Molecular Beam Epitaxy and Characterization of Bi-Based V_2VI_3 Topological Insulators

Dissertation zur Erlangung des
naturwissenschaftlichen Doktorgrades
der Bayerischen Julius-Maximilians-Universität
Würzburg

vorgelegt von
Steffen Schreyeck
aus Memmingen

Würzburg 2016

Eingereicht am: 19.12.2016

bei der Fakultät für Physik und Astronomie

1. Gutachter: Prof. Dr. Karl Brunner
2. Gutachter: Prof. Dr. Grzegorz Karczewski
3. Gutachter:

der Dissertation.

1. Prüfer: Prof. Dr. Karl Brunner
2. Prüfer: Prof. Dr. Grzegorz Karczewski
3. Prüfer: Prof. Dr. Björn Trauzettel

im Promotionskolloquium.

Tag des Promotionskolloquiums: 10.03.2017

Doktorurkunde ausgehändigt am:

Contents

Summary 1

Zusammenfassung 5

1 Introduction 9

2 Bi-based topological insulators of the V_2VI_3 material-system 13

3 Methods 19

3.1 Molecular beam epitaxy (MBE) . . . 19

3.2 Refraction high energy electron diffraction (RHEED) . . . 26

3.3 X-ray analysis techniques . . . 31

3.3.1 X-ray diffraction (XRD) . . . 31

3.3.2 X-ray reflection (XRR) . . . 36

3.4 Atomic force microscopy (AFM) . . . 38

3.5 Energy dispersive x-ray spectroscopy (EDX) . . . 40

3.6 Lithography and magnetotransport . . . 41

4 Molecular beam epitaxial growth and characterization of Bi_2Se_3 43

4.1 Bi_2Se_3 films on Si(111) . . . 43

4.2 Bi_2Se_3 grown on lattice matched InP(111) . . . 48

4.3 Twin suppression in Bi_2Se_3 films on InP . . . 60

4.3.1 Bi_2Se_3 on 2° miscut InP(111) substrate . . . 60

4.3.2 Bi_2Se_3 on rough InP(111) substrate . . . 62

5 Growth and characterization of $Bi_{2-x}Sb_xTe_{3-y}Se_y$ (BSTS) films 75

5.1 Bi_2Te_3 . . . 75

5.2 $Bi_2Te_{3-y}Se_y$ . . . 79

5.3 $Bi_{2-x}Sb_xSe_3$ . . . 86

5.4 $Bi_{2-x}Sb_xTe_{3-y}Se_y$ . . . 98

6 Magnetic doping of topological insulators **103**

Bibliography **111**

Publications **119**

Danksagung **121**

Summary

The present thesis is addressed to the growth and characterization of Bi-based V_2VI_3 topological insulators (TIs). The TIs were grown by molecular beam epitaxy (MBE) on differently passivated Si(111) substrates, as well as InP(111) substrates. This allows the study of the influence of the substrate on the structural and electrical properties of the TIs.

The Bi_2Se_3 layers show a change of mosaicity-tilt and -twist for growth on the differently prepared Si(111) substrates, as well as a significant increase of crystalline quality for growth on the lateral nearly lattice matched InP(111). The rocking curve FWHMs observed for thick layers grown on InP are comparable to these of common zincblende layers, which are close to the resolution limit of standard high resolution X-ray diffraction (HRXRD) setups. The unexpected high structural crystalline quality achieved in this material system is remarkable due to the presence of weak van der Waals bonds between every block of five atomic layers, i.e. a quintuple layer (QL), in growth direction.
In addition to the mosaicity also twin domains, present in films of the V_2VI_3 material system, are studied. The twin defects are observed in Bi_2Se_3 layers grown on Si(111) and lattice matched InP(111) suggesting that the two dimensional surface lattice of the substrates can not determine the stacking order ABCABC... or ACBACB... in locally separated growth seeds. Therefore the growth on misoriented and rough InP(111) is analyzed.
The rough InP(111) with its facets within a hollow exceeding the height of a QL is able to provide its stacking information to the five atomic layers within a QL. By varying the roughness of the InP substrate surface, due to thermal annealing,

the influence on the twinning within the layer is confirmed resulting in a complete suppression of twin domains on rough InP(111).
Focusing on the electrical properties of the Bi_2Se_3 films, the increased structural quality for films grown on lattice matched flat InP(111)B results in a marginal reduction of carrier density by about 10% (n=9×10^{18}cm^{-3}) compared to the layers grown on H-passivated Si(111) (n=1×10^{19}cm^{-3}), whereas the suppression of twin domains for growth on rough InP(111)B resulted in a reduction of carrier density by an order of magnitude (n=9×10^{17}cm^{-3}). This implies, that the twin domains are a main crystal defect responsible for the high carrier density in the presented Bi_2Se_3 thin films.

Besides the binary Bi_2Se_3 also alloys with Sb and Te are fabricated to examine the influence of the compound specific point defects on the carrier density. Therefore growth series of the ternary materials $Bi_2Te_{3-y}Se_y$, $Bi_{2-x}Sb_xSe_3$, and $Bi_{2-x}Sb_xTe_3$, as well as the quaternary $Bi_{2-x}Sb_xTe_{3-y}Se_y$ are studied.
The alloy $Bi_2Te_{3-y}Se_y$ is investigated concerning the chemical order of Te and Se on the group-VI lattice sites within the QL to reduce Se vacancy defects. Particularly, the composition $Bi_2Te_2Se_1$ with perfect order of 100% is a promising candidate to suppress Se vacancies, where the middle layer of the QL is occupied by the more electronegative Se atoms and the outer layers of the QL by Te. For the MBE grown $Bi_2Te_2Se_1$ layers the achieved chemical order is 75% Se atoms in the middle layer of the QL, as determined by XRD peak intensities compared to structure factor calculations.
Magnetotransport measurements on the partially ordered alloys $Bi_2Te_2Se_1$ grown on Si(111) reveal that the carrier concentration is still as high as n=1×10^{19}cm^{-3}, whereas the layers still exhibit twin domains, which might screen the effect of the suppression of Se vacancies. In the context of twin suppression in $Bi_2Te_2Se_1$ layers it is worth to mention, that studies on suppressing twin domains within quaternary $Bi_{2-x}Sb_xTe_{3-y}Se_y$ layers grown on rough InP(111) were successful.
To further reduce the carrier density of twin free Bi_2Se_3 layers grown on InP(111)B:Fe a series of $Bi_{2-x}Sb_xSe_3$ alloys were grown under comparable growth conditions. This

results in a reduction of the carrier density with a minimum (n=3×10^{17}cm^{-3}) in the composition range of about $x = 0.9 - 1.0$. This minimum is close to the transition of the R$\bar{3}$m symmetry of the TIs to the Pnma symmetry of Sb_2Se_3, which is determined to occur between $x = 1.2 - 1.4$ by XRD. Thus realizing a transition from n-type to p-type conduction is hindered.
The $Bi_{2-x}Sb_xTe_3$ alloys exhibit a pn-transition, due to the dominating n-type and p-type point defects in its binary compounds, which is determined to reduce the bulk carrier density enabling the study the TI surface states. This pn-transition plays a significant role in realizing predicted applications and exotic effects, such as the quantum anomalous Hall effect.

The magnetic doping of topological insulators with transition metals is studied by incorporating Cr and V in the alloy $Bi_{2-x}Sb_xTe_3$ by codeposition. The preferential incorporation of Cr on group-V sites is confirmed by EDX and XRD, whereas the incorporation of Cr reduces the crystalline quality of the layer. Magnetotransport measurements of the Cr-doped TIs display an anomalous Hall effect confirming the realization of a magnetic TI thin film. The quantum anomalous Hall effect is observed in V-doped $Bi_{2-x}Sb_xTe_3$, where the V-doping results in higher Curie temperatures, as well as higher coercive fields compared to the Cr-doping of the TIs.

Moreover the present thesis contributes to the understanding of the role of the substrate concerning the crystalline quality of van der Waals bonded layers, such as the V_2VI_3 TIs, MoS_2 and $WoTe_2$. Furthermore, the fabrication of the thin film TIs $Bi_{2-x}Sb_xTe_{3-y}Se_y$ in high crystalline quality serves as basis to explore the physics of topological insulators.

Zusammenfassung

In der hier vorliegenden Arbeit wurden die auf Bi-Verbindungen basierenden topologischen Isolatoren (TI) des V_2VI_3-Materialsystems hergestellt und sowohl deren strukturelle als auch elektrische Eigenschaften untersucht. Die Herstellung der TIs mittels Molekularstrahlepitaxie (MBE) erfolgte auf verschieden präparierten Si(111)-Oberflächen und auf InP(111) Substraten. Dadurch konnte der Einfluss der Substrate auf die strukturelle Qualität der Bi_2Se_3 Schichten, die lateral nahezu perfekt gitterangepasst zu InP(111) sind, analysiert werden. Während bereits die verschieden präparierten Si(111) Oberflächen einen Einfluss auf die Mosaizität aufweisen, erreichen die auf InP(111) gewachsenen Schichten die strukturelle Qualität gängiger Zinkblende Halbleiterschichten die mittels MBE hergestellt werden und damit auch die Auflösungsgrenze eines hoch auflösenden Röntgendiffraktometers (HRXRD). Dies ist besonders bemerkenswert, da diese TIs aus Blöcken von fünf kovalent gebundenen atomaren Schichten (QL) bestehen, die untereinander durch vergleichbar schwache Van-der-Waals Bindungen verbunden sind.

Neben der Mosaizität wurden auch Zwillingsdefekte untersucht, die für Schichten des V_2VI_3 Materialsystems typisch sind. Hier konnte festgestellt werden, dass eine glatte zweidimensionale (2D) Substratoberfläche nicht einheitlich vorgeben kann, ob die Stapelfolge in räumlich getrennten Kristallisationszentren ABCABC... oder ACBACB... ist.
Um die Zwillingsdefekte zu unterdrücken wurde das Wachstum auf rauen InP(111) Substraten untersucht. Die raue Oberfläche ermöglicht es an Facetten der Substratoberfläche neben der lateralen Orientierung der Schicht auch die Stapelfolge der Schicht zu definieren. Der Einfluss der Beschaffenheit der Substratoberfläche kon-

nte durch Variation der Rauigkeit, mittels thermischen Ausheizens, belegt werden. Das Wachstum auf rauen InP Substraten führt zu einer kompletten Unterdrückung der Zwillingsdefekte.
Betrachtet man nun den Einfluss der Steigerung der Kristallqualität auf die elektrischen Eigenschaften, so stellt man fest, dass die Unterdrückung der Zwillingsdefekte die Ladungsträgerdichte im Vergleich zu dem auf Si gewachsenem Bi_2Se_3 um eine Größenordnung reduziert (n=9×10^{17}cm^{-3}), während die Verwendung von gitterangepassten Substraten mit glatter Oberfläche sie lediglich um 10% reduziert (n=9×10^{18}cm^{-3}). Dies belegt, dass in den hier vorgestellten Schichten die Zwillingsdomänengrenzen die Hauptursache der unerwünscht hohen Ladungsträgerdichten sind.

Zusätzlich zu der Verbesserung der kristallinen Qualität von Bi_2Se_3 wurden Legierungen mit Sb und Te hergestellt, um die Ladungsträgerdichte durch Reduzieren von Punktdefektdichten zu senken. Hierfür wurden sowohl die ternären $Bi_2Te_{3-y}Se_y$, $Bi_{2-x}Sb_xSe_3$ und $Bi_{2-x}Sb_xTe_3$, als auch die quaternären $Bi_{2-x}Sb_xTe_{3-y}Se_y$ Legierungen in Wachstumsserien hergestellt und untersucht.
Das Einbauverhalten des elektronegativeren Se im Vergleich zu Te auf den unterschiedlichen Gruppe-VI Mittel- und Außenlagen im QL wurde im Hinblick auf eine Reduzierung von Se Fehlstellen anhand von $Bi_2Te_{3-y}Se_y$ Legierungen studiert. Besonders die Zusammensetzung $Bi_2Te_2Se_1$ mit perfekter Ordnung, welche durch 100% Se auf der Mittellage und Te auf der Außenlagen beschrieben wird, ist vielversprechend um die Se Fehlstellen zu reduzieren. Die erreichte chemische Ordnung in MBE gewachsenen $Bi_2Te_2Se_1$ Schichten beträgt 75% Se auf der Mittellage, die durch den Vergleich von XRD-Peak-Intensitäten und Strukturfaktor-Berechnungen bestimmt wurde.
Magnetotransport Messungen an $Bi_2Te_2Se_1$ Schichten auf Si(111) zeigen jedoch relativ hohe Ladungsträgerdichten von n=1×10^{19}cm^{-3}, welche vermutlich durch die Präsenz von Zwillingsdomänen in den Schichten dominiert wird und daher den Effekt der Reduzierung von Se Fehlstellen überdeckt. In Hinblick auf die Unterdrückung von Zwillingsdefekten in $Bi_2Te_2Se_1$ ist es erwähnenswert, dass quaternäre

$Bi_{2-x}Sb_xTe_{3-y}Se_y$ (BSTS) Schichten auf rauem InP(111) bereits zwillingsdomänenfrei hergestellt wurden.

Die Legierung $Bi_{2-x}Sb_xSe_3$ wurde wie Bi_2Se_3 auf rauem InP(111) gewachsen, um die Zwillingseffekte zu unterdrücken. Durch das Legieren mit Sb konnte eine weitere Reduktion der Elektronen Ladungsträgerdichte, die ihr Minimum im Bereich von $x = 0.9 - 1.0$ erreicht, realisiert werden (n=3×10^{17}cm^{-3}). Die Ladungsträgerdichte steigt bei größerem Sb-Gehalt wieder an, bevor ein kompletter Wechsel zur Löcherleitung beobachtet werden konnte. Der Übergang zu p-dotierten Schichten wird durch den mit XRD Messungen beobachtetem Wechsel der R$\overline{3}$m Symmetrie von Bi_2Se_3 zur Pnma Symmetrie von Sb_2Se_3 zwischen $x = 1.2 - 1.4$ verhindert, welcher zusätzliche Defekte verursacht.
Die $Bi_{2-x}Sb_xTe_3$ Legierungen sind durch den beobachteten pn-Übergang, der durch die in den binären TIs jeweils dominierenden Donator und Akzeptor Punktdefekte erzeugt wird, von großem Interesse, da sich diese Schichten dazu eignen die Volumenleitfähigkeit im Magnetotransport zu unterdrücken. Dies ist von besonderer Bedeutung für die Realisierung der vorhergesagten Anwendungen und exotischen Effekte in TIs.

Weiterhin wurde die magnetische Dotierung von $Bi_{2-x}Sb_xTe_3$-Schichten mit den Übergangsmetallen Chrom und Vanadium im Hinblick auf die Realisierung des Quanten anormalen Hall-Effekts (QAHE) untersucht. Der überwiegende Einbau der Cr-Atome auf Gruppe-V-Plätzen konnte mittels EDX und XRD Messungen bestätigt werden. Die TI-Schichten zeigen im Magnetrotransport einen anormalen Hall-Effekt, welcher die Magnetisierung der Schicht durch die Cr-Dotierung bestätigt. Die Realisierung des QAHE konnte in V-dotierten $Bi_{2-x}Sb_xTe_3$ Schichten erzielt werden, welche als weitere Vorteile die höheren Curie-Temperaturen und größere Koerzitivfeldstärken im Vergleich zu Cr-dotierten Schichten mit sich bringen.

Die in dieser Arbeit untersuchte Herstellung von den Bi-basierten TI-Schichten des V_2VI_3-Materialsystems mittels MBE schafft neue Erkenntnisse in Hinblick auf den Einfluss von Substraten auf Van-der-Waals gebundene Schichten, wie zum

Beispiel BSTS als auch MoS_2 und $WoTe_2$. Die Herstellung von $Bi_{2-x}Sb_xTe_{3-y}Se_y$ TI Schichten in verschiedenen Zusammensetzungen x und y mit hoher struktureller Qualität dient zudem als Grundlage für die weitere Erforschung der TI-basierten Effekte und Anwendungen.

1 Introduction

The present thesis addresses the MBE growth and the characterization of Bi-based V_2VI_3 topological insulators including magnetic doping with transition metals.
Topological insulators are a new emerging field in condensed matter physics. The field was opened in 2005 by Kane and Melee predicting a 2D topologically protected time reversal invariant state with a bulk electronic band gap and gap less spin polarized edge states, the so-called Quantum spin Hall state [KM05]. Topological insulators are proposed to host several novel applications, e.g. in spintronics and quantum computing, as well as exotic physical phenomena, including the quantum anomalous Hall effect (QAHE)[YZZ+10], majorana fermions [FK08], and axionic insulators [LWQZ10].
The search for experimental realization of topological insulators focuses on compounds consisting of heavy elements with strong spin orbit coupling causing band inversion, as predicted by Bernevig et al. for HgTe quantum wells embedded in CdTe [BHZ06]. In 2007, the first 2D topological insulator was experimentally observed in HgTe/(Hg,Cd)Te quantum wells by the Molenkamp group [KWB+07]. Subsequently, 3D topological insulators with topologically protected surface states were predicted in 2007 [FKM07] and experimentally confirmed by ARPES measurements of bulk $Bi_{1-x}Sb_x$ in 2008 [HQW+08]. The second generation of 3D TIs are Bi_2Se_3, Bi_2Te_3 and Sb_2Te_3, which were predicted to feature 3D topological surface states by Zhang et al. [ZLQ+09] and experimentally discovered by ARPES measurements of Bi_2Se_3 [XQH+09], and Bi_2Te_3 bulk crystals in 2009 [Che09]. Beside the bulk valance- and conduction-band, these ARPES measurements display two bands with linear dispersion forming a single Dirac cone within the bulk band gap of up to 0.3 eV (Bi_2Se_3) [XQH+09, ZQT+09]. The relatively large bulk band gap

and the ideal single Dirac cone with nearly linear dispersion at the center of the Brillouin zone of these TIs enable to study the surface states and applications even at room temperature [ZLQ+09].

While the existence of the surface states of the Bi-based V_2VI_3 chalcogenides is well established, it is challenging to fabricate them with insulating bulk in order to realize the proposed exotic effects and applications. Until now the majority of the crystals were grown by Bridgeman-like methods to obtain ingots for thermoelectric studies. Most of the TIs have a high bulk carrier density, as observed by the ARPES measurements displaying a large portion of the conductance band occupied by electrons for Bi_2Se_3 and Bi_2Te_3 [XQH+09, Che09, HXQ+09]. As these bulk carriers conceal the surface-state contribution in magneto transport, the exploration of their electrical properties is prevented. Therefore, the carrier density in these TIs has to be decreased. The main crystalline imperfections influencing the carrier density are Se vacancies, $Te_{Bi/Sb}$ and Bi/Sb_{Te} antisite defects, rotational twin domain boundaries, translation domain boundaries, as well as the crystallization of other crystalline phases such as V_4VI_3 or V_1VI_1 [TT61, Nak63, HCK86, FGT+88, LWK+10, LLH05].

One approach to reduce the carrier density is the suppression of crystal defects in the TIs by the application of molecular beam epitaxy (MBE). MBE allows to precisely control the growth parameters to systematically optimize the structural and electrical properties of the thin TI films. First studies on the MBE of these TIs investigated the growth of Bi_2Se_3 by codeposition of elemental Bi and Se on Si(111) substrate [ZQT+09]. The Si(111) substrate was chosen in order to fit to the lateral hexagonal crystal lattice structure of Bi_2Se_3 with a mismatch of the hexagonal lattice constants of 7.8%, which is relatively large compared to common semiconductor heterostructures [ZQT+09].

In the following chapters of this work three novel aspects of the MBE growth of the Bi-based TIs are presented.

First, the increase of the structural quality including the twin suppression in Bi_2Se_3 layers is studied by the use of Si(111) and lattice matched InP(111) substrates. Therefore differently passivated surfaces are investigated for the growth on Si(111), i.e. Bi-, Se-, and H- passivation. The growth on InP(111) substrates is studied for its lateral lattice match to the hexagonal surface lattice of Bi_2Se_3 to increase the structural quality, concerning mosaicity-size, -tilt and -twist. In addition the growth on miscut- and rough- InP substrates is investigated to reduce the twin domains present in the thin films.
Second, the alloying of Bi_2Se_3 with Sb and Te is examined to control the defect chemistry in this material system. The substitution of Se by Te, i.e. $Bi_2Te_{3-y}Se_y$, is applied for y ranging from 0 to 3 to reduce point defects, such as Se vacancies. Complementary, the alloying with Sb, i.e. $Bi_{2-x}Sb_{2-x}Te_{3-y}Se_y$, prospects a p-n transition for the Te rich V_2VI_3 material system by controlling the V_{VI} and VI_V antisite defects. In addition, the Sb alloying of Bi_2Se_3 is analyzed, i.e. $Bi_{2-x}Sb_{2-x}Se_3$, which is also a candidate to host a p-n transition prior the change of crystal structure to the Pnma symmetry of the trivial insulator Sb_2Se_3 [ZLQ$^+$09, EZK$^+$13].
Third, based on the growth of high structural quality MBE grown layers the magnetic doping of the TIs is elucidated. Here, the doping of the alloy $Bi_{2-x}Sb_{2-x}Te_3$ with transition metals, such as Cr and V, is investigated to reveal the interplay between surface states and magnetization to pave the way for the experimental realization of the QAHE.

2 Bi-based topological insulators of the V_2VI_3 material-system

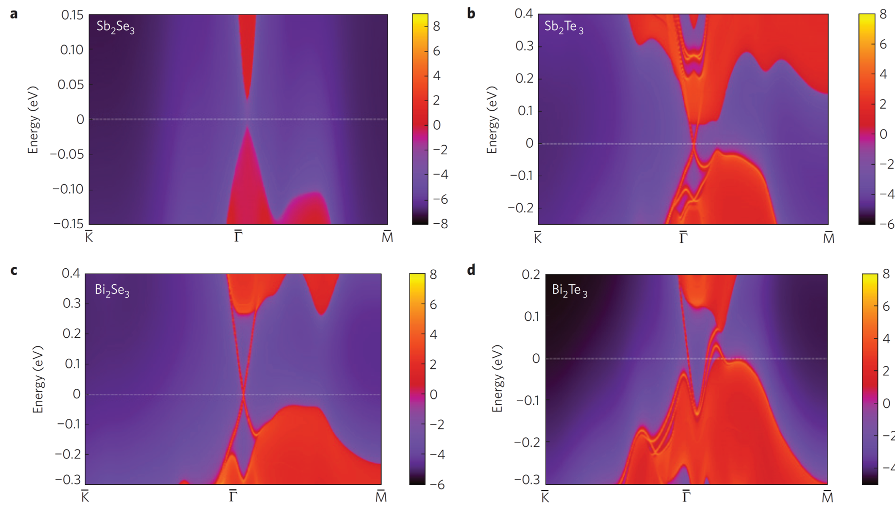

Fig. 2.1: Calculated energy momentum maps displaying the local density of states forming the bulk bands (red regions) of the trivial insulator (a) Sb_2Se_3, as well as the topological insulators (b) Sb_2Te_3 (c) Bi_2Se_3 and (d) Bi_2Te_3 with their surface states clearly visible within the bulk band gap at the Γ-point, taken from [ZQT+09]. *Reprinted by permission from Macmillan Publishers Ltd: Nature Physics, 5(6):438-442, copyright (2009)*

The V_2VI_3 compounds Bi_2Se_3, Bi_2Te_3, and Sb_2Te_3 were predicted to host topologically protected surface states with relatively large bulk band gaps compared to other TIs, as shown in figure 2.1 [ZQT+09]. The surface states arise from the p_z orbitals of the cation and the anion, which are reversed due to the strong spin orbit coupling (SOC) causing a band inversion, as displayed in figure 2.2, whereas Sb_2Se_3 with its weaker SOC is a trivial insulator [ZQT+09]. The surface states in these TIs form a single Dirac cone at the middle of the Brillouin zone (Γ-point) [ZQT+09]. Bi_2Se_3 exhibits the largest band gap of them with the crossing point of the surface

states (Dirac point) within the band gap making it to the most promising and studied of these TIs [ZQT+09].

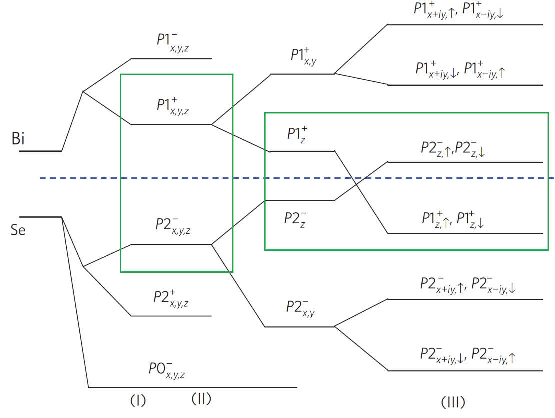

Fig. 2.2: Schematic diagram of the evolution of the p-orbitals of Se and Bi close to the Fermi level (blue dashed line) of Bi_2Se_3, with the stages (I), (II), and (III) representing the effect of turning on the chemical bonding, crystal field splitting, and spin orbit coupling, respectively, taken from [ZQT+09]. *(Reprinted by permission from Macmillan Publishers Ltd: Nature Physics (www.nature.com/nphys/), 5(6):438-442, copyright (2009))*

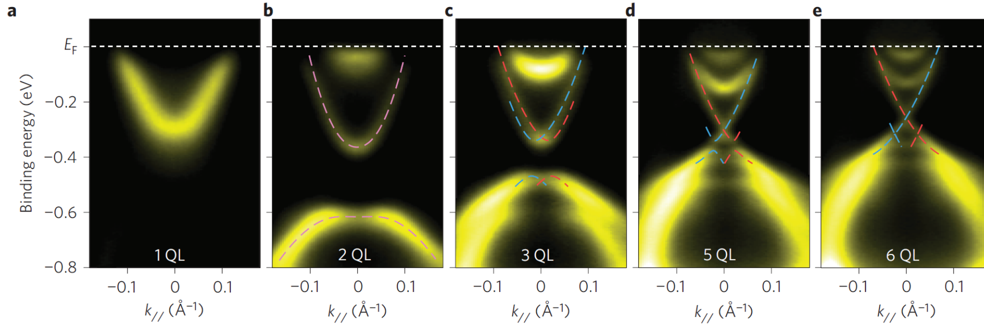

Fig. 2.3: ARPES spectra of Bi_2Se_3 for (a)-(e) 1, 2, 3, 5, and 6 QL thick films, displaying the bulk bands and the topological surface states (marked by blue and red dashed lines), taken from [ZHC+10]. *(Reprinted by permission from Macmillan Publishers Ltd: Nature Physics (www.nature.com/nphys/), 6(8):584-588, copyright (2010))*

The topological surface states are localized at the surface region with a penetration depth in Bi_2Se_3 of about 2 to 3 quintuple layer [ZYZ+10]. ARPES measurements of Bi_2Se_3 films with a thickness below 6 nm show an energy gap opening due to the coupling of the top and bottom surface states marking the 2D limit of this 3D topological insulator, as shown in figure 2.3 [ZHC+10, LSE+14].

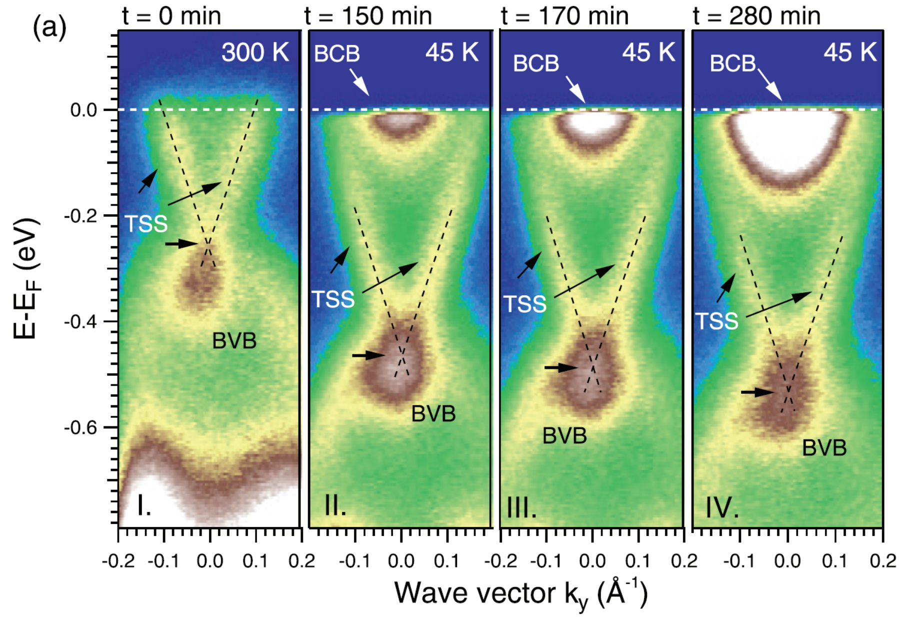

Fig. 2.4: ARPES spectra of $Bi_2Te_2Se_1$ displaying the shift of the Fermi level over time after removal of the Se capping layer. The shift of the bulk conduction band (BCB), bulk valance band (BVB), and the topological surface states (TSS) to lower energies is clearly visible [MSS+14].

ARPES is a powerful technique to analyze the topological surface states due to its surface sensitivity, whereas it is also limited to the surface analysis and it is sensitive to surface contamination by the residual gas within the UHV. This leads to differences of the determination of the bulk band gap value to other techniques, such as magneto optics, where the band gap is determined to be significantly smaller, i.e. 0.2 eV, compared to the 0.3 eV determined by ARPES [OPM+15]. The time dependent shift of the Fermi level to higher energies caused by adsorbates of the residual gas, also called aging effect, is displayed in figure 2.4.

Bi_2Se_3, Bi_2Te_3, and Sb_2Te_3 crystallize in the trigonal space group R$\bar{3}$m ($D_3{}^5$). In literature the V_2VI_3 compounds are commonly described in a hexagonal basis with 15 atoms per unit cell, with $a = b \neq c$, $\alpha = \beta = 90°$, and $\gamma = 120°$. The crystals consist of blocks of five covalently bonded atomic layers VI(1)-V-VI(2)-V-VI(1) forming a quintuple layer (QL) stacked in [001]-direction, as shown exemplarily for Bi_2Se_3 in figure 2.5 (a) and (b). Each atomic layer has a 2D hexagonal lattice. These are stacked in a ABC stacking order resulting in a threefold symmetry. The

group-VI sites differ in their coordination number: six for the VI(2)-site and three for the VI(1)-site. This makes the VI(2) site in the middle of the QL favorable for the more electronegative elements in alloys, as studied in chapter 5.2, whereas the outer sites of the QL are more likely to form vacancy defects. The QLs are bonded by van der Waals force to each other, which is relatively weak compared to the bonds within a QL. As a consequence of the vdW bonds between QLs, the material can be cleaved along (001)-planes by using a exfoliation technique, similar to graphene.

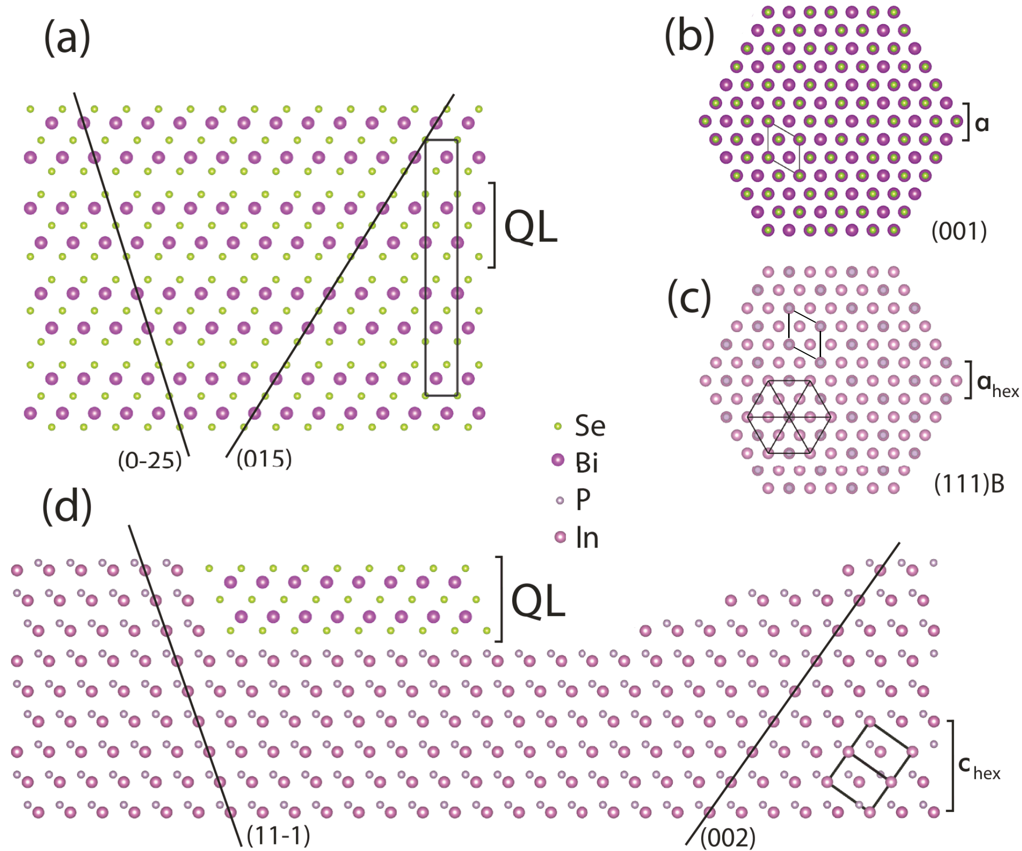

Fig. 2.5: Crystal structures of Bi_2Se_3 and InP with unit cells and lattice planes indicated in black. (a) side view in [100] direction and (b) top view of Bi_2Se_3. (c) top view of InP (P atoms filled homogeneously for better visibility) and (d) side view of InP in [1-10] direction with bi-layer steps and a three bi-layer high (11-1) facet. A QL of Bi_2Se_3 is aligned for comparison of the lattice structures with the (015) Bi_2Se_3 plane nearly parallel aligned to the (002) InP plane, as well as the (0-25) Bi_2Se_3 plane aligned to the (11-1) InP plane. The lattice constants a_{hex} and c_{hex} of InP are indicated for comparison of the two different crystal structures.

The binary V_2VI_3 compounds differ in their lattice parameters. Bi_2Se_3 has the smallest lattice constants of the binary compounds, followed by Sb_2Te_3 and Bi_2Te_3. While alloying Bi_2Se_3 with Te enlarges both the a and c lattice constant, the alloying with Sb mainly affects the a lattice constant. Figure 2.6 displays the relations of the a and $c/3$ (c/3 is equal to the height of a QL) lattice constants of the V_2VI_3 compounds. In addition, the hexagonal 2D surface lattice constants of common (111) oriented substrates, e.g. zincblende- and diamond-type substrates, are indicated versus the height of three bi-layer steps c_{hex} , which is comparable to the height of a QL, and the lateral hexagonal lattice constant a_{hex}, as shown exemplarily for Bi_2Se_3 and InP(111)B in figure 2.5 (c) and (d). This gives an overview of hexagonal 2D surface lattices of common substrates matching to the V_2VI_3 compounds. Due to their different crystal symmetry a match of the hexagonal surface lattices does not imply a match of the out of plane lattice constants of substrate and layer. Figure 2.5 displays the differences for Bi_2Se_3 and InP, as an example for an interface of a TI to a substrate studied in this thesis, whereas the (015) Bi_2Se_3 plane is nearly parallel aligned to the (002) InP plane and the (0-25) Bi_2Se_3 plane is nearly parallel aligned to the (11-1) InP plane. The interface between substrate and layer is due to the mismatch of crystal structure an additional source of defects, which is studied in detail in chapter 4.2 and 4.3.

The point defects in this material-system have been studied in earlier works, which mainly focused on crystals grown by melt for thermoelectric applications. Depending on the composition of the V_2VI_3 materials specific defects where found. In Bi_2Se_3 Se vacancies are the dominant defects resulting in n-type material [Nak63]. This defect is favored by the high vapor pressure of the Se compared to Te.
Bi_2Te_3 is observed to occur as n-type (Te-rich), as well as p-type (Bi-rich) material, depending on the ratio of Bi and Te in the melt, causing Te_{Bi} or Bi_{Te} antisite defects [FGT+88].
The Sb_2Te_3 appears as heavily p-type doped material due to the dominating Sb_{Te} antisite defects acting as acceptors [TT61].

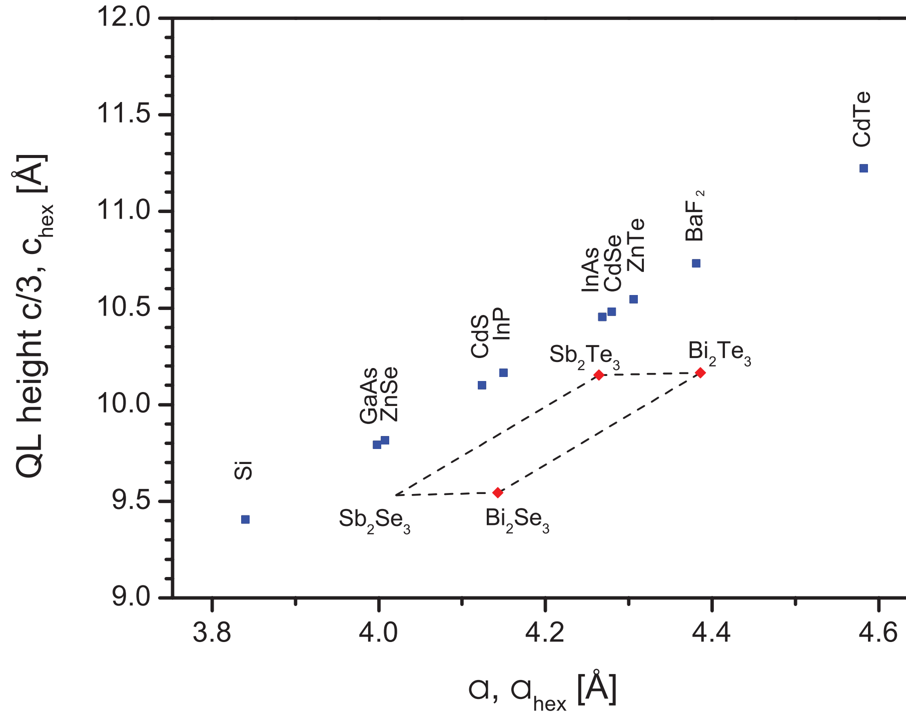

Fig. 2.6: Comparison of the lattice parameters of the V_2VI_3 TIs (red squares) and common cubic (111) oriented substrates (blue squares) [Wyc64]. The indicated QL height of the TIs is equal to $c/3$. The dashed lines connecting the lattice constants of the TIs indicate the change of lattice constants for alloys after Vegard's law, including an extrapolation for hypothetical Sb_2Se_3 in $R\bar{3}m$ symmetry. The lattice constants of (111) oriented cubic substrates are plotted as the hexagonal 2D surface lattice with a_{hex} ($a_{hex} = a_{cubic}/\sqrt{2}$) and the diagonal of the unit cell c_{hex} ($c_{hex} = a_{cubic} \cdot \sqrt{3}$), which corresponds to the height of three bi-layers for zincblende substrates [ML33, Nak63, Wyc63, Wyc64, Pal98, GM03].

3 Methods

3.1 Molecular beam epitaxy (MBE)

Molecular beam epitaxy (MBE) is a technique for growth of crystalline thin films in ultra high vacuum (UHV) conditions, which was developed since the 1960s and is well described in literature, which serves as basis of this section [Par85, HS96, Bra99]. The advantage of this technique, compared to other crystal growth methods, is the precise control of beam fluxes, which enables growth of atomic layer-by-layer and the setting of surface dynamics by the independent choice of the substrate and source temperatures [Par85]. In-situ shutters allow to interrupt the molecular beams realizing the growth of sharp interfaces between different crystalline materials. This enables the fabrication of heterostructures, such as superlattices and quantum well films. Further UHV MBE growth-, analysis-, and preparation chambers can be connected to a MBE system. These enable additional in-situ measurements and sample fabrication options prior and after the epitaxy. Typically, a load-lock chamber is attached to the MBE chamber, which enables loading substrates into the MBE system without interrupting the UHV in the growth chamber.

To achieve an UHV in a MBE system, it is necessary to generate a pre-vacuum by oil free pumps, such as scroll pumps (typically below 10^{-1}mbar). Turbo molecular pumps are used to pump to UHV range, which is optionally further improved by complementary pumps, such as ion getter -, titanium sublimation - or cryopumps. These facilitate to realize a base pressure below 10^{-10} mbar in a MBE chamber. The vacuum condition in a MBE chamber has two major implications on the growth. First, the recoverage rate of the surface by residual gas is direct proportional to the background pressure. Thus, the contamination of the grown film with residual

gas atoms is reduced by improving the vacuum conditions. Second, the mean free path L of molecules is indirectly proportional to the pressure p_{MBE} in the vacuum system, described by the formula:

$$L = \frac{k_B T_{MBE}}{\sqrt{2}\pi p_{MBE} d_m^2}, \tag{3.1}$$

where T_{MBE} is the temperature of the chamber, k_B the Boltzmann constant, and d_m the diameter of the molecules [HS96]. This results in mean free paths of molecules orders of magnitudes lager than the dimensions of the growth chamber for pressures in the UHV range. Accordingly, the interaction of molecular beams with residual gas is negligible small prior to impinging on the substrate surface [HS96].

The molecular beams are typically thermally produced with effusion cells operated at element or compound specific temperature ranges, which are partially collected in vapor pressure data tables [HK69]. The most source materials are available in purities of 99.9999% (6N) or higher to guarantee the growth of ultra pure layers. The flux of the molecular beams is indirectly measured as a beam equivalent pressure (BEP),i.e. p_X/η_X, by an ion gauge (after Bayard-Alpert) close to growth position, where p_X is the measured pressure and η_X the ionization sensitivity of the material X [FO71]. The BEP is linked to the flux by the ideal gas law, which describes the relation between pressure p, and the density within a Volume N/V at a given temperature (temperature of the ion gauge T_{IG}, i.e. 300K) $p = N/V \cdot k_B \cdot T_{IG}$, where in this case p corresponds to the measured BEP. The flux F_X is proportional to $N/V \cdot v_X$, where N/V is the density of particles within a Volume and v_X the average thermal velocity ($v_X \propto \sqrt{T_X/M_X}$ with the temperature T_X, molar weight M_X). This results in the relation between BEP and flux $F_X \propto BEP\sqrt{T_X/M_X}$. To deduce the flux ratio of two materials (X and Y) from the BEPs, the average thermal velocities and the ionization efficiency η of the molecules have be taken into account, which is described by following equation:

$$\frac{F_X}{F_Y} = \frac{p_X}{p_Y}\frac{\eta_Y}{\eta_X}\sqrt{\frac{T_X M_Y}{T_Y M_X}}, \tag{3.2}$$

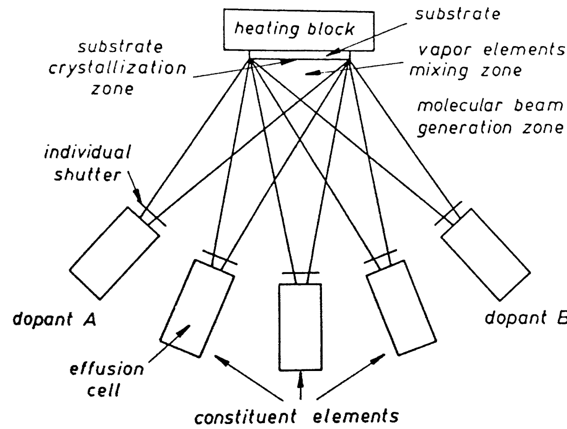

Fig. 3.1: Schematic of the growth in a MBE system, taken from [HS96]. *(Reprinted from Vacuum, 32, 9, M. A. Herman, Physical problems concerning effusion processes of semiconductors in molecular beam epitaxy, Copyright (1982), with permission from Elsevier; and republished with permission of Springer Science and Bus Media B V, from Molecular beam epitaxy: fundamentals and current status, M.A. Herman, H. Sitter, 7, 2nd ed, 1996; permission conveyed through Copyright Clearance Center, Inc.))*

with

$$\eta = [0.4Z/14 + 0.6] \tag{3.3}$$

where Z the number of electrons of the molecules [Par85, WDSW82, FO71]. The temperatures $T_{X,Y}$ of the molecules is measured by a thermocouple within the effusion cell, and the molar weight depends on the size of the molecules in the beam. To obtain the flux ratio between Bi and Sb, used for $Bi_{2-x}Sb_xSe_3$ growth described in chapter 5.3, an average molecule size of two atoms per molecule is assumed and the ion gauge ionization sensitivities are calculated by equation 3.3 multiplied by a factor of two to account for the number of atoms in the molecules, i.e. $\eta_{Bi} = 2 \cdot 3.0$ and $\eta_{Sb} = 2 \cdot 2.1$.

Figure 3.1 shows a schematic of molecular beams within a typical MBE chamber, which are directed to the middle of the substrate surface. Besides the interaction of the molecules of the beam with residual gas, mentioned above, also the interaction of molecules of the applied beams in the mixing zone (see Fig. 3.1) is negligible, due to the large mean free path of the molecules relative to the size of this zone [HS96]. Hence, the substrate surface is the active growth zone in a MBE growth process, where the applied materials crystallize.

To obtain a homogeneous distribution of the molecular beams on the substrate surface the manipulator in the growth chamber allows an in-plane rotation of the substrate-holder. The growth temperature is regulated by a heating filament behind the substrate and can be measured by a thermocouple, which is positioned at approximately the same distance to the filament as the substrate. The substrate-holder is required to be heated to temperatures up to 900°C in our experiments, without producing excessive background pressure, which is realized by the use of materials with low vapor pressure, such as molybdenum, tungsten, or tantalum. A pyrolytic boron nitride (PBN) ceramic plate is used in between filament and substrate to distribute the thermal radiation homogeneously to substrates with a diameter of two inches in the used MBE-system.

The precise control of the beam fluxes and substrate temperature enables to grow epitaxial films under reproducible conditions with specific growth dynamics at the substrate surface. Figure 3.2 shows a schematic of several surface processes, such as desorption, surface diffusion, nucleation, incooperation, interdiffusion, and overgrowth, which may occur during growth. To get information about the surface processes the growth is monitored by RHEED. This in-situ technique, described in section 3.5, allows an insight to the surface properties, such as determination of layer-by-layer growth, during MBE growth.

Once parameters to initialize crystalline MBE growth are determined, different growth modes may occur. The most prominent growth modes are displayed in figure 3.3. First, the Frank-van Merwe mode which describes a layer-by-layer growth. Second, the Stranski-Krastanov mode, which describes a mixed growth of layer plus islands caused by strain. Third, the Volmer-Weber mode, which describes pure island growth [HS96]. Fourth, a step flow mode where monolayers grow in-plane starting at surface steps on different height levels induced by the miscut of the used substrate (not shown). Other growth modes may also be realized within a MBE, such as polycrystalline growth at interfaces without lattice match or amorphous growth at low substrate temperature, e.g. to protect the layer of interest from oxidizing or contamination under ambient conditions.

Besides the growth conditions mentioned above, the choice of the substrate and

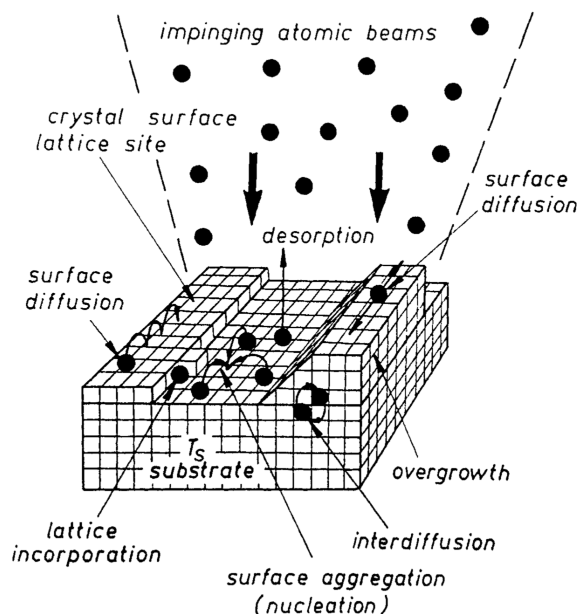

Fig. 3.2: Surface dynamics while growth, taken from [HS96]. *(Republished with permission of Springer Science and Bus Media B V, from Molecular beam epitaxy: fundamentals and current status, M.A. Herman, H. Sitter, 7, 2nd ed, 1996; permission conveyed through Copyright Clearance Center, Inc.)*

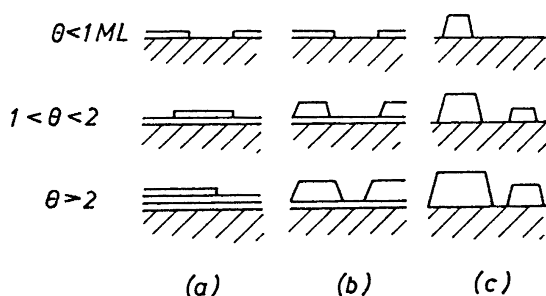

Fig. 3.3: Schematic of three common growth modes: (a) layer-by-layer Frank-van Merwe, (b) layer plus island (Stranski-Krastanov), and (c) island (Volmer-Weber) mode, taken from [HS96]. *(Republished with permission of Springer Science and Bus Media B V, from Molecular beam epitaxy: fundamentals and current status, M.A. Herman, H. Sitter, 7, 2nd ed, 1996; permission conveyed through Copyright Clearance Center, Inc. ; and Copyright IOP Publishing. Reproduced with permission from Rep. Prog. Phys., J. A. Venables, G. D. T. Spiller and M. Hanbucken, Nucleation and growth of thin films, 47,399-459, 1984 (https://doi.org/10.1088/0034-4885/47/4/002). All rights reserved.)*

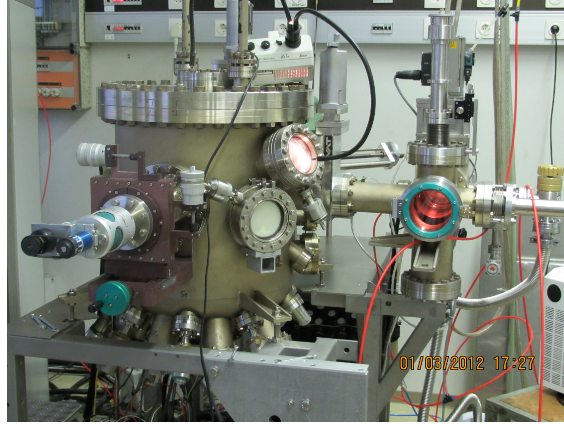

Fig. 3.4: Image of the CreaTec MBE chamber used for the Bi-based TI growth at the University Wuerzburg Phys. Inst. EP3. The photo was taken while a maintenance, therefore most connectors have been removed.

its preparation are crucial to obtain high crystalline quality for the MBE grown films (e.g. group IV, II-VI, and III-V semiconductors). Here, the substrate lattice is the guide for the impinging atoms/molecules and determines the positions of the atoms within the first atomic layers and, accordingly, the crystalline orientation of the film. Therefore substrates with a similar crystal symmetry and lattice-constant compared to the desired crystalline properties of the layer are chosen to reduce strain and defects at the interface of thin film heterostructures. In contrast to the MBE of covalent- or ionic-bonded semiconductors, little is known about the MBE of van der Waals (vdW) bonded 2D-layered materials, such as Bi_2Se_3, which are studied in this thesis. Efforts in the 90s by A. Koma et al. show that the growth of vdW bonded heterostructures, e.g. GaSe layers on MoS_2, results in a very uniform mono-layer film with its own bulk lattice constant (within the limit of 0.1%) and the a axis aligned to that of the substrate (within 0.1° or less, determined by STM Moiré pattern analysis), even though there exists substantially large lattice mismatch [KY86, Kom92]. These authors suggested, that the so called vdW epitaxy is possible between any layered materials regardless to their crystal structures and their lattice constants [KY86, Kom92]. A central objective of this thesis is analyzing the influence of substrate lattice with zincblende/diamond crystal structure on MBE grown 2D-layered materials to improve their crystalline quality.

The samples presented in this thesis are grown in a CreaTec MBE system with a

base pressure of 10^{-10} mbar, which is achieved by an ion-pump with an integrated titanium sublimation pump. The UHV system (see Fig. 3.4) is divided in a load lock chamber to store two substrate holders and a growth chamber equipped with eight standard effusion cells. The system has a built in ionization gauge (after Bayard-Alpert) to measure the beam equivalent pressure of the elements at the growth position. The Mo substrate holders are made for clamping two inch wafers on a PBN disk to guarantee a homogeneous heat distribution. The substrates can be heated to about 900° in the growth chamber. Cooling shrouds around the cells and in the top half of the chamber are kept at T_c=-20° to reduce cross contamination of the cells and reevaporation from the chamber walls. The elements Al, Bi, Ca, Cd, Cr, Pb, Sb, Sn, Se, Te, V, and Zn were evaporated within the MBE during this work. Several chamber openings to refill and exchange effusion cells were also used to clean and maintain the MBE chamber.

3.2 Refraction high energy electron diffraction (RHEED)

RHEED is a technique to probe the surface of a crystalline structure by reflection and diffraction of a high-energy electron beam in UHV. It is mainly used in MBE to monitor the growth process and is well described in literature [Bra99, HS96, IC04]. The electron beam is generated by a high voltage electron gun, which deflects the electron beam on the substrate surface under an angle typically below 3°. There, the electron beam is partially reflected and diffracted by the sample, i.e. the sample surface and few outermost atomic layers, resulting in a specular spot and a diffraction pattern on the fluorescence screen mounted at the opposite side of the electron-gun, as illustrated in Fig. 3.5 [HS96]. The diffraction pattern is recorded by a CCD camera connected to a computer to analyze the signal.

An advantage of this techniques is the possibility to measure in-situ, which allows to analyze the crystal surface, including the growth dynamics and the crystalline structure of the layer in real time. The various appearing RHEED patterns give insight to the structural quality of the crystalline layers close to the surface (few atomic layers). The main implications deduced from RHEED patterns are discussed below.

First, the pattern of the diffracted beam on the RHEED screen provide information of the crystallinity of the layer. Typical patterns, as displayed in Fig. 3.6 are streaks, spots, and rings, which arise from diffraction of 2D- (flat), 3D- (rough), and poly-crystalline structures, respectively. The streaks are oriented normal to the diffracting crystal plane. In addition to the streaks, Kikuchi lines appear in the diffraction pattern of crystals with sufficient structural quality, which are formed by diffusive multiple scattering of the electrons [Kai55]. RHEED patterns with diffusive (ring like) intensity distribution on the screen originate from amorphous materials, which are used to cap layers in this study. Also, a superposition of these typical RHEED patterns may appear in case of imperfect 2D-crystalline growth, enabling adjustment of the MBE parameters during growth.

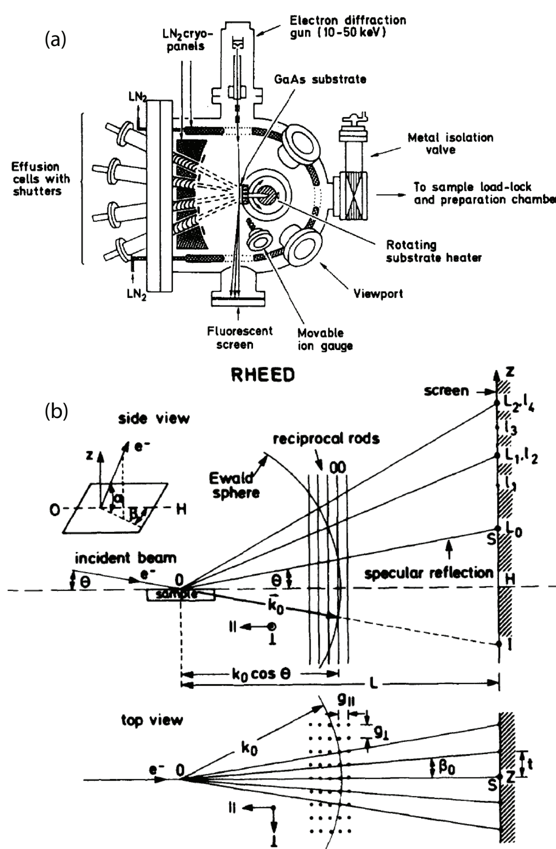

Fig. 3.5: (a) Typical arrangement of the RHEED gun, substrate, and fluorescent screen in a MBE chamber. Reprinted from Prog. Quant. Electr., 14, 289-356, E. O. Goebel and K. Ploog, Copyright (1990), with permission from Elsevier. (b) Diffraction geometry with Ewald sphere construction in the top and side view. The intersections of the Ewald sphere by the reciprocal lattice rods result in the RHEED features, which are projected to the screen [Bra99]. *(Reprinted figure with permission from I. Hernandez-Calderon and H. Hoechst, Physical Review B, 27, 4961, 1983. Copyright (1983) by the American Physical Society. (https://doi.org/10.1103/PhysRevB.27.4961))*

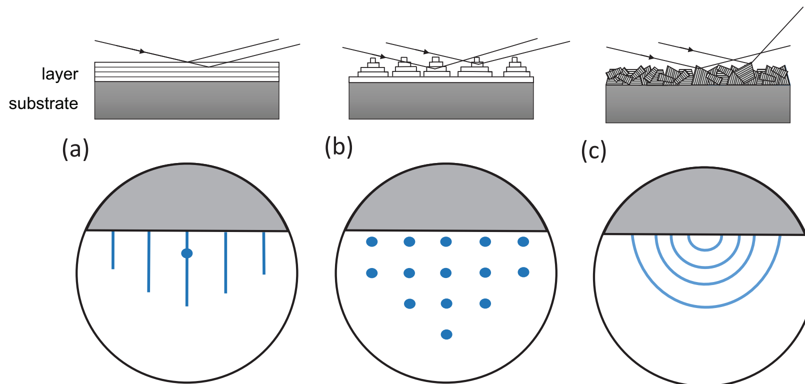

Fig. 3.6: Schematics of RHEED patterns observed for different layer surfaces (cross section): (a) atomically flat 2D surfaces result in a streaky pattern with a bright sharp specular spot, (b) 3D island growth results in a typical spotty pattern (c) a poly-crystalline surface results in a pattern with rings. Mixtures of these patterns are possible due to different locally diffracting and reflecting areas.

Second, the recording of the intensity of the specular spot of a streaky diffraction pattern during layer-by-layer growth allows to determine the growth speed of the layer. Figure 3.7 illustrates the influence of different growth stages on the intensities of the reflected beam. While the reflectivity of a closed atomic layer is at the maximum a partially covered atomic layer has a reduced reflectivity, resulting in an oscillation of the intensity of the specular spot during the growth [HS96]. A constant amplitude of the oscillation during the growth is associated with nucleation of monolayer islands and atomic layer-by-layer growth. While a damped intensity oscillation is a sign for growth of atomic layers starting to grow before the underlying layer (layers) is (are) closed. In the case of step-flow growth the reflectivity of the layer is constant and no oscillations are visible.

Third, the distance between streaks in a RHEED pattern is indirect proportional to the lateral lattice constant and the reoccurrence with substrate rotation depends on the crystal symmetry and orientation, e.g. the pattern of a (111) oriented zincblende or Si substrate exhibits a six-fold rotational symmetry due to the hexagonal 2D surface lattice (see figure 2.5). This allows to compare the known lattice constant and the orientation of the substrate with these of the MBE grown

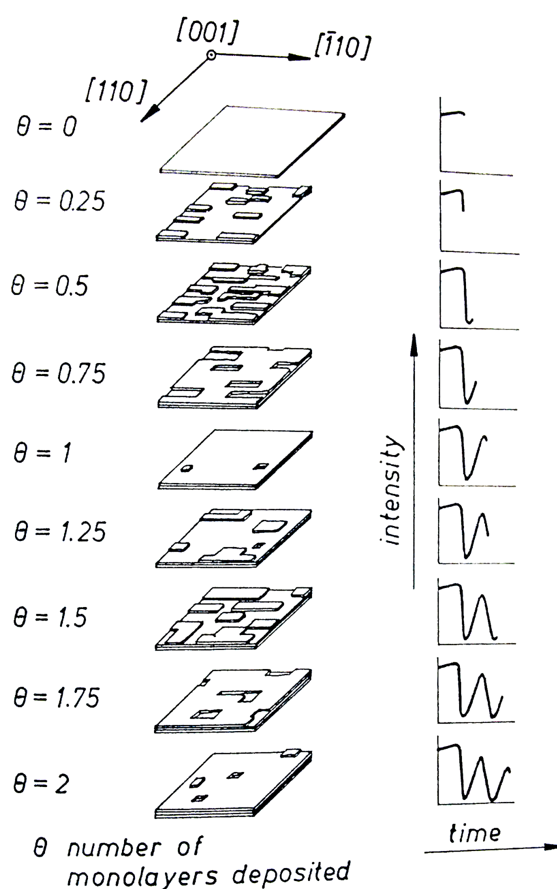

Fig. 3.7: Schematic of increasing coverage of GaAs(001) monolayers in relation to RHEED intensity oscillations, according to a nearly perfect layer-by-layer growth, taken from [HS96]. *(Reprinted from Surface Science, B.A. Joyce, et al., 168, 423-438, Copyright (1986), with permission from Elsevier; and Republished with permission of Springer Science and Bus Media B V, from Molecular beam epitaxy: fundamentals and current status, M.A. Herman, H. Sitter, 7, 2nd ed, 1996; permission conveyed through Copyright Clearance Center, Inc.)*

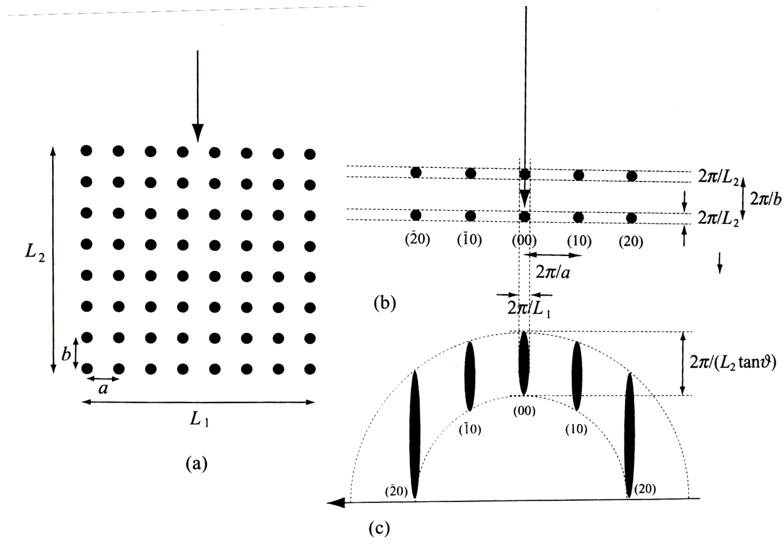

Fig. 3.8: Effect of finite crystalline lattice size L_1 and L_2 with the lattice constants a and b (a) on the reciprocal lattice rods (b) and the RHEED features on the screen (c), where the length of the RHEED streaks also depends on the glancing angle of incidence ϑ, taken from [IC04].

layer.

Fourth, in the case of a perfect 2D crystalline surface the width of the streaks is indirect proportional to the lateral size of the coherently scattering lattice as shown in Fig. 3.8 and thereby a measure of the crystallite-size of the layer. Bowing of the substrate, the experimental resolution of the RHEED system and crystal defects, e.g. as mosaicity-tilt, are additional sources of streak broadening.

Last but not least, a reconstructed surface lattice can be detected, if additional weaker lines occur between the main streaks, e.g. caused by a periodic arrangement of ad-atoms at the surface with a multiple lattice constant compared to the bulk material. Reconstructions on substrates or layers are formed at material characteristic temperatures and under specific cation- or anion- rich conditions. These are used to calibrate the temperature or to control the flux ratios of the applied molecular beams at the surface of the sample.

3.3 X-ray analysis techniques

X-ray diffraction (XRD) and X-ray reflection (XRR) are techniques for the destruction free analysis of bulk crystals and thin crystalline films by diffraction and reflection of X-rays at lattice planes and material interfaces. Mainly the structural properties of a crystal are probed by XRD and XRR, such as crystal symmetry, lattice parameters, composition, crystalline quality, surface/interface roughness, layer thickness, and layer structure of the sample.

Therefore a diffractometer with an eight bounce geometry is used to measure high resolution XRD (HRXRD) diffractograms using characteristic X-ray, e.g. Cu Kα1 (1.54056Å) [Bea67]. Figure 3.9 (a) shows a sketch of the used Panalytical X'pert MRD system with two detector optics for different resolutions. On the incident beam side, the Ge[220] four bounce monochromator reduces the broadening of the beam to about 6 arcsec. The installed high resolution triple axis analyzer, which is a three bounce channel cut Ge[220] crystal, allows to measure with a detector opening comparable to a slit of 12 arcsec (0.0036°) width. The detector opening for an optional slit optics of 0.8 mm is about 500 arcsec (0.14°), which is used to get a higher peak intensity at the cost of the angular resolution. The detector is a Si scintillation counter with a linear counting behavior up to 500000 counts per seconds. The used beam has a width of 1.0 mm and a height of 10.0 mm resulting in a macroscopic area which is probed. The angle between incident beam and the diffracted beam is labeled as 2θ. As sketched in fig. 3.9 (b), the sample holder enables an in-plane rotation ϕ and two out of plane rotations, ω in the plane and ψ orthogonal to each other, to position the sample in the required diffraction geometry.

3.3.1 X-ray diffraction (XRD)

A schematic of the diffraction of a X-ray beam by a crystalline structure is shown in fig. 3.10. The incoming X-ray beam is diffracted by the lattice planes of the crystal. The diffraction at different planes causes a difference in the length of the beam paths. The beams with different path lengths interfere with each other

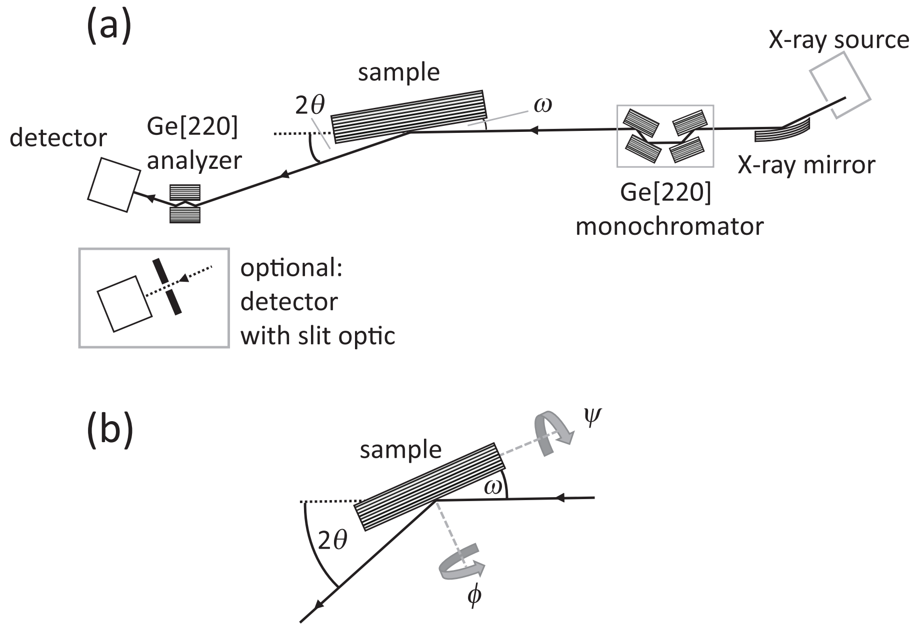

Fig. 3.9: Schematics of a HRXRD (after a panalytical X'Pert MRD) [War69]. (a) top view of the eight bounce X-ray beam path (4× monochromator + sample + 3× analyzer), as well as the optional slit optics for the detector. (b) Close up of the sample area with labeling of the incidence angle ω, detector angle 2θ, in-plane rotation angle ϕ, and out-of-plane rotation angle ψ.

resulting in destructive and constructive interference. They interfere constructive, if the difference in the length of the beam path is a multiple of the used X-ray wave length, as described by the Bragg equation:

$$\lambda = 2d_{hkl}sin(\theta), \tag{3.4}$$

where λ is the wavelength of the beam and d_{hkl} is the spacing between the diffracting lattice planes.

The reciprocal relation between d_{hkl} and $sin(\theta)$ ($\frac{1}{d_{hkl}} \propto sin(\theta)$) lead to a convenient description of the X-ray diffraction in the reciprocal space. Here, using the definition common in condensed matter physics, the relation between absolute value of the reciprocal lattice vector and the distance between planes (hkl), is given by

$$|\vec{G}| = \frac{2\pi}{d_{hkl}} \tag{3.5}$$

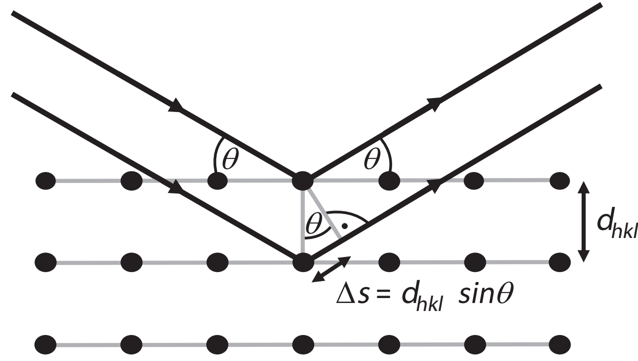

Fig. 3.10: Schematic of X-rays diffracted at crystal lattice planes separated by d_{hkl}. The difference of the beam path $\Delta s = 2d_{hkl}\ sin(\theta)$ results in constructive interference, if it coincide with the wavelength λ or multiple integers of it.

where $\vec{G}$ is the reciprocal lattice vector

$$\vec{G} = h\vec{a}_1^* + k\vec{a}_2^* + l\vec{a}_3^*, \tag{3.6}$$

with the primitive vectors of the reciprocal lattice

$$\vec{a}_1^* = 2\pi\frac{\vec{a}_2 \times \vec{a}_3}{\vec{a}_1(\vec{a}_2 \times \vec{a}_3)}; \vec{a}_2^* = 2\pi\frac{\vec{a}_3 \times \vec{a}_1}{\vec{a}_1(\vec{a}_2 \times \vec{a}_3)}; \vec{a}_3^* = 2\pi\frac{\vec{a}_1 \times \vec{a}_2}{\vec{a}_1(\vec{a}_2 \times \vec{a}_3)}, \tag{3.7}$$

which depend on the primitive vectors a_1, a_2, and a_3 of the Bravais lattice with the relation $\vec{a}_i\vec{a}_j^* = 2\pi\delta_{ij}$, where the Bravais lattice vector is $\vec{r} = x\vec{a}_1 + y\vec{a}_2 + z\vec{a}_3$ [STS+09, IL09].

In reciprocal space the diffraction condition is written as

$$\vec{G} = \Delta\vec{k} = \vec{k}_e - \vec{k}_i, \tag{3.8}$$

also known as the Laue condition. The wavevectors for the incident beam $\vec{k}_i$ and diffracted beam $\vec{k}_e$ have the same length $|\vec{k}_i| = |\vec{k}_e| = 2\pi\lambda^{-1}$ for elastic scattering. The wavevectors form a sphere with the radius $r = 2\pi\lambda^{-1}$ (Ewald sphere), where the diffraction condition is fulfilled, if both tips of the wavevectors lie on reciprocal lattice points connected by the reciprocal lattice vector $\vec{G}$ [STS+09, Kit13]. Figure 3.11 displays the construction of the Ewald sphere on the grid of the reciprocal

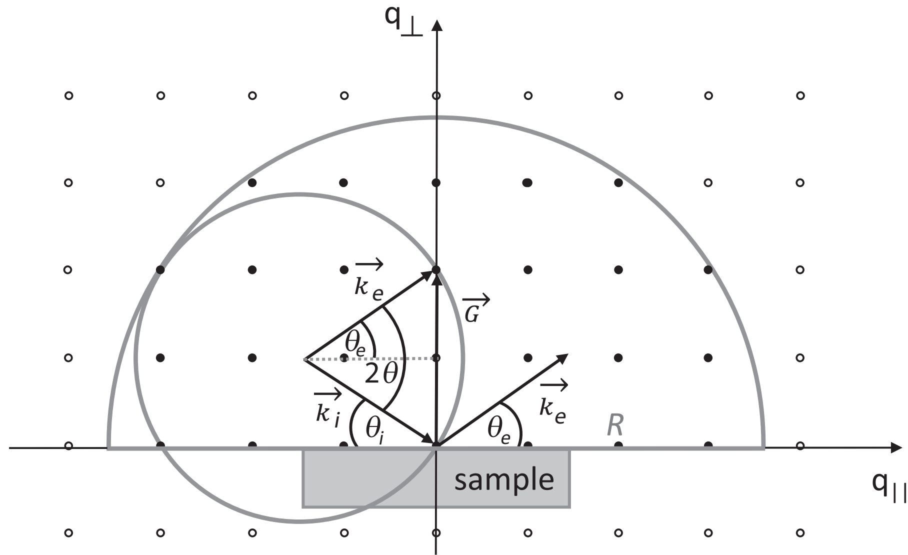

Fig. 3.11: Ewald construction with the Ewald sphere (radius $|k_{i,e}| = 2\pi\lambda^{-1}$) and the accessible hemisphere (radius $R = 4\pi\lambda^{-1}$) in reciprocal space. The reciprocal lattice points, which are not within the accessible hemisphere lie either behind the sample, or are not accessible due to the used wavelength.

lattice. The accessible area is limited by the used wavelength and the absorption of the sample itself, resulting in an accessible hemisphere with radius $R = 4\pi\lambda^{-1}$. The reciprocal lattice points within the hemisphere are not all accessible in a pure $2\theta-\omega$ geometry, therefore an additional inclination of the sample in ψ (see fig. 3.9) by the angle between symmetric and measured asymmetric plane is required. For example, (001) oriented Bi_2Se_3 on Si(111) or InP(111) substrates requires an inclination of 58° in ψ direction to measure a pole-scan of the asymmetric reflections of the Bi_2Se_3 $\{0\ 1\ 5\}$ planes, as indicated in figure 2.5. Pole-scans are applied to determine the lateral mosaicity-twist by measuring the FWHM and the amount of twin volume within the layer by measuring the integrated intensity of peaks corresponding to twin domains.

Symmetric reflections of homogeneous layers show in addition to the layer peak also fringes, as shown for the 0 0 3 reflection of Bi_2Se_3 in figure 3.12. The fringe period gives information about the layer thickness $d_{layer} = \frac{\lambda}{2(sin(\theta_{n+1})-sin(\theta_n))}$, where θ_n and θ_{n+1} are the positions of two neighboring fringe maxima and λ the used wavelength

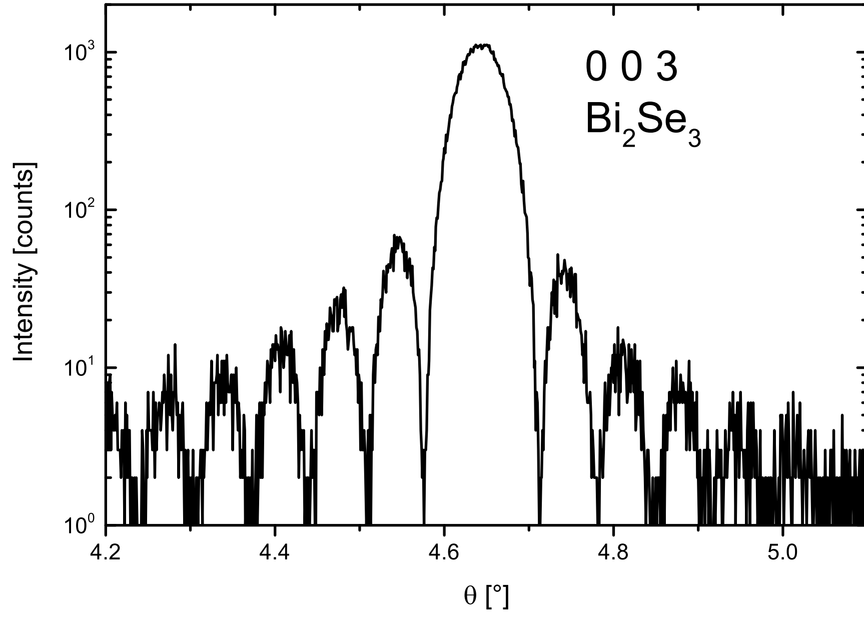

Fig. 3.12: XRD diffractogram of a 0 0 3 reflection of Bi_2Se_3 grown on InP(111)B exhibiting distinct thickness fringes.

[STS+09]. The equation

$$\frac{1}{d_{hkl}^2} = \frac{4}{3}\frac{h^2 + hk + k^2}{a^2} + \frac{l^2}{c^2} \tag{3.9}$$

deduced from equation 3.5, for hexagonal lattices with $a = b$, $\alpha = \beta = 90°$, and $\gamma = 120°$, is used together with the Bragg equation to obtain the lattice constants a and c from the measured Bragg reflection angles θ [War69]. Furthermore, rocking curves of symmetric reflections, where the detector is fixed at the angle of the Bragg reflection and the sample is inclined in $\pm\omega$, are studied to determine the out-of-plane mosaicity-tilt.

While the Bragg equation and Laue condition describe the relation between diffraction angle and distance of diffracting lattice planes, the intensity I of the reflections depends on the structure factor S_{hkl} of the material:

$$I \propto |S_{hkl}|^2 \tag{3.10}$$

with

$$S_{hkl} = \sum_{j=1}^{N} f_j e^{-i(\vec{G}\vec{r})} = \sum_{j=1}^{N} f_j e^{-2\pi i(hx_j + ky_j + lz_j)} \tag{3.11}$$

where f_j is the atomic form factor, describing the scattering contribution of each atom j within the unit cell at the position x_j, y_j, and z_j [Hun09, IL09]. The calculation of the structure factor of the V_2VI_3 TIs is more complicated than for the cubic zincblende materials since the 15 atomic positions in the R$\overline{3}$m symmetry (e.g. Se(2) 0;0;0, Se(1) 0;0;0.2117, and Bi 0;0;0.4008 [Nak63]) result in “unhandy” complex numbers for the exponents. The measured intensities of reflections additionally depend on several corrections, such as absorption, Lorenz- and polarization-factor, which are listed in the international tables of crystallography [PWHS99].

3.3.2 X-ray reflection (XRR)

While XRD describes the reflection of the X-ray beams at the lattice planes, XRR probes interference effects of reflections at interfaces close to the total reflection angle θ_C. Figure 3.13 shows a schematic of X-rays reflected at the substrate layer and the layer air interface. Constructive interference between the reflected beams is achieved if the difference of the path length is equal to the used wavelength or multiple integer of it. Figure 3.14 shows a typical XRR scan displaying the total reflection up to a critical angle θ_c (depending on the refracting indices of the two interfacing media) and distinct fringes, where the positions of neighboring maxima θ_m and θ_{m+1} correspond to the layer thickness by following equation (for θ_m significantly above θ_c):

$$d_{layer} = \lambda(2(sin(\theta_{m+1}) - sin(\theta_m))^{-1} \approx \lambda(2(\theta_{m+1} - \theta_m))^{-1}\text{[Bir06]}. \tag{3.12}$$

Here, both the interfaces between substrate and layer, as well as layer and air influence the measured intensity, e.g. by changing locally the incidence angle in the case of facets or by the presence of inhomogeneous layer thickness d_{layer} due to island growth (roughness). Simulation and fitting software is used to get detailed information about the interface roughnesses and layer thickness of the films. The

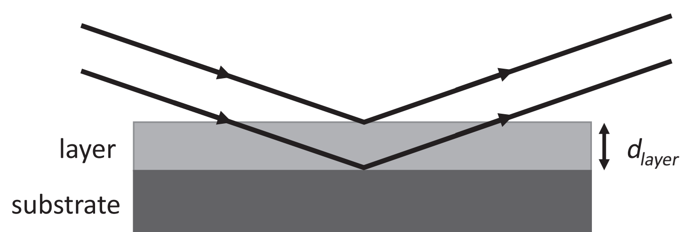

Fig. 3.13: Schematic of the X-rays reflected at the interfaces air/layer and layer/substrate. The difference of the path length of the beams results in interference between the reflections at the two interfaces.

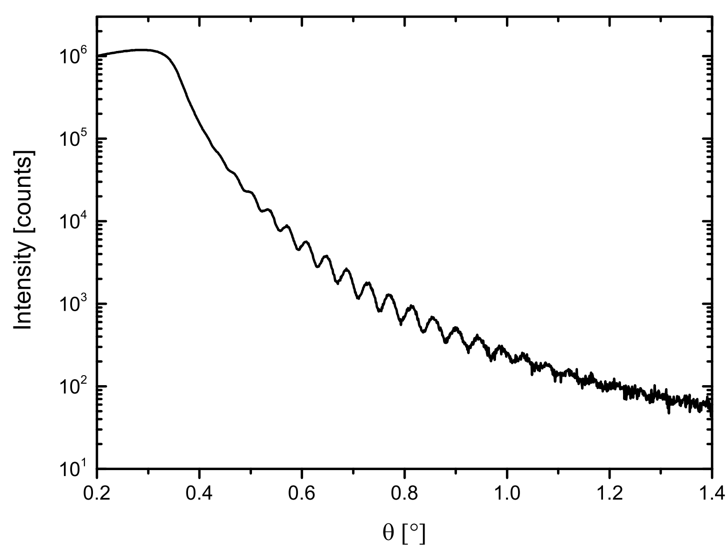

Fig. 3.14: XRR scan of a 93 nm Bi_2Se_3 layer grown on flat InP(111)A:Fe.

commercially available software “Leptos” from the company “Bruker” is utilized in this study.

3.4 Atomic force microscopy (AFM)

Atomic force microscopy is a surface sensitive technique to measure the topography of a sample. Therefore a tip with a small diameter is used in contact-, tapping-, or non-contact-mode. Figure 3.15 shows the schematic of an AFM setup, where a laser beam is reflected at the backside of the tip to measure the z-deflection of the cantilever. The used AFM is operated in non-contact mode (AC-mode) at a constant damping rate of the oscillating cantilever. Here the cantilever oscillates with its resonance frequency and its amplitude is damped by the van der Waals force between tip and sample depending on the distance between cantilever and sample surface. A z-feedback loop is used to readjust the distance between tip and sample with the z-piezo motor to keep the average distance Δz (damping rate) constant. The z-correction given by the z-feedback loop for each measured point results in the topography of the sample. The AFM scans several lines in the xy-plane of the sample to obtain a two dimensional height profile of the surface. The vertical resolution of an AFM allows to resolve height differences of atomic steps in z-direction, while the in plane resolution is limited due to the tip radius and the positioning accuracy of the piezo motor to few nanometers. Since the AFM is operated in air, the resolution depends also on ambient conditions, such as acoustic noise, vibrations, air moisture and air flow in the room, which have to be isolated or avoided to achieve the technical accessible resolution.

Using AFM enables to get information about the surface structure, the surface roughness, as well as defects of a crystalline layer as shown in this thesis. The surface roughness is given as a root mean square roughness (rms), which is the square root of the sum of the squared deviation in the z-height to the average height of all measured points N in the area of interest divided by the number of measured points N.

In addition to van der Waals force, also electric- and magnetic-forces between tip and surface can be measured with convenient cantilevers. In this thesis, the AFM measurements are realized using a DME DualScope 95-50 scanner equipped with Si cantilevers with a tip radius below 10 nm for non-contact mode to measure

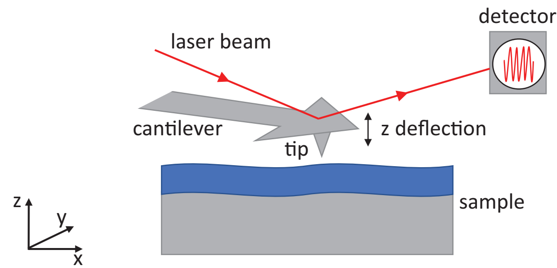

Fig. 3.15: Schematic of the atomic force microscopy, for measuring the z-deflection with a reflected laser beam in non-contact mode [Hun09].

the surface topography of the substrate and TI layers in ambient conditions. The resolution is limited by the tip diameter of about 20 nm in xy-direction and by the underground noise in z direction of 50-100 pm rms in our setup allowing to resolve steps with the height of an atomic layer.

3.5 Energy dispersive x-ray spectroscopy (EDX)

Energy dispersive X-ray spectroscopy (EDX) is a technique to study quantitatively the amount of elements in a sample by analysis of the characteristic x-rays . Figure 3.16 (a) displays how an electron beam ejects a core electron of the K shell, which leaves a void. This void is filled by an other electron, e.g. of the L shell [GNE+12]. This process produces K_α a photon with an energy, equal to the energy difference between the K and L shell $\Delta E = hf$, where h is the planck constant and f the frequency emitted light, which is characteristic for the measured element [STS+09]. To detect the x-ray photons it is common to use a Si(Li) or a silicon drift detector. A exemplary spectrum of bulk $Bi_{2-x}Sb_xSe_3$ on Si(111), displayed in Figure 3.16 (b), shows a broad area of bremsstrahlung and characteristic x-ray emission lines. The measured peak areas of the characteristic x-ray emission lines are proportional to the amount of atoms in the material. The spacial resolution of this measurement is limited to the pear-shaped emission volume, which has the diameter of few microns. To enlarge the surface sensitivity of EDX, low acceleration voltages (5-10 kV) for the electron beam, or measurements on inclined samples are used. Due to the need of an electron beam and high vacuum condition the EDX measurement is often implemented in a scanning electron microscope (SEM), which enables positioning of the electron beam at representative areas of the layer, or imperfections for defect analysis.

The used EDX detectors in this study are a silicon drift detector from “Oxford instruments” and a Si(Li) detector from “EDAX”, implemented in a “Zeiss Ultra Plus” SEM and in a “Phillips XL30” SEM, respectively.

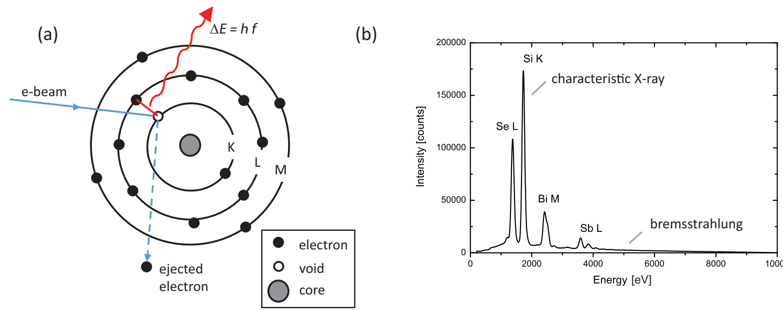

Fig. 3.16: Schematic of EDX: (a) generating characteristic x-ray emission lines with the energy ΔE by electron collision within a atom. (b) spectrum of a bulk $Bi_{2-x}Sb_xSe_3$ layer on Si(111) showing the characteristic x-ray emission lines of Se, Si, Bi, and Sb as well as the bremsstrahlung.

3.6 Lithography and magnetotransport

The lithography and magnetotransport measurements were conducted by Stefan Grauer et al. within the spintronics and quantum transport group of EP3. The layers were structured in a Hall bar geometry by wet chemical lithography, as shown in figure 3.17 (a). The layers were etched by a bromine-ethylene-glycol solution. The contact areas were metalized with either a Au/Ge- or Ti/Au-layer directly on the layer with an additional Au layer on top. The height of the contacting metal layers is adapted to exceed the layer thickness. After lithography, the samples are glued into a chip-carrier and the contacts are bonded to it with Au-wires.

The magnetotransport was measured in a cryostat under an out-of-plane magnetic field at 4.2 K. As shown in figure 3.17 the current is determined by the voltage U_R measured at a reference resistor R. The longitudinal voltage U_{xx} and the Hall voltage U_{xy} of the sample are measured in a 4-point geometry in an out-of-plane magnetic field B.

To extract the carrier density and carrier mobility of the layer a one carrier model is applied, which is not sufficient to describe the complex transport behavior within a TI, but it delivers a tool to compare the sample to sample variation depending on growth parameters. The slope of Hall resistance versus magnetic field R_{xy}/B is extracted from the high magnetic field region to determine the carrier concentration with the formula $n = \frac{B}{e \cdot d \cdot R_{xy}}$, where e is the charge of a electron and d the layer thickness [SN06]. The carrier mobility μ is determined by the formula $\mu = \frac{\sigma}{n \cdot e} =$

$\frac{1}{\rho \cdot n \cdot e} = \frac{l}{R_{xx}(B=0) \cdot b} \cdot \frac{R_{xy}}{B}$, where σ is the conductivity, ρ the resistivity, l the vertical distance of contacts 2 and 3 (600 μm), b the width of the Hall bar (200 μm), and $R_{xx}(B = 0)$ the longitudinal resistance at zero magnetic field [SN06].

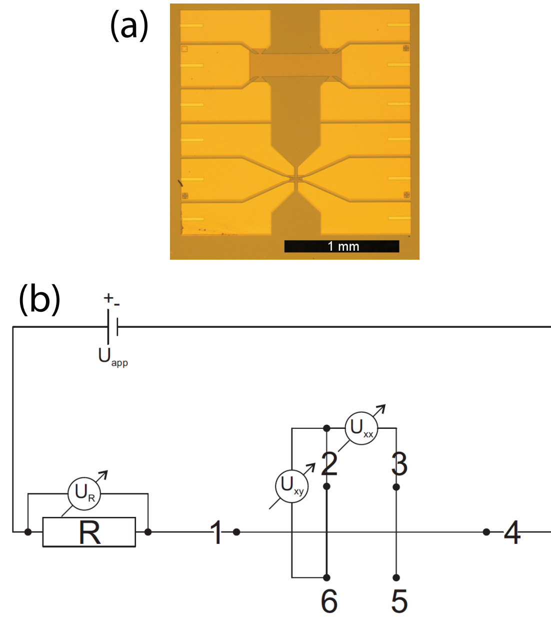

Fig. 3.17: (a) Image of a typical Hall bar layout used for the lithography process. (b) Schematic of the circuit used to measure magnetotransport [Gra10].

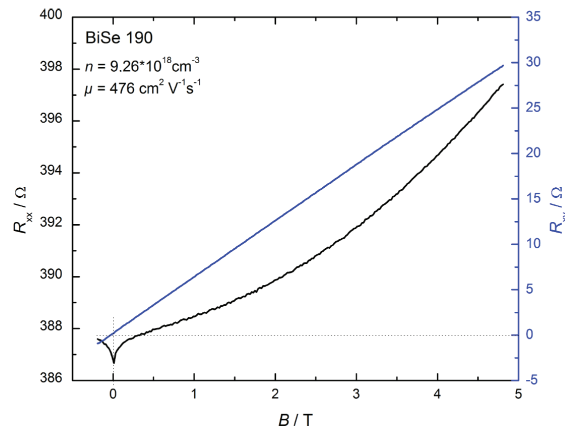

Fig. 3.18: Magneto transport measurement of a structured Bi_2Se_3 layer in Hall bar geometry. The longitudinal resistance (black) and the Hall resistance (blue) are plotted versus the applied field [Reu10].

4 Molecular beam epitaxial growth and characterization of Bi_2Se_3

In this chapter, molecular beam epitaxy is applied to precisely control the growth parameters for optimizing the structural crystalline and electrical properties of Bi_2Se_3. In addition, the influence of the substrate and its surface preparation on the structural quality of Bi_2Se_3 layers are analyzed. This contains different passivation techniques of the Si(111) surface, as well as the use of lattice matched InP(111) substrates with miscut and various surface roughnesses.

4.1 Bi_2Se_3 films on Si(111)

To grow Bi_2Se_3 on Si(111) the natural oxide layer of the substrate is removed by an ex-situ etch step prior introducing it into the MBE system. The etch step in 50% hydrofluoric acid removes the oxide layer and forms a hydrogen passivated surface. This hydrogen passivation is relatively robust against oxidation on a time scale of few minutes [FBB89]. However, the etched substrates are kept in nitrogen atmosphere directly after etching until they are loaded quickly into the MBE system to reduce oxidation.

Bi_2Se_3 layers were grown on three differently prepared Si(111) surfaces, a bismuth reconstructed, a selenium passivated, and a hydrogen passivated surface [ZQT+09, BKE+11, LGL+13].
To prepare a $\sqrt{3} \times \sqrt{3}$ Bi reconstruction, rotated in-plane by 30° to the Si $[1\bar{1}0]$ direction, a Si(111) 7×7 reconstruction is formed by heating the substrate to ap-

proximately 800°C. After cooling the substrate to 140°C an amorphous layer of Bi is grown on the Si(111) 7×7 surface, as indicated by a change from a streaky 7×7 reconstruction to a featureless RHEED screen. Then the substrate is heated to 400°C to desorb the excess of Bi and forms a Bi R30$\sqrt{3} \times \sqrt{3}$ reconstruction, which is accompanied by the evolution of a 1×1 RHEED pattern [Sch11].
The Se passivated surface is also prepared on a Si(111) 7×7 reconstruction at a substrate temperature of approximately 110°C, and does not need an additional annealing step since the excess of Se desorbs at this substrate temperature.
The hydrogen passivation of Si(111) is formed ex-situ by the etch step with hydrofluoric acid, as described above and does not need any further in-situ process prior growth.

After the in-situ substrate preparation, the growth temperature is achieved by a temperature ramp of about 20°C per minute. Bi_2Se_3 growth on H passivated, or Bi reconstructed Si surfaces starts at the substrate temperature T_{sub}=300°C by opening the Bi- and Se-shutter simultaneously.
In the case of the Se passivated substrate a two step growth is applied, which includes a growth of 2 QL Bi_2Se_3 at 110°C to prevent desorption of the Se-passivation. This is followed by heating to the second growth temperature $T_{sub} = 300$°C in Se-atmosphere. At $T_{sub} = 300$°C the second Bi_2Se_3 growth is initiated by opening the Bi shutter. The layers are grown in Se rich growth conditions to obtain the Bi_2Se_3 phase of the bismuth selenides, which is the selenium richest phase, as well as to reduce Se vacancies. During growth a streaky RHEED pattern is observed for the three layers on differently prepared substrates. The growth on Bi- or H-passivated substrates results in rotation dependent streak separation with a factor of $\sqrt{3}$ every 30°, as expected for a hexagonal surface lattice, while for growth on Se-passivated substrates the streaks of both orientations of Bi_2Se_3 are visible ([-210] and [-110]) for a rotation by 30° indicating a large mosaicity-twist within the layer.

The influence of the Si(111) surface preparation on the structural quality of the Bi_2Se_3 layers is determined by XRD measurements of three representative bulk lay-

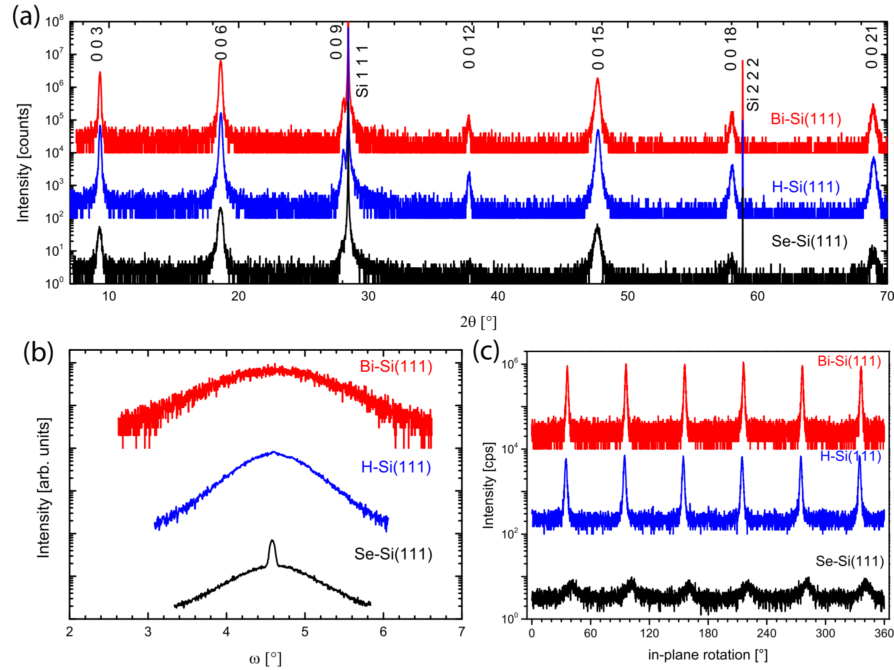

Fig. 4.1: XRD of Bi_2Se_3 bulk layers grown on differently prepared Si(111) surfaces as labeled in the graphs. (a) θ-2θ diffractogram showing the reflections of the (0 0 l) Bi_2Se_3 planes and the substrate reflections. (b) Rocking curve diffractograms of the 0 0 3 Bi_2Se_3 reflection. (c) In-plane rotation scan of the reflections of the {0 1 5} Bi_2Se_3 planes. Curves are shifted for clarity.

ers. All substrate preparations result in single phase Bi_2Se_3 layers with the [001] direction well aligned to the Si [111] direction as shown in figure 4.1 (a).

Figure 4.1 (b) shows rocking curves of the symmetric 0 0 6 Bi_2Se_3 reflection, which is a measure of the out-of-plane mosaicity tilt. The FWHM of the rocking curves for growth on Bi-, and H-passivated Si(111) are 1.4°, and 0.8°, respectively. In contrast to the other layers the growth on Se-passivated Si(111) results in a sharp peak of 0.086° FWHM , which is already limited due to the resolution of the XRD, and a broad peak with 0.97° FWHM. The area of the sharp peak is 16% of the total area of the double peak.

The in-plane mosaicity-twist is determined by XRD pole scans of asymmetric reflections of {0 1 5} Bi_2Se_3 planes shown in Fig. 4.1 (c). These reflections appear six times every 60° instead of the expected three times for single crystalline Bi_2Se_3 with $R\bar{3}m$ symmetry (see chapter 2), which is a sign of twinning within the layers. The FWHMs of the reflections for in-plane rotation are 1.7°, 10°, and 1.9° for Bi-, Se-,

and H-passivated Si substrates, respectively. In all cases, one of the peak triplets is measured at the same in-plane rotation angles as the reflections of the {0 0 4} Si planes proving the same in-plane orientation of the Si and Bi_2Se_3 hexagonal surface lattices. The relatively high in-plane twist (compared to zincblende heterostructures) observed for growth on Bi-, and H-passivated Si, most likely compensates the mismatch in lattice parameter between the hexagonal lattices of the Si(111) substrate and the layer of 7.8%. The Se-passivation seems to partially mask the substrate lattice resulting in the observed in-plane twist of 10°, which is about a factor of five higher than for the layers grown on Bi-, and H-passivated Si.

The n-type carrier concentrations (mobilities) of the layers measured by magneto transport at 4K are 1.1×10^{19} cm^{-3} ($821\frac{cm^2}{Vs}$), 2.0×10^{19} cm^{-3} ($248\frac{cm^2}{Vs}$), and 1.7×10^{19} cm^{-3} ($830\frac{cm^2}{Vs}$) for growth on Bi-, Se-, and H-passivated Si substrates, respectively. These values compare well to literature values of MBE grown Bi_2Se_3 on Si(111) [LWK+10, HXW+11]. The low electron mobility in the Bi_2Se_3 layer on Se-passivated Si(111) substrate seems to be related to the low layer quality, concerning mosaicity-twist.

In conclusion, growth parameters for the three surface preparations were determined allowing the growth of single phase Bi_2Se_3 with the [001] direction well oriented to the [111] direction of Si. However, the layers contain twin domains and the crystalline orientation differs depending on the substrate surface preparation.

For the Bi- and H-passivation the hexagonal lattices of substrate and layer are oriented to each other within a twist of below 2° proving the influence of the substrate on the layer orientation, even at a lattice mismatch of 7.8%. The Se passivation seems to partially screen this influence of the substrate lattice on the layer resulting in a large in-plane mosaicity-twist of 10°. This screening of the substrate lattice allows a portion of the vdW bonded domains (about 16% of the volume of the layer) to orient homogeneously to the flat substrate surface as determined by the sharp XRD rocking curve attesting a small out-of-plane tilt compared to the layers grown on Bi- and H-passivated substrates. Here, it is important to note, that for

the V_2VI_3 layers, which are bonded by vdW force to the substrate, not only the out-of-plane tilt, but also the in-plane twist has to be measured to determine the structural crystalline quality of the layer.

In addition the transport results show that the layers with both, good in-plane and out-of-plane orientation, have lower carrier concentration, as well as higher carrier mobilities, than the sample with the sharpest rocking curve peak, but worst in-plane orientation. Nevertheless, the carrier concentration of all the layers is above 1×10^{19} cm^{-3} presumably caused by structural imperfections, such as the twin domains, and the high level of mosaicity within the layers observed by XRD, as well as point defects described in chapter 2. Therefore the growth on lattice matched substrate (section 4.2), as well as suppression of twinning (section 4.3) is studied to improve the structural crystalline quality.

4.2 Bi_2Se_3 grown on lattice matched InP(111)

The main results presented in this section are published in international journals [TSB+12, STK+13, LSE+14, TSL+14].

As shown in chapter 4.1, the substrate and its surface preparation strongly influence the structural crystalline quality of the vdW bonded Bi_2Se_3 layers. Therefore, the use of lattice matched substrates is studied to improve the structural layer quality. As a substrate, which matches to the hexagonal lattice of Bi_2Se_3, we focus on InP(111) with a lateral lattice mismatch of 0.2% (as shown in figure 2.6).

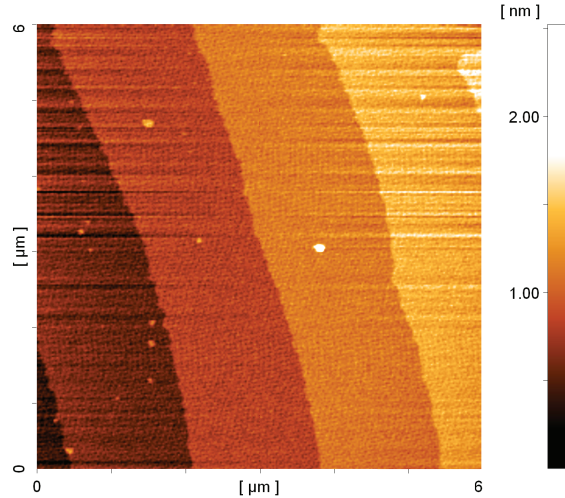

Fig. 4.2: AFM image (6×6 μm) of the surface of InP(111)B after oxide desorption in As atmosphere showing bi-layer steps on the surface. (The horizontal lines are artifacts of the AFM measurement.)

InP is a III-V zincblende semiconductor commercially available as a substrate ready for epitaxy. The {111} oriented InP substrates can differ in their surface termination, e.g. (111) and (-1-1-1). The surfaces are either indium- or phosphorous-terminated, labeled as (111)A and (111)B, respectively. An other important point is the smoothness of the substrates. Arising from misalignment in the fabrication process of the wafers, the InP substrates come along with a miscut to the (111) surface plane. The miscut results in InP bi-layer steps with a height of about 0.34 nm at the surface.

In this chapter undoped InP(111)B substrates were used to grow Bi_2Se_3. To characterize the surface of the substrate the natural oxide layer was thermally desorbed in-situ in As atmosphere in a III-V MBE chamber. Then the substrate was unloaded from the UHV system and quickly measured by ex-situ atomic force microscopy to avoid excessive oxidation of the surface. The AFM image in figure 4.2 displays atomically flat terraces connected by steps of 0.3 nm height corresponding to the height of an InP(111) bi-layer step (0.34 nm). The terrace width is about 1.5 μm and the miscut calculated from the terrace width and the step height is 0.013°. The observed 0.013° miscut to the (111) plane reveals that the surface is well oriented to the (111) planes, as the substrate specifications allow a miscut up to ± 0.2°.

Prior to the growth, the InP substrates were etched in 50 % hydrofluoric acid to remove the oxide layer and loaded to the MBE system, as described for the Si substrates in chapter 4.1. Two different growth methods were applied to obtain Bi_2Se_3 layers on InP(111)B.
First, the growth is divided in two parts at different substrate temperatures. Therefore the substrate is heated to 250°C to grow two QLs, as a protection layer against possible phosphorus out-diffusion from the substrate. Then the two QLs are kept in Se atmosphere and heated to the 300°C. The two QLs are annealed in Se atmosphere for one hour at 300°C before the second growth step. The growth time of the second growth step is varied to get different layer thicknesses, i.e. 22 min, 1 h, 3 h, and 6 h for samples A, B, C, and D, respectively.
Second the growth is performed at a constant substrate temperature, where the substrate is directly heated to 300°C. The growth time is 1 h for sample E, which makes it comparable to sample B with the two step growth start.
The growth parameters for both methods were chosen to obtain a growth rate of approximately 1 nm per minute at Se rich conditions. Therefore a BEP of $p_{Se} = 6 \times 10^{-6}$ mbar and $p_{Bi} = 2 \times 10^{-7}$ mbar was applied during growth. After growth, the samples were cooled from growth temperature to 140°C in Se atmosphere to prevent creating Se vacancies by Se out-diffusion after growth.

The growth start of sample B is monitored by RHEED (see figure 4.3 (a)) showing two distinct intensity oscillations of the specular spot during the low temperature growth. These two oscillations are attributed to the growth of two QLs. After closing the Bi shutter the intensity of the RHEED increases for 25 s before it stays at a constant level. After the first growth step, the sample is heated to the substrate temperature 300°C. At the second growth step, again RHEED intensity oscillations are visible, decreasing in amplitude. Within four periods no more intensity oscillations are detectable, suggesting, that the growth of Bi_2Se_3 takes place at different height levels (terraces) causing a nearly constant reflectivity of the surface after growth of 4 QLs, as described in chapter RHEED 3.2. Extrapolating the period of RHEED intensity oscillations, assuming the growth of one QL corresponds to one oscillation period, results in film thicknesses of $d_A = 19$ nm, $d_B = 54$ nm, $d_C = 166$ nm, $d_D = 315$ nm, and $d_E = 53$ nm, for sample A, B, C, D,and E, respectively.
RHEED patterns show streaks and Kikuchi lines during the growth (see figure 4.3 (b) and (c)). The full width at half maximum (FWHM) of the streaks decrease with increasing layer thickness, indicating an increase of the size of surface domains contributing to the diffraction (see chapter 3.2). Figure 4.4 shows a SEM image of the surface of sample B after growth corresponding to the RHEED pattern shown in figure 4.3 (b) and (c). The surface is composed of triangular structures rotated by 60° to each other, as indicated by the red and green color. These triangular structures have side lengths of up to approximately 1 μm and several smaller triangular structures grow on top, separated by steps with terrace widths of up to 200 nm.

The as grown layers are measured by AFM. Figures 4.3 (d), (e), (f), and (g) show the surface morphology of sample A, B, C, and D, respectively. The surfaces of the layers consist of triangular structures, which are in-plane rotated to each other by 60°, as also shown in figure 4.4 by SEM. Between differently oriented triangular structures trenches of several nm depth are observed. These different orientation of the triangular structures is likely the result of twinning. The AFM measurements

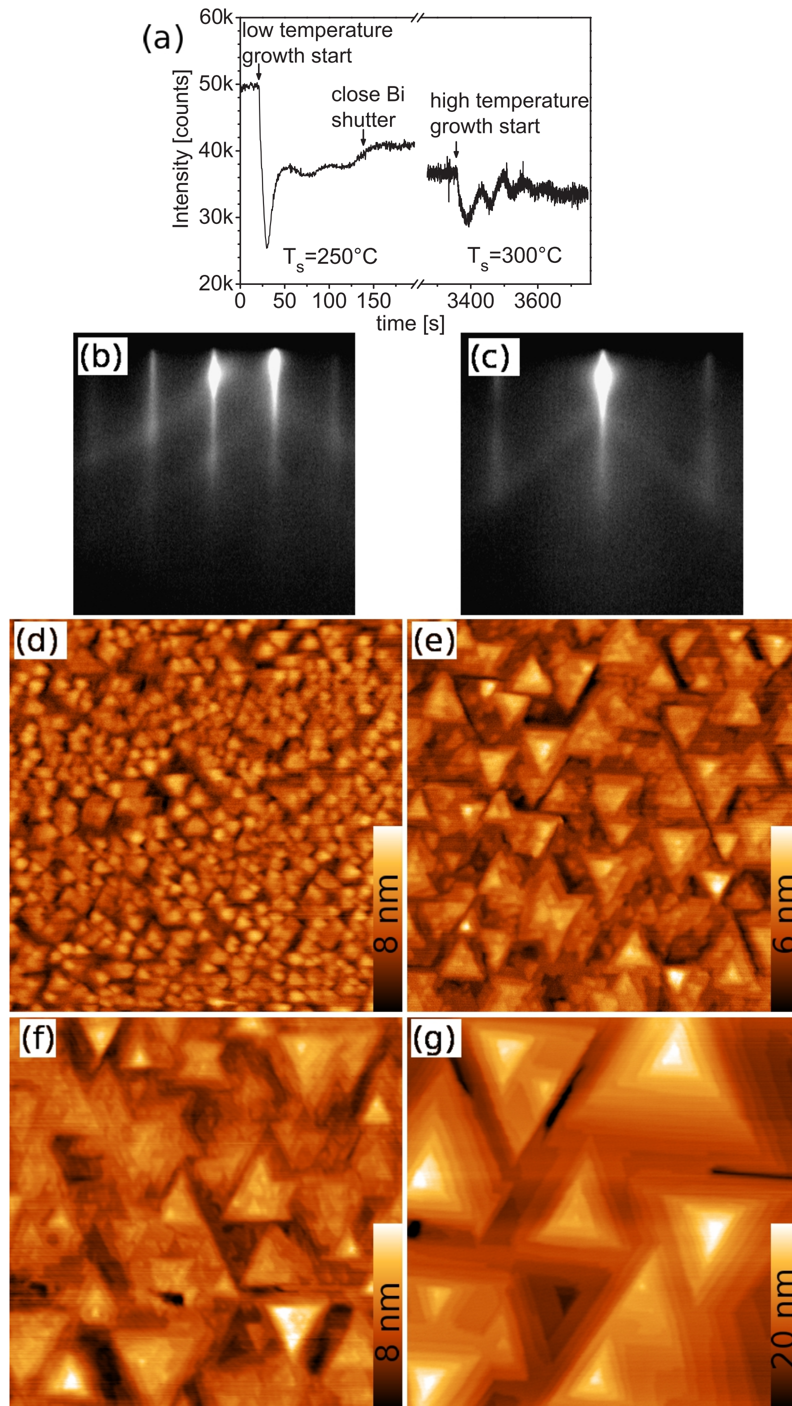

Fig. 4.3: (a) RHEED intensity oscillation of the specular spot of sample B, during the growth starts at T_{sub} =250°C and 300°C . RHEED images of sample B after the growth of Bi_2Se_3 taken along the (b) $[0\bar{1}1]$ and (c) $[1\bar{2}1]$ direction of the substrate. AFM images (7×7 μm) of the surfaces of Bi_2Se_3 for (d) sample A, (e) sample B, (f) sample C, and (g) sample D [STK+13].

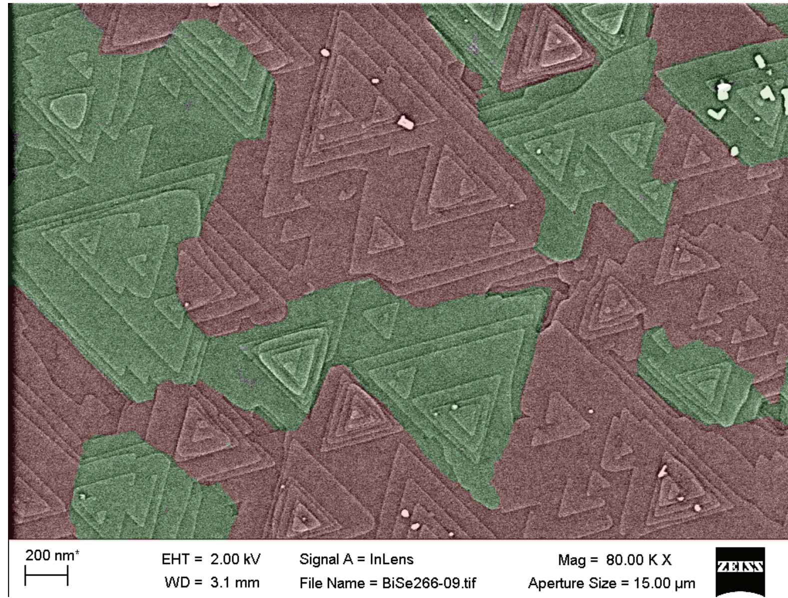

Fig. 4.4: SEM image of the surface of sample B after growth. The differently oriented triangular structures are artificially colored as a guide for the eye.

reveal that the steps observed in SEM have a height of approximately 1 nm, which corresponds to the height of 1 QL (0.95 nm) and that the terraces are atomically flat. Furthermore the side length of the triangular structures increase with the layer thickness. This observation might be explained by over growth of twin domains and merging of equally oriented domains during MBE.

HRXRD analyses reveal the structural quality of the Bi_2Se_3 films grown on InP(111)B. The wide range θ-2θ diffractograms (see inset figure 4.5 (a)) of the samples show the reflections corresponding to the (0 0 l) planes ($l = 3n$, $n \in \mathbb{N}_1$) of the layer and the 1 1 1 and 2 2 2 substrate reflections. Other peaks are absent in the diffractograms confirming that no other phases than Bi_2Se_3 of bismuth selenide are present within the sensitivity limit of HRXRD and that the [111] axis of InP is parallel oriented to the [001] axis of the hexagonal Bi_2Se_3 lattice. The higher resolution diffractogram shown in figure 4.5 (a) of the 0 0 3 reflection reveals distinct oscillations and a broadening of the peaks in dependence of the layer thickness. The period of these fringes (as described in chapter 3.3) corresponds to a homogeneous layer thicknesses of $d_A = 24$ nm, $d_B = 63$ nm, $d_C = 159$ nm, $d_D = 250$ nm, and $d_E = 66$ nm, for sample A trough E, respectively. The layer thicknesses measured

by HRXRD are consistent with the thickness extracted from RHEED Intensity oscillations, when taking into account that only few oscillation periods at the growth start were measured and extrapolated over the whole growth time.

Figure 4.5 (b) shows a HRXRD rocking curve of the 0 0 3 reflection of sample D. The diffractogram consists of a very sharp peak with a FWHM of 13 arc sec (which is close to the resolution limit of the used HRXRD diffractometer) and a broader peak with a FWHM of 0.1° (360 arc sec). The peak intensity area of the sharp peak is 86 % suggesting that the layer is preferably oriented within a very small out of plane mosaicity-tilt. The inset of figure 4.5 (b) shows the FWHM of the 0 0 3 reflections in dependence of the layer thickness. The FWHM decreases with increasing layer thickness, which is attributed to the better out-of-plane orientation with increasing domain size as measured by AFM. In addition the comparison between sample B and E with different growth start and comparable layer thickness does not show any significant difference in the FWHM of the rocking curve. This suggests that not the two step growth start with the annealing procedure is responsible for the small ω peak widths, but rather the layer thickness and the choice of substrate.

The reciprocal space map of the 0 0 3 reflection in figure 4.6 (a) clearly shows the sharp peak with the layer thickness fringes in Q_l direction and the broad background with the shoulders elongated in Q_h direction. The shoulders and the background could be related to any combination of defects causing tilts at the interface to InP, as well as at the domain boundaries, or finite size effects of domains [KFA95].

The XRD in-plane rotation scans of the asymmetric {0 1 5} layer planes of Bi_2Se_3 and {0 0 2} substrate planes are shown in figure 4.6(b). The substrate reflections show a three fold symmetry with the in-plane ϕ peak positions matching to one triplet of the peaks observed for Bi_2Se_3. This reveals that the hexagonal lattice of the layer is oriented to that of the InP substrate. The orientation to the substrate is within an in-plane twist of 0.07°, measured by the FWHM of the 0 1 5 reflection of sample D shown in the inset of figure 4.6 (b). The 0 1 5 reflection of the layer is expected to occur every 120°C in a single crystalline layer. Instead a six fold symmetry is observed, as for the growth on Si(111) studied in chapter 4.1. This

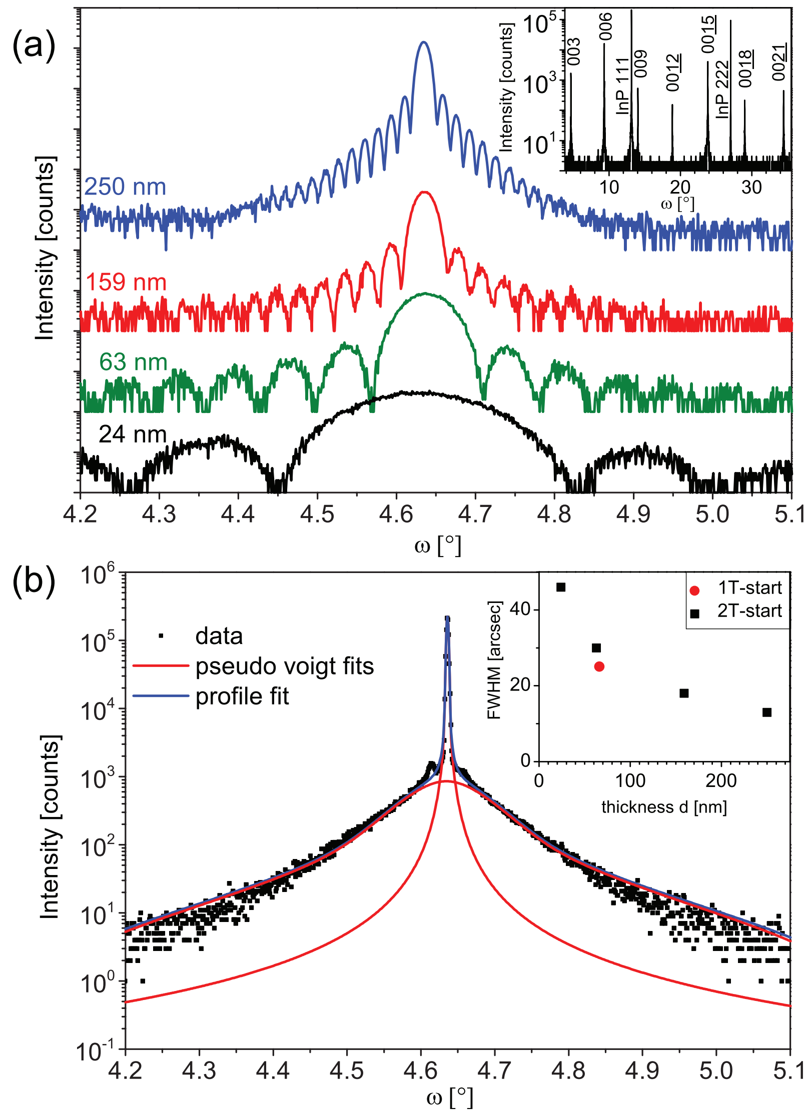

Fig. 4.5: HRXRD analysis of the Bi_2Se_3 grown on InP(111)B. (a) θ-2θ diffractograms of the 0 0 3 reflection of the samples A, B, C, and D showing distinct fringes corresponding to the various layer thicknesses, as indicated (subsequent curves offset by two decades for clarity). The inset shows a wide range θ-2θ diffractogram confirming the absence of other phases than Bi_2Se_3. (b) Rocking curve of sample D showing an intense sharp peak with a peak width of 13 arc sec and a weak broad background with a FWHM of 0.1° (≈360 arc sec) as determined by pseudo Voigt fits (red). The profile fit (blue) is the superstition of the two fits. The inset shows the FWHMs of the samples A through E grown with a one step start (1T-start) and a two step start (2T-start) plotted against the layer thickness [STK+13].

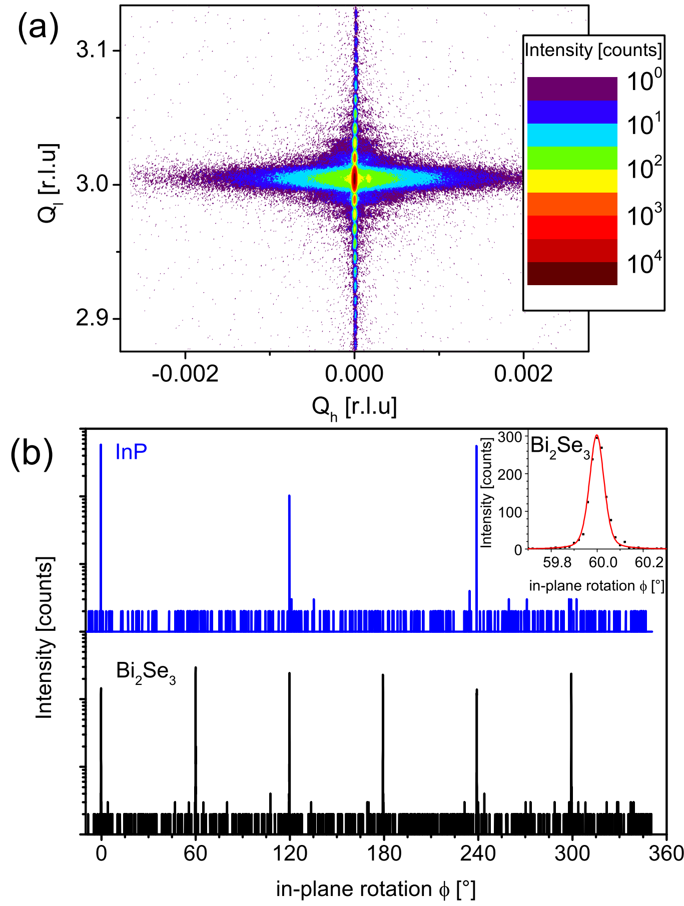

Fig. 4.6: (a) Reciprocal space map of the 0 0 3 Bi_2Se_3 reflection of sample D. The fringes, as well as the sharp rocking curve peak with the broad background and shoulders are clearly visible. (b) Pole scan of the asymmetric {0 1 5} layer planes and {0 0 2} substrate planes. The sample was rotated in-plane (ϕ) by 360° under the expected Bragg condition of the substrate (ψ = 54.74°) and layer (ψ = 58°) reflections. The Inset shows an enlargement of a 0 1 5 Bi_2Se_3 reflection with a FWHM of 0.07° [STK+13].

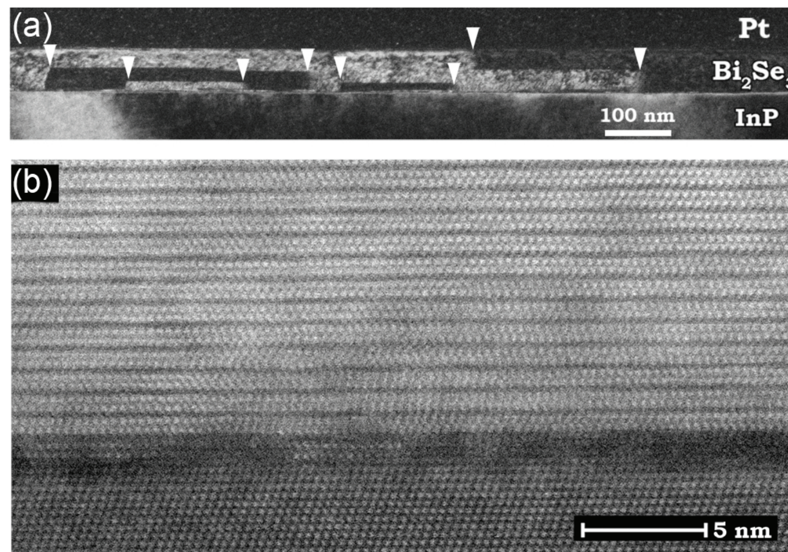

Fig. 4.7: TEM analysis of sample B. (a) Dark-field TEM image with white arrows indicating the twin boundaries. (b) Cross-sectional HAADF-STEM image showing the interface region of Bi_2Se_3 and InP within a single domain at atomic resolution [STK+13].

observation is explained by twinning, caused by the presence of both stacking orders ABC and ACB within the film. Apparently the first Se layer (A site) is well oriented to the hexagonal substrate surface, whereas the position of the first Bi layer (B or C site) is not determined through the weak van der Waals bonds to the InP substrate, causing that both stacking orders ABC and ACB are present in the film.

Transmission electron microscopy (TEM) analysis of sample B is shown in figure 4.7. The cross-sectional dark field TEM image (see figure 4.7 (a)) reveals the twinned domains in the film as illustrated by the bright and dark areas within the layer. Lamellar as well as rotational twin domain are present [TSB+12], with decreasing number of twin domain boundaries for increasing distance to the substrate, supporting the previously suggested mechanism of merging and overgrowth of twin domains. Figure 4.7 (b) shows a high-angle annular dark field STEM image of the interface region. The first QL exhibits regions with higher and lower crystalline quality followed by well-crystallized QLs.

TEM analysis performed by a probe-corrected scanning TEM (STEM) reveal that the first QL layers consist of small misaligned Bi_2Se_3 domains [TSL+14]. The mis-

aligned domains lower the contrast and the apparent resolution of the high-angle annular dark field (HAADF)-STEM images, making the interface region look amorphous. The layer of small misaligned Bi_2Se_3 domains varies between 0 and 2 QL in thickness, suggesting that the growth starts at many crystallization points, which merge and are overgrown within 2 QLs. An other defect is shown to persist at the bi-layer steps of InP(111)B substrate (also see figure 4.2), where the 3.4 Å bi-layer substrate step meets the 9.5 Å QL. To overcome the difference in height a seven layer (Bi_3Se_4) is formed at the step, as shown in figure 4.8. This interface defect represents an additional source of free electrons in the thin film.

The growth of homogeneous well oriented Bi_2Se_3 on InP(111) substrate and the precise layer thickness control obtained by the XRD measurements enabled to grow a series of thin layers , i.e. 2-, 3-, 4-,5-, and 6-QLs with a one step start at 300°C. These layers were studied by spin resolved ARPES and revealed the thickness dependence of the band dispersion of the topological surface states from bulk to thin films in the quantum tunneling limit, as described in chapter 2 [LSE+14]. Figure 4.9 shows spin integrated ARPES band maps of the layers taken at two different photon energies. The 6 QL thick film shows the bulk conduction band, the bulk valance band, and the Dirac cone of the topological surface states, as expected from bulk layers. For the thinner films the two surface states interact with each other via quantum tunneling and an energy gap of the surface states opens, which increases with decreasing layer thickness (see figure 4.9).

The electrical properties of Bi_2Se_3 grown on InP(111) are investigated by magneto transport of exfoliated flakes, to avoid an electrical bypass trough the undoped InP(111)B substrate. The carrier concentration of $9\times10^{18}\text{cm}^{-3}$ is slightly lower and the electron mobility of 1300 $\frac{cm^2}{Vs}$ is a factor of 1.5 higher, than those observed for growth of Bi_2Se_3 on Si(111) substrates (see chapter 4.1).

In summary, the growth of Bi_2Se_3 on the lattice matched InP(111) increases the structural quality of the TI, with regard to the mosaicity -tilt, -twist and -size.

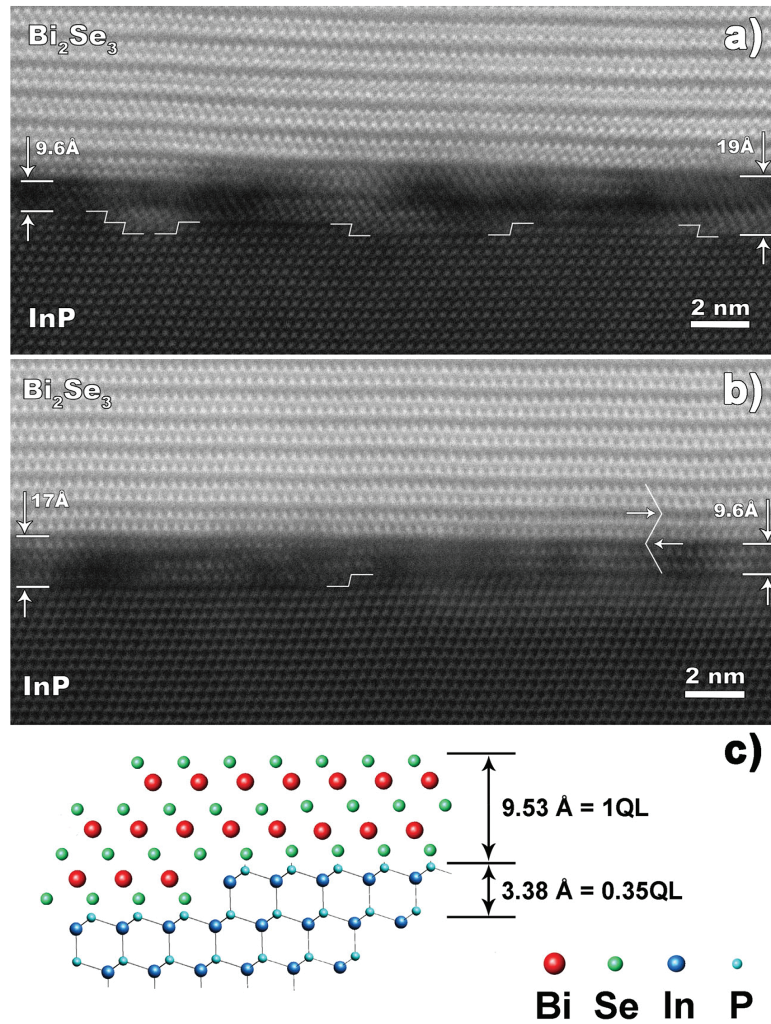

Fig. 4.8: (a) and (b) Crossectional HAADF-STEM analysis of the interface region of Bi_2Se_3 and InP (sample B). The horizontal arrows and the kinks in zig-zag lines point out the boundaries between lamellar twins. Step-shaped lines outline bi-layer steps of the InP substrate surface. (c) Sketch of a seven layer (Bi_3Se_4 cluster) formed at a bi-layer step of InP [TSL+14].

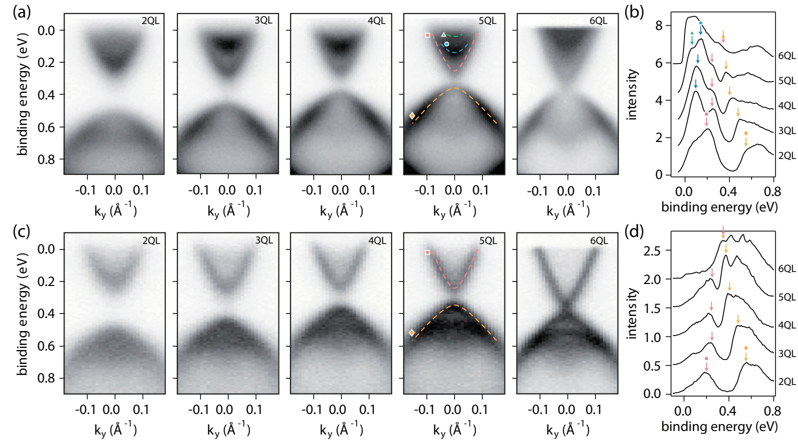

Fig. 4.9: Spin integrated band dispersion of Bi_2Se_3 grown on InP(111) in the two to six QL range taken at (a) 20 eV and (c)50 eV photon energy measured by spin resolved ARPES. The corresponding energy distribution curves at $\overline{\Gamma}$ (b) and (c) are plotted on the right side. The colored arrows indicate the position of the bands shown in the band dispersions [LSE+14].

This results in films with homogenous layer-thickness and well aligned crystalline layer-substrate interface. Crystal defects, such as the twinning observed for Si(111), are still present in the films grown on InP(111). The improvement of the structural layer quality has only a small impact on the carrier concentration, while the carrier mobility increases.

4.3 Twin suppression in Bi_2Se_3 films on InP

4.3.1 Bi_2Se_3 on 2° miscut InP(111) substrate

As shown in Chapters 4.1 and 4.2, as well as in literature [LWK+10], twinning is a growth defect present in MBE grown Bi_2Se_3 and other V_2VI_3 TIs. A technique to suppress twinning in epitaxially grown layers, e.g. in zincblende- or diamond-structure materials [ACF+96], is using miscut substrates, which is supposed to transfer the stacking information of the substrate at its surface steps to the layer.

To apply this technique to the growth of Bi_2Se_3, InP(111)B:Fe substrates with a miscut of 2° in [-1-12] direction to the (111) surface are used. The mean terrace width between bi-layer steps on the 2° miscut substrate is approximately 10 nm, with a step height of about 0.34 nm. The InP(111)B substrates are semi-insulating, due to the Fe doping acting as deep acceptors [FNS79], to allow magnetotransport measurements without bypass through the substrate. The applied ex-situ substrate preparation is the same as for the InP(111) wafers described in chapter 4.2 ($T_{sub} \leq 300°$). Both a one- or a two-temperature start was applied to grow samples with 60 nm Bi_2Se_3 layers on the miscut substrates at a growth speed of approximately 1 nm per minute. After growth sharp RHEED streaks are displayed on the screen and XRD confirms the growth of Bi_2Se_3.

Figure 4.10 shows a typical SEM image of the surface of the Bi_2Se_3 layer grown on a miscut substrate. Along the miscut direction (from the right hand side of the image to the left hand side) straight steps are visible. Assuming that the steps are QL steps of 0.954 nm height, the width of the terraces correspond well to the expected height difference on the substrate surface of about 1 nm every 30 nm due to the substrate miscut. Besides straight step-edges in [-110] direction of the substrate, perpendicular to the miscut direction, which originate from triangular structures facing with one vertex in miscut direction, also kinked steps are present corresponding to triangular structures rotated by 60°, as indicated in Figure 4.10.

The presence of the two differently oriented structures at the surface suggests that the Bi_2Se_3 layer contains twins, as verified by XRD in-plane rotation scans

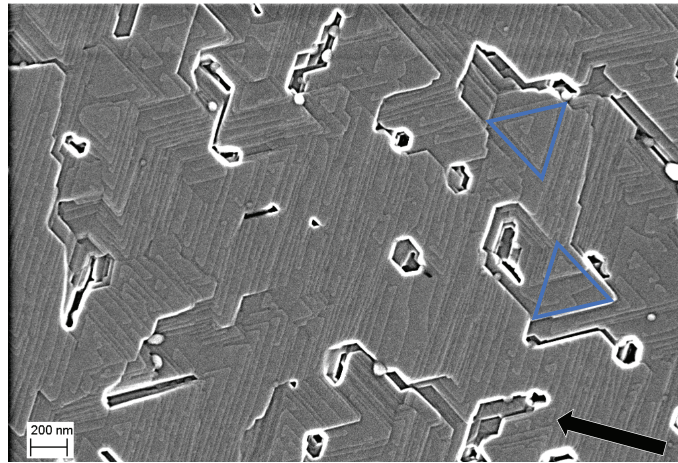

Fig. 4.10: SEM image of a 60 nm Bi_2Se_3 layer grown on InP(111)B:Fe substrates with a miscut of 2° in [-1-12] direction (black arrow) to the (111)B plane. Straight and kinked steps are visible resulting from differently oriented triangle islands (as illustrated by the blue triangles). The bright areas highlight the enhanced emission of electrons from edges of trenches, which are formed between differently oriented islands.

revealing a six fold symmetry of the {0 1 5} reflections.

Apparently the step height of 0.34 nm on the miscut substrates is not sufficient to transfer the stacking information from the substrate to the QL, suggesting that the steps are overgrown, as shown for the flat substrates in section 4.2. Therefore rough substrates with step heights exceeding the height of a QL are studied to suppress the twinning, as described in section 4.3.2.

4.3.2 Bi_2Se_3 on rough InP(111) substrate

The main results presented in this section are already published in international journals [TSB+13, TSL+14, WJF+16].

As the miscut InP(111)B:Fe substrates with its bi-layer steps do not provide a uniform stacking information to the layer, rough InP(111)B:Fe substrates were applied to ensure that the height of steps at the surface exceeds the height of a QL (see chapter 2). The roughness of these substrates is within a few nanometer scale and the visual appearance of the wafer surface is still shiny metallic.
To vary the roughness of the InP(111)B:Fe surface the substrates (without intended miscut) were annealed in Se atmosphere at different temperatures. Figure 4.11 shows typical RHEED patterns of a rough InP(111)B:Fe substrate obtained at different substrate temperatures, i.e. T_{sub} =300°C, 570°C, 630°C and 730°C. The annealing takes place in Se atmosphere, if the temperature is above 300°C, to prevent phosphorus out-diffusion. At 300°C the RHEED pattern displays intense spots. Increasing the annealing temperature results in additional streak features in the spotty RHEED pattern, as shown in figure 4.11. Further increase of the annealing temperature results in an increase of streak- and decrease of spot-intensities confirming the flattening of the surface, as discussed in section 3.2. At 730°C the spots completely vanish and a RHEED pattern with sharp streaks is obtained corresponding to a nominally flat InP substrate.

The Bi_2Se_3 layers on the InP(111)B:Fe substrates with different roughness were grown with a speed of approximately 1 nm per minute at a growth temperature of 300°C. The substrates were either directly heated to the growth temperature or cooled to 300°C in Se atmosphere after the annealing step.
At the growth start on rough InP(111)B:Fe streaks appear in the RHEED pattern within the growth of the first QL. The streak intensity increases while the intensity of the spots decreases. The spots vanish within the growth of six quintuple layers and a pattern with sharp streaks remains. This suggests that the rough surface of

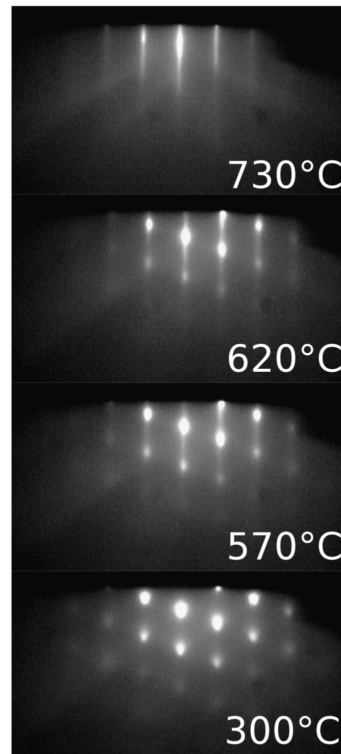

Fig. 4.11: RHEED of the InP(111)B:Fe substrate at different annealing temperatures, as indicated [TSL+14].

the InP is overgrown within six QLs implying an estimated peak to valley height of InP below 6 nm.

After the growth the layers were analyzed by XRR to determine the roughness of the InP(111)B:Fe substrates. Figure 4.12 (c) shows the XRR diffractogram of nominally 100 nm thick Bi_2Se_3 layers grown on rough and flat (annealed at 730°C) InP substrates. While the layer grown on flat substrate displays distinct oscillations in XRR, the curve for growth on rough substrates shows a small oscillation amplitude, which is a sign of a larger interface roughness. The fitting of the curves results in root-mean-square roughnesses of 0.3 nm for flat- and 2.1 nm for rough-InP substrates at the interface between substrate and layer.

Figure 4.12 (a) and (b) shows a comparison of the surface topography of 100 nm thick Bi_2Se_3 films grown on a rough and flat InP measured by AFM. The root-mean-square roughnesses are 1.1 nm and 1.7 nm for growth on rough and flat substrates, respectively. As expected from studies presented in section 4.2, the layer grown on

flat InP exhibits triangular structures with two different orientations rotated by 60° to each other. In contrast, the layer grown on rough InP(111)B:Fe exhibits only one orientation of triangular structures suggesting the formation of twin domains is suppressed in this layer. For both layers the side length of the triangles is up to 1.6 μm.

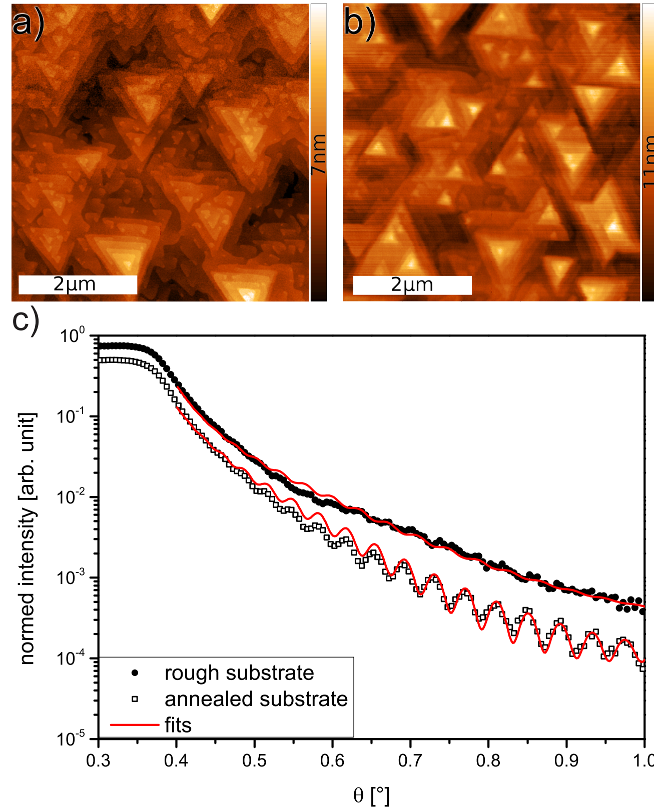

Fig. 4.12: AFM images of about 100 nm thick Bi_2Se_3 layers grown on (a) rough and (b) annealed flat InP(111)B:Fe substrates (the deformation of the triangles in the lower part of (a) is an artifact most likely caused by piezo drift of the AFM). (c) Corresponding XRR measurements of the layers grown on rough and flat InP. The red curve is the fitting curve using the surface rms roughnesses obtained by AFM to fit the interface roughness.

The triangular structure sizes for Bi_2Se_3 layers with thicknesses of nominally 0.3 μm are large enough (up to 4 μm side length) to make them visible in an optical microscope equipped with Normaski interference contrast. The optical microscope images shown in figure 4.13 allow to compare the surface of the layers grown on flat and rough InP(111) substrate on a relatively large area of approximately 120×90 μm. As determined by AFM the triangular structures are oriented

equally for growth on rough substrates forming surface with absence of any visible trenches. This is in contrast to the growth on flat substrate, where the differently oriented triangles form trenches at their boundaries.

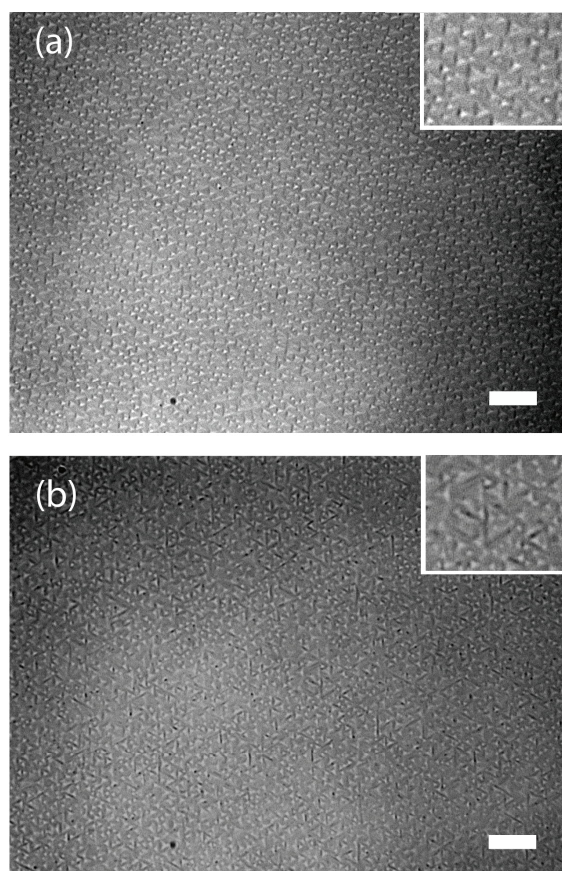

Fig. 4.13: Normaski interference contrast images of about 0.3 μm thick Bi_2Se_3 layers grown on (a) rough and (b) flat InP(111)B substrates (scale bar indicates 10μm). The large area images demonstrate that the triangular structures are homogeneously oriented over the whole layer without creating any trenches in (a) compared to the twinned layer in (b). The insets show a zoom of a factor of two for better visibility.

The structural quality of the layers grown on rough InP is studied by XRD. The wide range diffractogram of the symmetric 0 0 l reflections shown in Figure 4.14 (a) confirms that the (001) planes of Bi_2Se_3 are well oriented to the (111) planes of InP and no peaks of other phases than Bi_2Se_3 are present. Figure 4.14 (b) shows the rocking curves of the 0 0 3 Bi_2Se_3 reflections for the growth on rough and flattened

InP substrates. The FWHM for growth on the rough substrate is 0.3°, while the reflection for growth on flattened substrates exhibit two peaks with FWHM of 0.3° for the broad and 0.006° for the sharp peak. Here the sharp peak has only a small fraction of the total peak area compared to the two peak behavior observed on the bought flat InP substrates, as shown in chapter 4.2. Most likely, the flattening due to the annealing of rough InP(111)B:Fe is not sufficient to achieve the surface quality of the bought flat InP(111)B, which is required to orient the Bi_2Se_3 layer out-of-plane coherently.

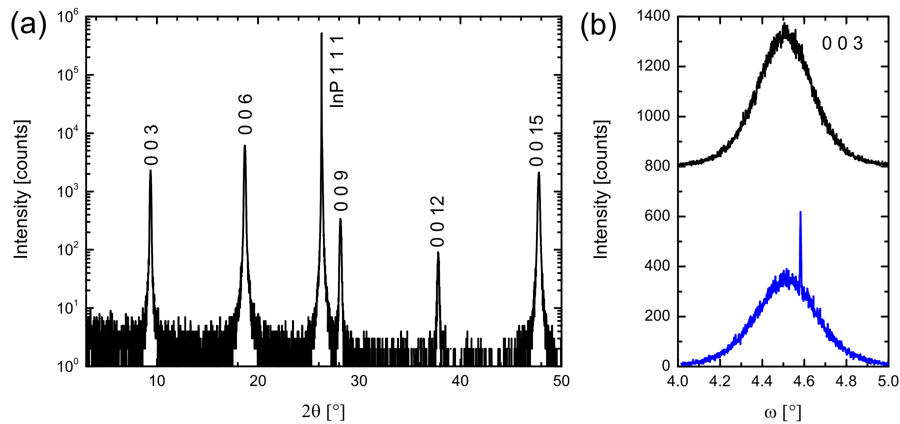

Fig. 4.14: (a) XRD diffractogram of the symmetric reflections of the {0 0 l} Bi_2Se_3 planes for growth on a rough InP(111)B:Fe substrate. (b) Rocking curves of the reflections of the {0 0 3} Bi_2Se_3 planes grown on rough (black) and annealed (blue) InP(111)B:Fe substrates (diffractograms shifted in intensity for clarity).

Pole scans of the asymmetric reflections of {0 1 5} layer planes, shown in Figure 4.15, are measured for different substrate annealing temperatures to analyze the influence of the substrate roughness on the twinning within the layer. The diffractograms display peaks with comparable intensities each 120° forming peak triplets, attesting a correct alignment of the sample. For flat surfaces (annealed at 730°C) two peak triplets are measured corresponding to two differently oriented twin domains. The volume of the twin domains within the layer is measured by the intensity area of the twin peak triplet compared to the total measured peak area and indicates a twin volume of 34%. For reducing the annealing temperatures the roughness of the substrate increases. Therefore the twin volume decreases to 6%,

2%, and below 0.1% for the substrate annealing temperatures of 620°C, 570°C, and 300°C, respectively. The twin volume of 0.1% is estimated as upper limit since the potentially present twin peaks are below the level of the noise. The pole scans confirm the complete suppression of twinning for layers grown on rough InP(111)B:Fe substrates directly grown at 300°C. This is consistent with the equal orientation of triangular islands at the surface measured by AFM and proves that the orientation of the triangular islands depends on the crystalline orientation of the Bi_2Se_3 domains. The remaining asymmetric reflections of the {0 1 5} Bi_2Se_3 planes occur under the same angle as the reflections of the {0 0 2} InP planes confirming a orientation of the QL as displayed in figure 2.5 for growth on rough InP(111)B:Fe.

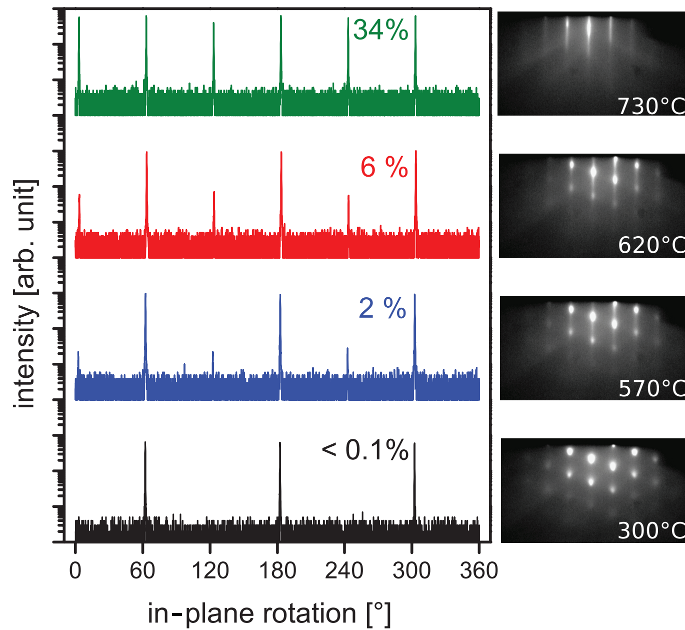

Fig. 4.15: XRD in-plane rotation diffractograms of the asymmetric reflections of the {0 1 5} Bi_2Se_3 planes for samples grown on substrates, which were annealed at different temperatures, as indicated by the RHEED images of a comparable InP substrate at the corresponding annealing temperature next to the curves. The InP {0 0 2} reflections occur under the same angle as the non suppressed {0 1 5} layer peak triplet in the present case of the InP(111)B:Fe substrates [TSL+14].

To study the microstructure of the interface between Bi_2Se_3 layer and rough InP substrate TEM analyses were performed. The large area HAADF-STEM image shown in figure 4.16 reveals the roughness of the interface between substrate and

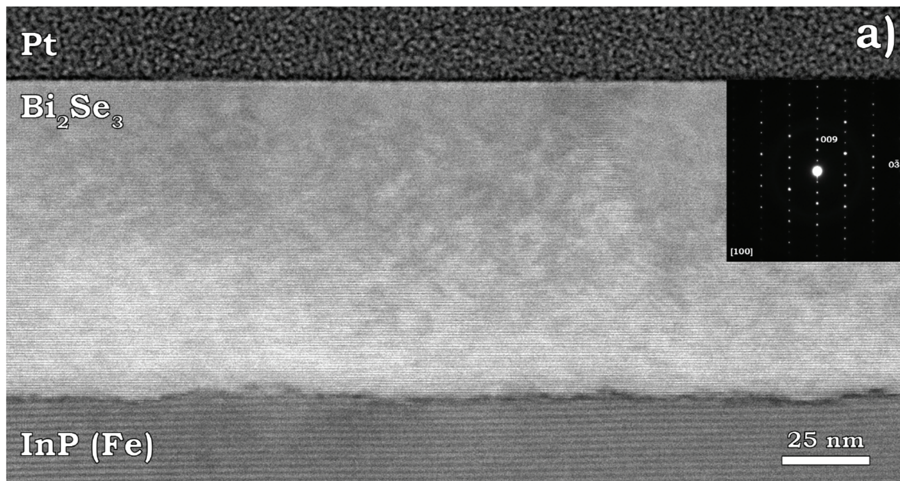

Fig. 4.16: HAADF-STEM image of a 100 nm Bi_2Se_3 layer grown on rough InP(111)B:Fe substrate. The inset shows a selected-area electron diffraction (SAED) pattern indicating the absence of twin domains [TSB+13].

layer, and a smooth Bi_2Se_3 surface. The interface is composed of hollows of few tens of nanometer in widths and depths of up to about 5 nm. The SAED pattern shown in the inset of figure 4.16 confirms the absence of twin domains [TSB+12].

The high resolution STEM shown in figure 4.17 enables to resolve the interface on atomic scale. Side walls of the hollows are formed by up to 15 InP bi-layer steps forming In-terminated (11-1)A, (1-11)A, and (-111)A facets, as sketched in figure 2.5 (c). Here sharp interfaces between the Bi_2Se_3 layer and the (111)B InP surface, as well as the side surfaces are observed, which are indicated by white lines in figure 4.17 (a).

As shown in figure 4.18 there are six possible stacking sequences, i.e. ABC or ACB stacking order starting at A, B or C position, where the A position is defined as the position of the P surface layer of InP(111)B. Figure 4.17 (b) shows a simulation of the interface of the A-A type stacking which fits well to the measured stacking sequence by TEM. This suggests, that the interface to the InP pins the lateral position of the first atomic Se layer to the A position of the P terminated (111)B InP surface, as sketched in figure 4.17 (c), forming an A-A stacking at the interface between layer and substrate.

The in-plane hexagonal lattice constant of InP matches well to that of Bi_2Se_3 while the out of plane lattices differ in their crystalline structure and lattice constant. The

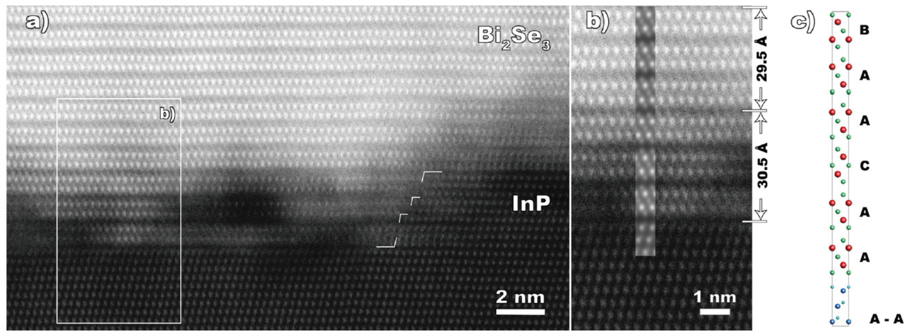

Fig. 4.17: (a) High resolution CS corrected HAADF-STEM image of the interface between Bi_2Se_3 and rough InP(111)B:Fe substrate. White lines indicate the interface of layer and substrate at the right side wall of the hollow. (b) Zoom to the region indicated by the white frame in (a), with a simulated HAADF-STEM image of three bi-layers of InP and six QLs. (c) Stick and ball model of the simulated crystal structure in (b), with the starting layer position of the QL indicated [TSL+14].

mismatch of the out of plane lattice constant of a QL to three bi-layer steps of InP is 6.5% and results in an increased vdW gap between QLs within the hollow. The c lattice constant decreases within the first six QLs from 30.5 Å for the first, to 29.5 Å for the second and to 28.7 Å for the third unit cell, as measured by TEM (see figure 4.17 (b)), almost matching the intrinsic lattice constant of bulk Bi_2Se_3 28.636 Å[Nak63].

The c lattice parameter of the first Bi_2Se_3 unit cell of 30.5 Å corresponds well to the height of nine InP bi-layer steps of 30.42 Å. Accordingly the bonds of the QL to the side walls are strong enough to increase the distance between the vdW bonded QLs over tens of nanometers in lateral direction. This implies that the bond strength to the side walls excels these of the vdW bonded QLs, suggesting that the QLs are chemically bonded to the side walls of InP within the hollows.

Besides other structural differences, the stacking position (A, B or C) of InP(111) changes within every bi-layer (ABBCCA for three bi-layers), compared to the stacking position of Bi_2Se_3 QL that changes every atomic layer (ABCAB). This difference leads to stacking faults between the weakly bonded QLs, as simulated and sketched in figure 4.17 (b) and (c), where the starting Se layer of the QLs are AACAAB (as indicated) for the first six QLs instead of the expected ACBACB. The accumula-

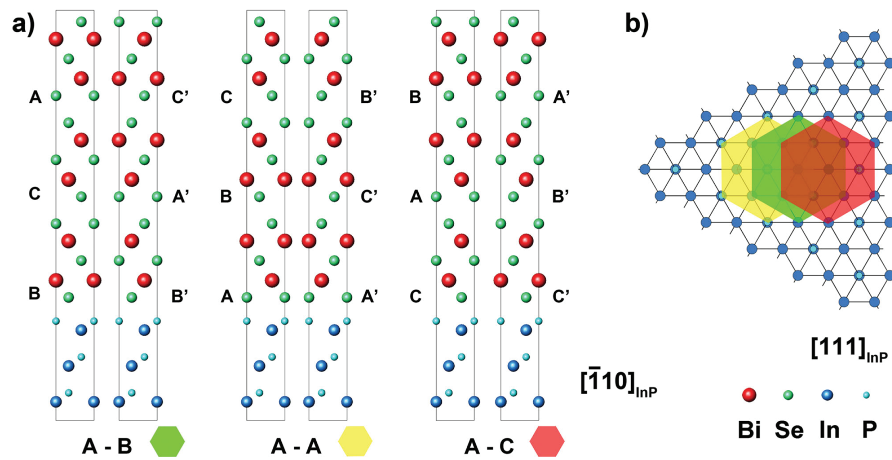

Fig. 4.18: Stick and ball models of possible stackings at the interface between Bi_2Se_3 and InP(111). (a) Cross-section of different stacking orders ABC and ACB of the interface types A-B (green), A-A (yellow) and A-C (red), where the P surface layer of InP(111)B is defined as A position and the second letter represents the first atomic layer (Se) of the QL. (b) Top view on the positions of the first Se layer of the QL (indicated by the edges of the colored hexagons) of different stackings shown in (a) [TSL+14].

tion of QLs starting with A position coincidences with the stacking order of three bi-layers of InP(111)B within the hollow, which always starts at A position. This accumulation is presumably favored by the increased vdW gap between QLs due to the out-of-plane height mismatch between a QL and three bi-layers.

The difference in crystal structure results in a defect observed by TEM, caused by domains growing in hollows with different depths. Therefore domains grown in different hollows are likely to be translated in z-direction to each other, and most likely also in xy-direction due to the change of ABC position of the P surface layer

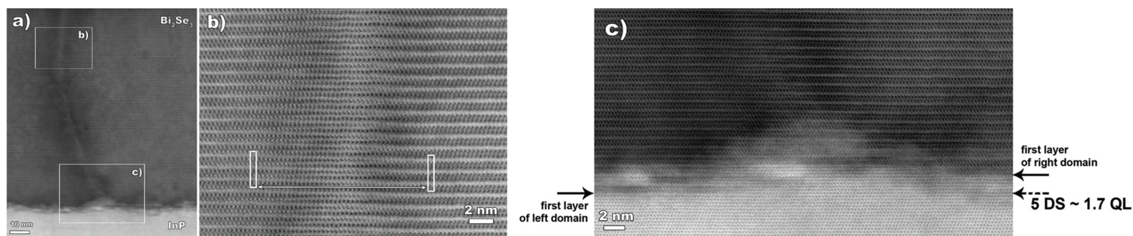

Fig. 4.19: Crossectional STEM image of the transition domain boundary between Bi_2Se_3 domains grown in different InP(111)B hollows. (a) Overview BF-STEM image,(b) HAADF-STEM image of the region labeled in (a) with white unit cells indicating the translation in z-direction of the two domains. (c) Zoom to the interface region of the boundary showing the difference of depth in the hollows [TSL+14].

occurring for each bi-layer step. Figure 4.19 shows such a translation domain boundary, which forms a zipper-like domain boundary, where the two Bi layers in each QL are split to form an interface to QLs shifted in z-direction [LLG+13, TSL+14]. These domains share the same crystalline orientation with an offset in z-direction due to different depths of the hollows. The difference of height level of the unit cell is about one third of a QL in z-direction, as visualized in figure 4.19 (b). This difference corresponds approximately to the height of a bi-layer step of InP.

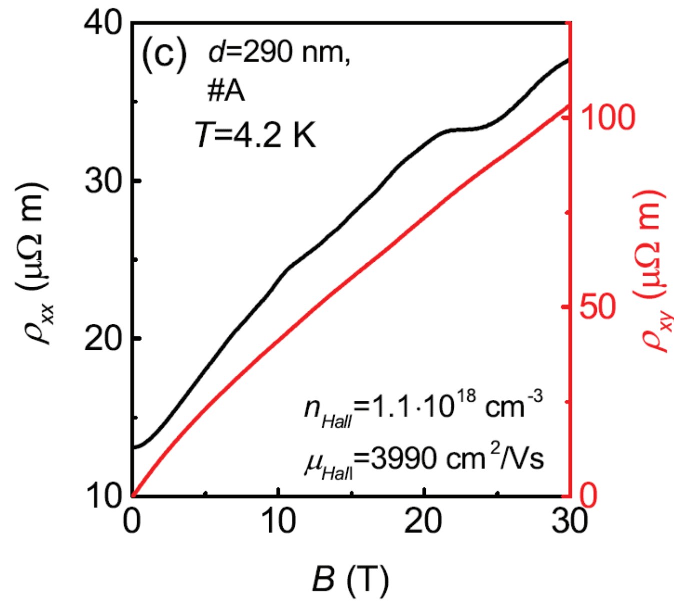

Fig. 4.20: High magnetic field magnetotransport of a 290 nm thick twin free Bi_2Se_3 layer grown on rough InP(111)B:Fe [WJF+16].

Magnetotransport measurements reveal that the twinning defect in Bi_2Se_3 layers grown on InP increases the carrier density up to an order of magnitude. The lowest carrier density measured in twin free Bi_2Se_3 layers is 9×10^{17}cm^{-3} with a mobility of 2000 $\frac{cm^2}{Vs}$ for a 100 nm thick film, while twinned Bi_2Se_3 grown on bought flat InP(111)B shows carrier densities of 9×10^{18}cm^{-3}.

The carrier density of non twinned films stays nearly constant at 1.1×10^{18}cm^{-3} for increasing the layer thickness while the mobility further increases, up to a value of 3990 $\frac{cm^2}{Vs}$ for a 290 nm thick film, as shown in figure 4.20. On the other hand thin films with thicknesses below 50 nm, i.e. 20 nm, 11 nm, and 8 nm, show an increased

carrier density up to the order of 10^{19}cm^{-3}, presumably caused by defects at the rough interface to the substrate, as described above [WJF+16].
Remarkably, the twin free films show Shubnikov-de-Haas oscillations in the magnetotransport measurements (see figure 4.20). The oscillations show a complex behavior, which can not be understood by a simple one carrier model. Here the contributions of top-, bottom- and side surfaces, as well as the bulk states to the conductivity of the TI layer have to be included.

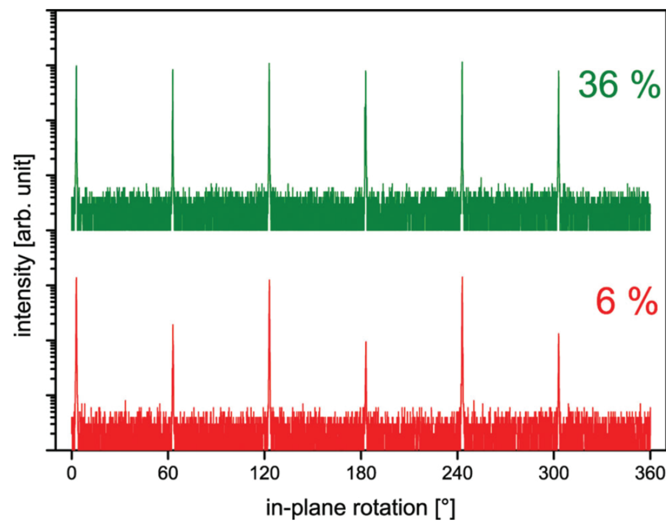

Fig. 4.21: XRD in-plane rotation diffractogram of the reflections of the {0 1 5} Bi_2Se_3 planes for 100 nm thick Bi_2Se_3 layers grown on rough (red) and flat (green) InP(111)A substrates (curves shifted for clarity). The measured twin volume is indicated next to the curves [TSL+14].

In order to clarify the influence of the surface termination of the substrate on the Bi_2Se_3 twin suppression, the growth on InP(111)A:Fe substrates was performed at the same growth conditions like on InP(111)B:Fe substrates. Here, the RHEED, AFM, XRR, and XRD measurements showed comparable results of the influence of the surface roughness on the twin domain suppression. The XRD pole scan illustrated in figure 4.21 shows a suppression of twin domains to a volume of 6% for increased surface roughness. The suppressed peak triplet of the {0 1 5} Bi_2Se_3 planes for growth on InP(111)A:Fe is at the same in-plane angle as the reflections of the InP {0 0 2} reflections, in contrast to the layers grown on rough InP(111)B:Fe. This indicates, that the surface termination within the substrate hollows controls

the selection of the Bi_2Se_3 twin domain being suppressed. However, further studies are needed to clarify the selection of twin domains in dependence of the substrate surface termination.

In conclusion, the twinning of the Bi_2Se_3 layers grown on InP can be suppressed if steps on the surface exceed the height of a QL, as demonstrated by the uniformly oriented trigonal surface structures in AFM and Normaski microscopy, the threefold symmetry of the {0 1 5} asymmetric XRD reflections, and the absence of differently oriented domains in TEM analysis for growth on rough InP(111)B:Fe. This twin suppression is realized by the strong chemical bonds of the QLs to the side facets within a hollow, which transfer the stacking information to the layer and enlarge the c lattice constant. It is shown, that the twinning defect increases the carrier density by an order of magnitude, which reveals it as a main source of doping in the Bi_2Se_3 layers grown on InP(111). Suppression of the twins in Bi_2Se_3 is a mayor step to further reduce the carrier density in this material. The achieved low carrier densities in these twin free layers are promising for the application of gating and doping techniques to shift the Fermi level into the bulk band gap.

5 Growth and characterization of $Bi_{2-x}Sb_xTe_{3-y}Se_y$ (BSTS) films

5.1 Bi_2Te_3

This chapter describes the influence of the Element V to VI flux ratio on the structural and electronic properties of MBE grown Bi_2Te_3. Bi_2Te_3 is known from literature to be n- or p-type conducting, in dependence of the fabrication method and the defects in the crystal [HCK86, FGT+88]. Ingots fabricated by the Bridgman method tend to be n-type for annealing in Te-rich and p-type for Bi-rich melts, which vary by a few atomic percent of the stoichiometric composition [FGT+88]. The carrier type is determined by crystal defects, i.e. bismuth antisite (Bi_{Te}) causing p-type doping and tellurium (Te_{Bi}) antisite defects causing n-type doping.

The Bi_2Te_3 MBE grown layers are n-type under Te-rich growth conditions. Therefore, the growth of Bi-rich layers is studied to reduce the doping level of the Bi_2Te_3 layers.

The layers were grown on hydrogen passivated Si(111), prepared as described in chapter 4.1. A series of samples with different Bi cell temperatures in the range of T_{Bi}=600°C to 720°C were grown while keeping the substrate temperature and tellurium cell temperature constant at T_{sub}=300°C and T_{Te}=380°C. The BEP ratio of Te ($p_{Te}=2.9\times10^{-6}$mbar) to Bi ($p_{Bi}= 5.5\times10^{-8}$mbar to 72×10^{-8}mbar) varies from 6 to 75. The growth time was adjusted to obtain layer thicknesses of approximately 80 nm.

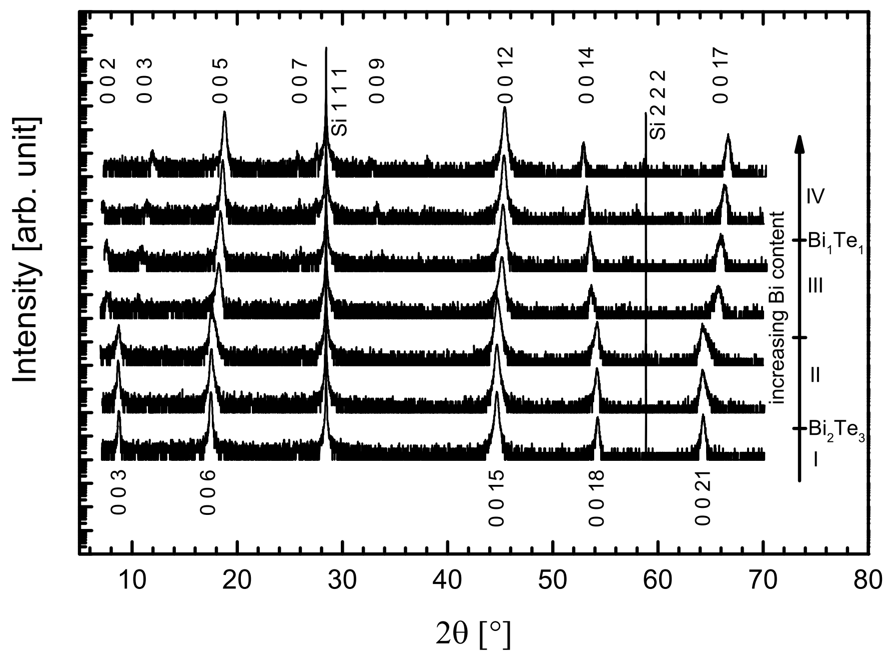

Fig. 5.1: XRD difractograms of representative bismuthtellurides of the growth series with varied Bi flux. The Bi content increases from the bottom to the top. The Bi_2Te_3 and Bi_1Te_1 like reflections are labeled below and above the diffractograms, respectively. The arrow indicates the different regions corresponding to the diffractograms next to it: Te-rich (I) and Bi-rich (II) Bi_2Te_3, as well as the Te-rich (III) and Bi-rich (IV) Bi_1Te_1. Curves are shifted by two decades for clarity.

Figure 5.1 shows the wide range θ-2θ-diffractograms of representative samples of this growth series. The bottom curve represents the Bi_2Te_3 diffractogram with the $(0\ 0\ l)$ (l=3n; $n \in \mathbb{Z}$) peaks labeled. For increasing the Bi flux the 0 0 6 peak forms a shoulder at higher angles and also the peak position drifts in this direction. Further increasing the Bi Flux leads to appearance of new peaks, e.g. close to the former position of the 0 0 3 peak there are two peaks with relatively low intensity. The new set of peaks fits well to the expected positions and intensities of the 0 0 2, 0 0 3, 0 0 5, 0 0 7, 0 0 9, 0 0 12, 0 0 14, and 0 0 17 Bi_1Te_1 reflections. The BEP ratio for obtaining Bi_2Te_3 without shoulders is $\frac{p_{Te}}{p_{Bi}} > 20$, the transition to Bi_1Te_1 like reflections occurs at $\frac{p_{Te}}{p_{Bi}} = 16$, and the composition Bi_1Te_1 is achieved at $\frac{p_{Te}}{p_{Bi}} = 10$.

These BEP ratios separate the growth series in four regions: I. Te-rich Bi_2Te_3 for $\frac{p_{Te}}{p_{Bi}} > 20$, II. Bi-rich Bi_2Te_3 for $20 > \frac{p_{Te}}{p_{Bi}} > 16$, III. Te-rich Bi_1Te_1 for $16 > \frac{p_{Te}}{p_{Bi}} > 10$, and IV. Bi-rich Bi_1Te_1 for $\frac{p_{Te}}{p_{Bi}} < 10$.

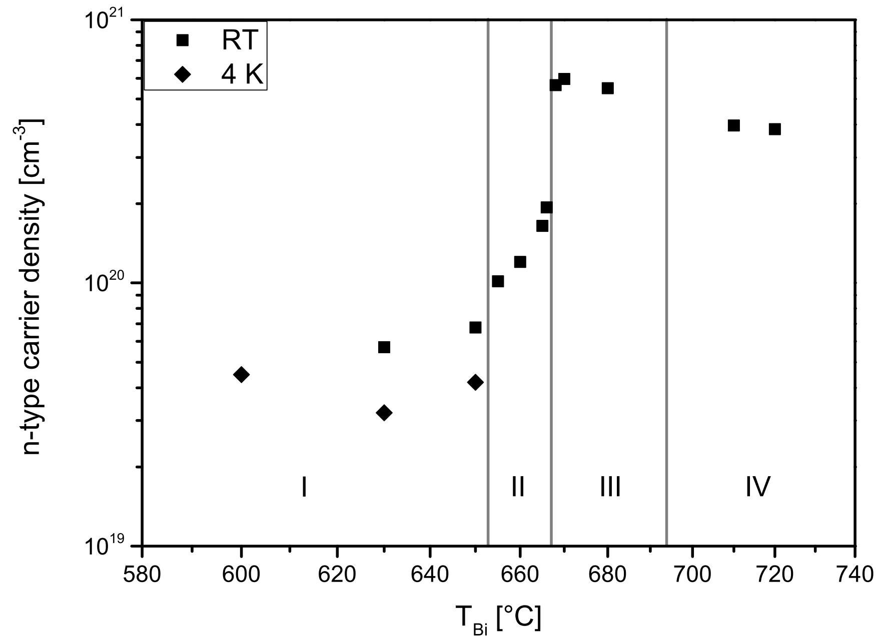

Fig. 5.2: Carrier density in dependence of the Bi cell temperature measured at room temperature and 4 K as labeled in the graph. The gray vertical lines separate the Te-rich (I) and Bi-rich (II) Bi_2Te_3, as well as the Te-rich (III) and Bi-rich (IV) Bi_1Te_1 regions.

The samples were measured by magneto transport as shown in figure 5.2, where the carrier density is plotted versus the Bi cell temperature. The Bi cell temperature is chosen in the figure as the most accurate measure of relative Bi flux, since the differences in the measured BEPs are smaller than the measurement accuracy. The samples are measured at room temperature as well as 4 K, where the determined carrier densities are slightly lower at 4 K for samples measured at both temperatures. In region I (with the excess supply of Te) the carrier density of Bi_2Te_3 is in the range of 3 to $7{\times}10^{19}$ cm^{-3}. Increasing the Bi flux to obtain Bi rich growth conditions results in a gradual increase of the carrier density up to $2{\times}10^{20}$ cm^{-3} as shown in region II. Further increase of Bi flux results in the transition from Bi-rich Bi_2Te_3 (region II) to Te-rich Bi_1Te_1 (region III) as determined by XRD. This crystalline transition results in an abrupt increase of the carrier density from $2{\times}10^{20}$ cm^{-3} to $6{\times}10^{20}$ cm^{-3} within a change of Bi cell temperature of 2°C. At higher Bi fluxes the carrier density decreases to a doping level of $4{\times}10^{20}$ cm^{-3} for

Bi-rich Bi_1Te_1 in region IV.

In conclusion, the variation of Bi flux results in well crystalline bismuth tellurides with a transition from a pure Bi_2Te_3 QL structure to a Bi_1Te_1 like structure with Bi double-layers between QLs at a flux ratio $\frac{p_{Te}}{p_{Bi}}<16$. The samples grown under Bi-rich conditions with slight deviations from the stoichiometric Bi_2Te_3, as determined by the peak shift as well as the formation of a shoulder at the Bragg peaks measured by XRD, show a gradual increase of the n-type carrier density with increasing the Bi flux. This suggests, that the excess of Bi rather forms n-type doping Bi interstitials between QLs than positively charged Bi_{Te} antisites during the growth.

5.2 $Bi_2Te_{3-y}Se_y$

Parts of this chapter are already published [SBK+16].

$Bi_2Te_{3-y}Se_y$ alloys are topological insulators with the same crystal symmetry as their binary compounds ($y = 0$ and $y = 3$). The ordered alloy with Se content $y = 1$ combines beneficial features of both binary compounds: the relatively large band gap (≈0.3 eV) with the Dirac point of the TI surface state at an energy within the band gap of Bi_2Se_3 and the Bi_2Te_3 property of being relatively insensitive to vacancy defects [TT61, RTS+10, MSS+14]. Therefore the ternary compound Bi_2Te_2Se with the out of plane stacking Te-Bi-Se-Bi-Te (VI(1)-Bi-VI(2)-Bi-VI(1)) within the QLs, where the Se layer is covalently bonded to six neighboring Bi atoms, is a promising candidate for obtaining a bulk insulating TI due to the reduction of the Se vacancy defects, which act as a double electron donor in Bi_2Se_3 [HRR+09].

To study the chemical order within our MBE grown $Bi_2Te_{3-y}Se_y$ alloys, a growth series on H-passivated Si substrates is performed. The layers are grown at a growth rate of about 1 QL min^{-1}, as determined by profilometer measurements of the layer thickness of approximately 70 nm and the growth time of 70 min. given that the growth rate is only limited by the Bi flux under this group-VI rich growth conditions, the flux of Bi is determined by the growth rate and the number of Bi planes in the QL, i.e. two monolayers (ML). In this study, the fluxes of Bi and Te are kept constant at $f_{Bi} = 2$ ML min^{-1} and $f_{Te} = 84$ ML min^{-1}, as well as the growth temperature of $T_{sub} = 300°$C. To obtain the full composition range the flux of Se f_{Se} is varied from 0 to 250 ML min^{-1}. Additionally, a layer without Te flux is grown to obtain binary Bi_2Se_3. The Se content y in the layers is determined by EDX, with an accuracy of about ±0.05.

In the following paragraphs, the data collected by EDX, XRD, and RAMAN measurements is compared with calculated values expected from an alloy with perfect order (first Se is filled in VI(2) sites, then in VI(1) sites), random order (Se is filled in all VI(1/2) sites randomly) and an order calculated from a kinetic growth model

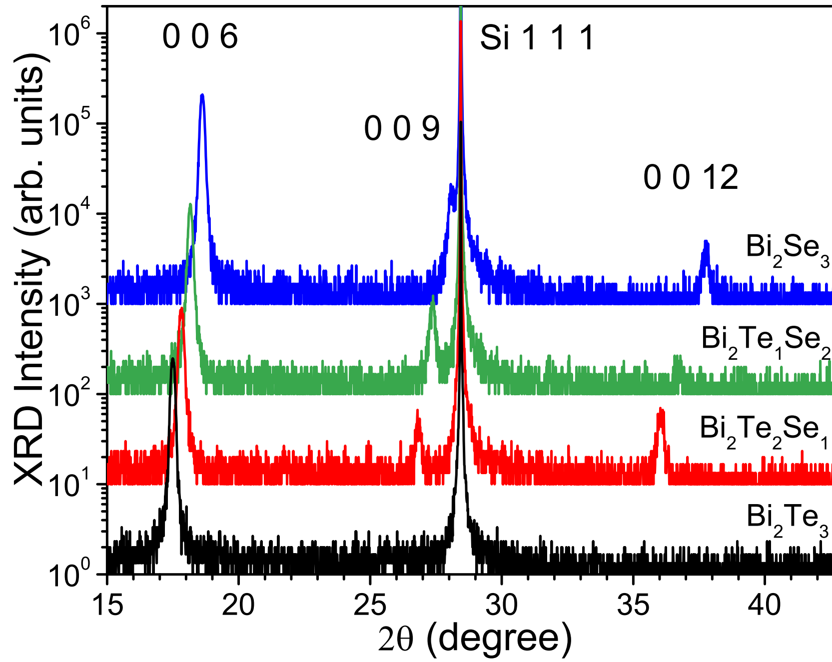

Fig. 5.3: XRD θ-2θ diffractogram of $Bi_2Te_{3-y}Se_y$ alloys with $y = 0, 1, 2, 3$ as indiccatd (curves shifted for clarity) [SBK+16].

(Se and Te is filled in the VI(1/2) sites according to their surface coverage and site selectivity) to study the chemical order within the $Bi_2Te_{3-y}Se_y$ QL [SBK+16].

The XRD θ-2θ diffractogram displayed in figure 5.3 shows the region of the 0 0 6, 0 0 9, and 0 0 12 reflections of the Se contents $y = 0, 1, 2, 3$. The intensities of the 0 0 9 and 0 0 12 reflections alternate depending on the Se content and are below the measurement noise level for $y = 0$ (Bi_2Te_3). The reflections gradually shift with increasing Se content y to higher angles due to the decreasing lattice parameter c. Figure 5.4 shows the lattice parameter c in dependence of the Se content y. The lattice parameter c deviates from linearity (Vegard's law), which is expected due to the difference in coordination number of the group-VI lattice sites and electronegativity of the chalcogens. Rather, a bowing is observed for $y > 1$ indicating a non linear change of the separation between layer planes. This non linear change of layer separations is primarily assigned to the VI(1)-VI(1) separation c_{vdW} between the QLs as a function of Se content y_1 on these sites. The van der Waals bonds of mixed atomic pairs are weaker than those of Te-Te or Se-Se pairs. Thus the deviation of

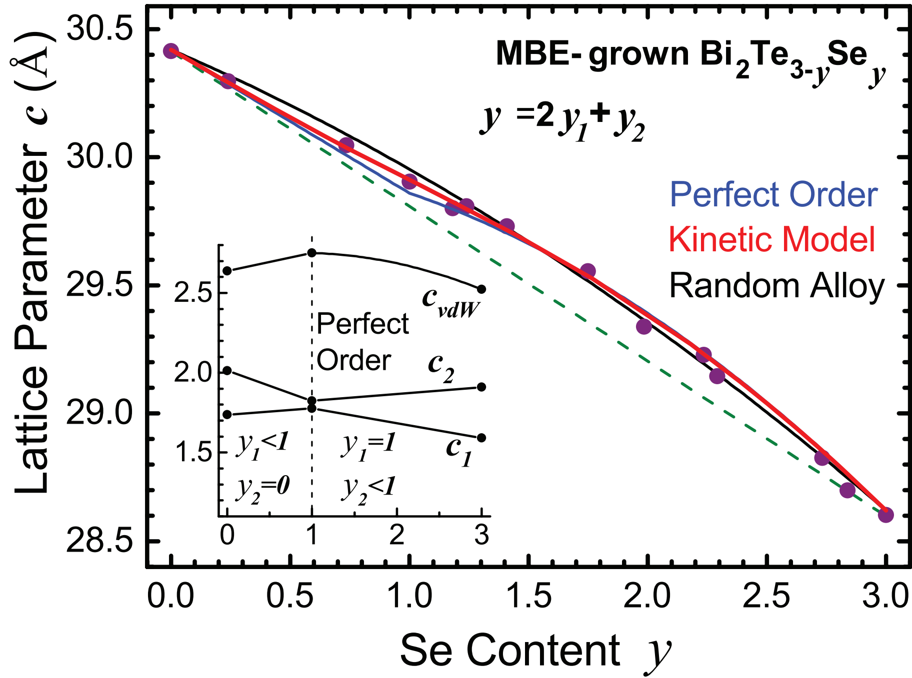

Fig. 5.4: Lattice constant c determined from positions of 0 0 l XRD reflections of $Bi_2Te_{3-y}Se_y$ alloys (dots), the linear behavior after Vegards's law (green dashed line), as well as $c(y_1, y_2)$for random alloy, perfect order and the $y_{1,2}$ values obtained by the kinetic growth model plotted versus the Se content y. The inset shows the sublayer separations for the perfect ordered $Bi_2Te_{3-y}Se_y$ alloys versus Selenium content y in Å[SBK+16].

Vegard's law is incorporated by the term $y_1(1-y_1)$ describing the probability of Se-Te pairs contributing to the van der Waals bonds [MLS63, WM60, SBK+16].

The lattice parameter c depending on the Se content on the sites y_1 and y_2 can be interpolated between the known literature values of the ordered chalcogenides with $y = 0$, 1, and 3, using:

$c(y_1, y_2) = 30.42$ Å$-y_2 0.56$ Å$-y_1 0.24$ Å$+y_1(1-y_1)0.6$ Å, where y_1 and y_2 describes the Se content on the VI(1) and VI(2) lattice sites with $y = 2y_1 + y_2$ [SBK+16].

Besides the data, also calculated $c(y_1, y_2)$ curves are plotted corresponding to layer separations of a random alloy, perfect ordered alloy and the order obtained by the kinetic model in figure 5.4. The three curves show a bowing fitting to the data points within the accuracy of the experiment. The partial overlap of the curves indicates that the lattice parameter c is rather insensitive to the degree of chemical order within the QL and thus not reliable to discriminate between them.

The layer separations c_1, c_2, and c_{vdW}, between VI(1)-Bi, Bi-VI(2), and VI(1)-VI(1), respectively, depend on the lattice constant c described by the formula $c = 3(2c_1 + 2c_2 + c_{vdW})$ and the Wyckoff positions of the atoms given in literature for Bi_2Te_3, Bi_2Te_3 and ordered $Bi_2Te_2Se_1$ [SBK+16]. These layer separations are plotted in the inset of figure 5.4 (assuming alloys are perfectly ordered) revealing that all layer separations depend on the Se content and show a non-monotonic behavior.
The incorporation of the Se on the VI(2) position decreases the layer separation c_2 due to its lower atomic radius compared to Te and higher electronegativity of Se (2.4) than Te (2.1). The increased ionic character of the Bi-VI(2) bond transfers the electron charge into this bond from the VI(1)-Bi bond reducing its polarity. This results in an increasing separation c_1 and c_{vdW} with increasing y_2. On the other hand, the incorporation of Se in the VI(1) sites causes a decrease of c_1 and c_{vdW} (with bowing), as well as an increase of c_2.

A method to study chemical order within alloys by XRD is the analysis of reflection intensities depending on the position and atomic form factors of the elements within the crystal structure. Therefore the data in figure 5.5 show the integrated intensity of the 0 0 12 reflections as a function of Se content y. To reduce the experimental inaccuracies these intensities were normalized to the 0 0 6 reflection intensities, which are nearly independent of Se content. The data points of the intensity ratio $I_{0\ 0\ 12}/I_{0\ 0\ 6}$ show an oscillatory behavior exhibiting minima in intensity ratio at $y = 0$ and $y = 2.5$ (due to the vanishing 0 0 12 reflection intensities), as well as maxima at $y = 1$ and $y = 3$. To determine the order within the QL the ratio of the quadratic structure factors $|S_{0\ 0\ 12}/S_{0\ 0\ 6}|^2$ of a random alloy, a perfect ordered alloy and an alloy with the order resulting from the kinetic growth model are compared with the experimental data [SBK+16].
The structure factors were calculated using the layer separations depicted in the inset of figure 5.4. The intensity ratio $S_{0\ 0\ 12}/S_{0\ 0\ 6}$ taken from the binary compound Bi_2Se_3 with certain chemical order is used to scale the data accordingly to

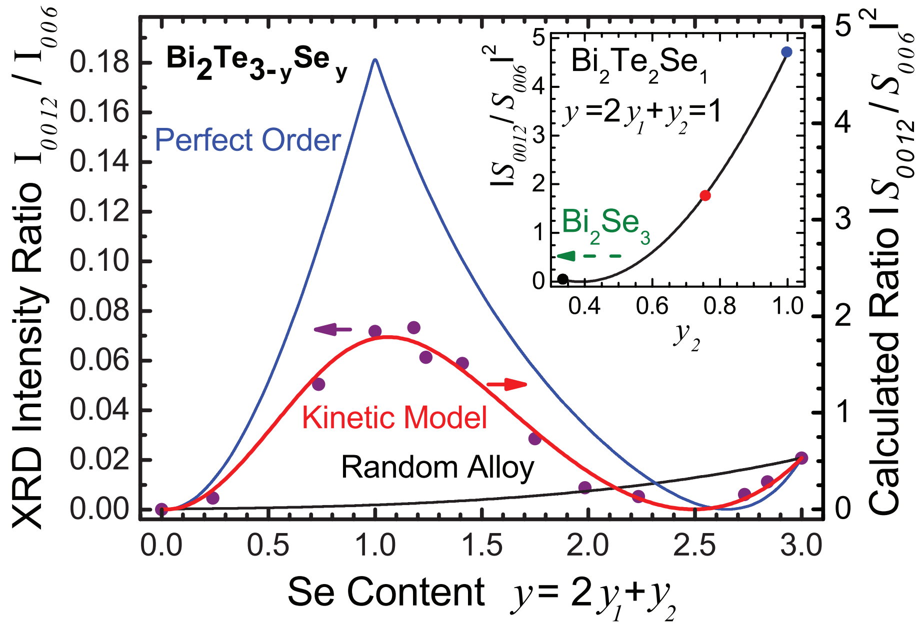

Fig. 5.5: Lattice constant c determined from positions of 0 0 l XRD reflections of $Bi_2Te_{3-y}Se_y$ alloys (dots), the linear behavior after Vegards's law (green dashed line), as well as $c(y_1, y_2)$for random alloy, perfect order and the $y_{1,2}$ values obtained by the kinetic growth model plotted versus the Se content y. The inset shows the sublayer separations for the perfect ordered $Bi_2Te_{3-y}Se_y$ alloys versus Selenium content y [SBK+16].

the experimental correction factors. The randomly ordered alloys show a successive increase in intensity without oscillating behavior proving that Se is not incorporated randomly. The perfect ordered structure shows an oscillatory behavior with the position of maxima fitting to the data, but a higher intensity ratio and a sharper peak at $y \approx 1$ ruling out that the layers are perfectly ordered. The chemically ordering obtained by the kinetic model fits well to the observed data at the whole Se content range implying that the chemical order within the layers is well described by this kinetic growth model. It considers adsorption of the impinging Te and Se fluxes, their incorporation and desorption, as well as the site selectivity of Se compared to Te [SBK+16].

The inset of figure 5.5 shows the ratio of squared structure factors $|S_{0\ 0\ 12}/S_{0\ 0\ 6}|^2$ for the range from random to perfect order of y_2 calculated for $Bi_2Te_2Se_1$ $(y = 1)$ allowing to determine the chemical order by measuring the XRD intensities of the 0 0 6 and 0 0 12 reflections. The intensity ratio is small for random alloy and increases monotonically for $y_2 > 0.5$. The slope increases with the Se content y_2.

The dots mark the ordering within the $Bi_2Te_2Se_1$ where the black dot ($y_2 = 0.33$) represents the random order, the red dot the order depicted from the kinetic growth model ($y_2 = 0.75$), and blue dot the perfect order ($y_2 = 1$). Permitting an uncertainty of $\pm 1\%$ in the layer separations c_1 and c_2 given by the literature values results in an shift of the determined degree of order up to ± 0.05.
Focusing on the experimental uncertainty of determining the peak intensities, an error bar of $\pm 20\%$ on the measured peak ratio still yields a result of $y_2 = 0.75 \pm 0.04$ due to the large slope of the curve shown in the inset of figure 5.5 [SBK+16]. Where an error bar of 20% in peak intensity ratio for applying the XRD correction factors that vary slightly with Se content and for statistical fluctuations of the weak 0 0 12 peak is an extremely conservative estimate [SBK+16].
This suggests, that the chemical order y_2 in MBE grown $Bi_2Te_{3-y}Se_y$ layers is well described by the kinetic model and experimentally quantified by analyzing the XRD peak intensities for $y = 1$ [SBK+16].
The intensity oscillations of the 0 0 12 peak is presumably caused by partially occurring destructive interference with increasing the Se content due to the non-monotonic variations of sublayer separations [SBK+16].

The structural analysis reveals, that the layers grown on H-Si(111) show crystal defects as observed for Bi_2Se_3 on this substrate, such as twinning, high mosaicity-tilt and -twist. Therefore, the carrier densities remain high in the range of 1 to 3 times 10^{19}cm^{-3}, which probably conceals the effect of reducing Se vacancies in $Bi_2Te_{3-y}Se_y$ alloys.

In summary, the chemical order of the $Bi_2Te_{3-y}Se_y$ layers shows preferential incorporation of Se in the VI(2) site. Especially, XRD intensity analysis allows to quantify the chemical order. The determined Se content on the middle layer of the QL of the $Bi_2Te_2Se_1$ alloy is $y_2 = 0.75 \pm 0.04$. The XRD intensities agree well with a kinetic growth model suggesting that the chemical order of MBE grown layer is kinetically limited [SBK+16]. In addition the chemical order is independently confirmed by Raman phonon spectroscopy of $Bi_2Te_{3-y}Se_y$ layers in the whole com-

position range from $y = 0$ to 3 [SBK+16]. A promising route towards low carrier densities is to combine reduction of Se vacancies in chemically ordered $Bi_2Te_{3-y}Se_y$ layers with increasing the crystalline quality by use of lattice matched substrates, as well as suppressing twin domains, as described in chapters 4.2 and 4.3.

5.3 $Bi_{2-x}Sb_xSe_3$

The topological insulators Bi_2Se_3, Bi_2Te_3, and Sb_2Te_3 have large bulk band gaps, in comparison to other TIs, which allow for possible room temperature applications. These materials have relatively high carrier densities, caused by crystal defects, such as vacancies and anti-sites. Bi_2Se_3 and Bi_2Te_3 show n-type and Sb_2Te_3 p-type bulk conduction, while Sb_2Se_3 is a trivial band insulator. In this approach, Bi_2Se_3 is alloyed with Sb to achieve reduction of the bulk carrier density by changing the defect chemistry in the crystal, e.g. reducing Se vacancies and forming Sb_{Se} anti-sites, as described in chapter 2. The growth parameters of twin free Bi_2Se_3 layers grown on rough InP(111)B:Fe with carrier densities of approximately $10^{18}cm^{-3}$, as described in section 4.3, were used to alloy Bi_2Se_3 with Sb to obtain as high crystalline quality and low carrier density as possible. The layers and growth conditions were analyzed by EDX, as described in chapter 3.5, and BEP measurements to obtain the composition of the layers. AFM, XRD, and ARPES were carried out to determine the crystal structure and the presence of surface states in the $Bi_{2-x}Sb_xSe_3$ alloy. Magneto-transport measurements were applied to study the influence of Sb alloying on the electrical properties of the layers.

The $Bi_{2-x}Sb_xSe_3$ layers are grown on rough semi insulating InP(111)B substrates, which were used for the twin suppression described in section 4.3 and hydrogen passivated Si(111). The Sb cell temperature was varied to obtain different Sb pressure p_{Sb} for each growth (figure 5.7), whereas the other temperatures were kept constant at $T_{Bi} = 650°C$, $T_{Se} = 180°C$, and $T_{sub} = 300°C$, resulting in group-VI rich growth conditions ($p_{Bi} = 1.5\times10^{-7}$ mbar, $p_{Se} = 3.8\times10^{-6}$ mbar). The growth was initiated by opening the Bi, Sb, and Se shutters simultaneously and the growth time was kept constant. To obtain a Sb_2Se_3 layer ($x = 2$) the growth procedure were performed without Bi flux. Figure 5.6 shows representative RHEED patterns of samples with different Sb contents after growth. The layers with a Sb concentration x ranging from 0 to 1.2 show streaky RHEED patterns (figure 5.6 (a) and (b)), indicating a 2D crystalline layer growth. The RHEED pattern (figure 5.6 (c)) for a sample

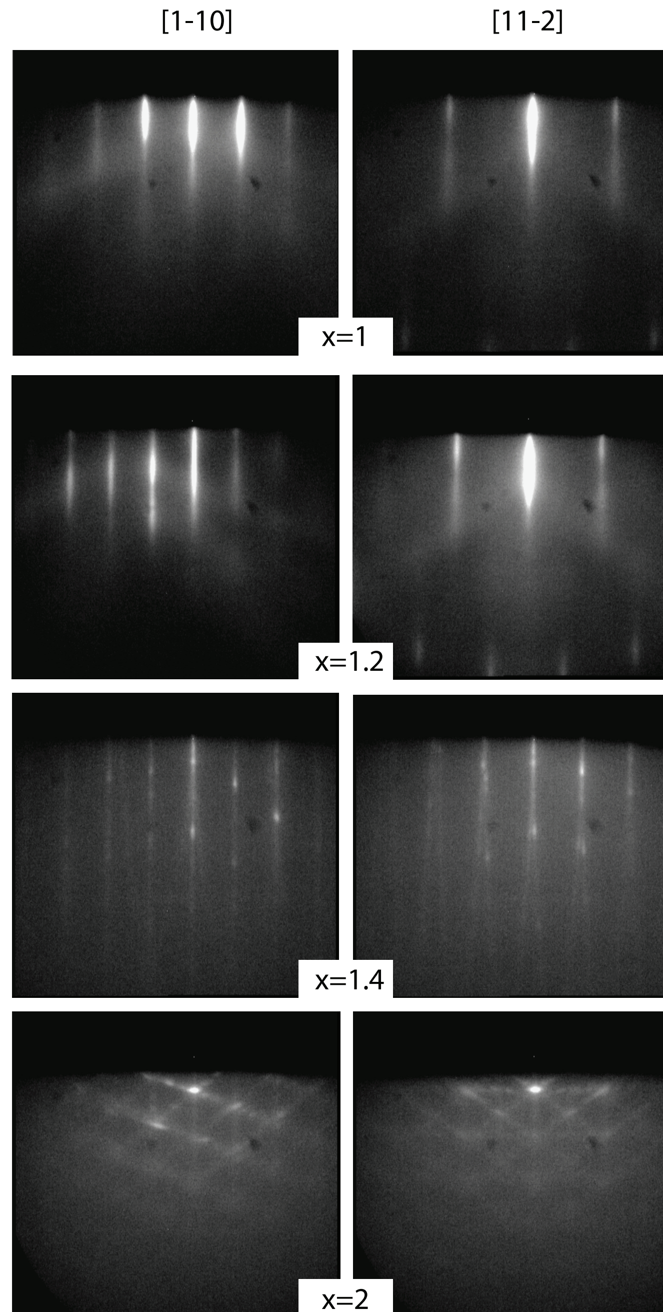

Fig. 5.6: RHEED patterns of $Bi_{2-x}Sb_xSe_3$ layers after growth with increasing Sb content x from top to bottom, as indicated in the image, taken in the [1-10] and [11-2] direction of InP(111).

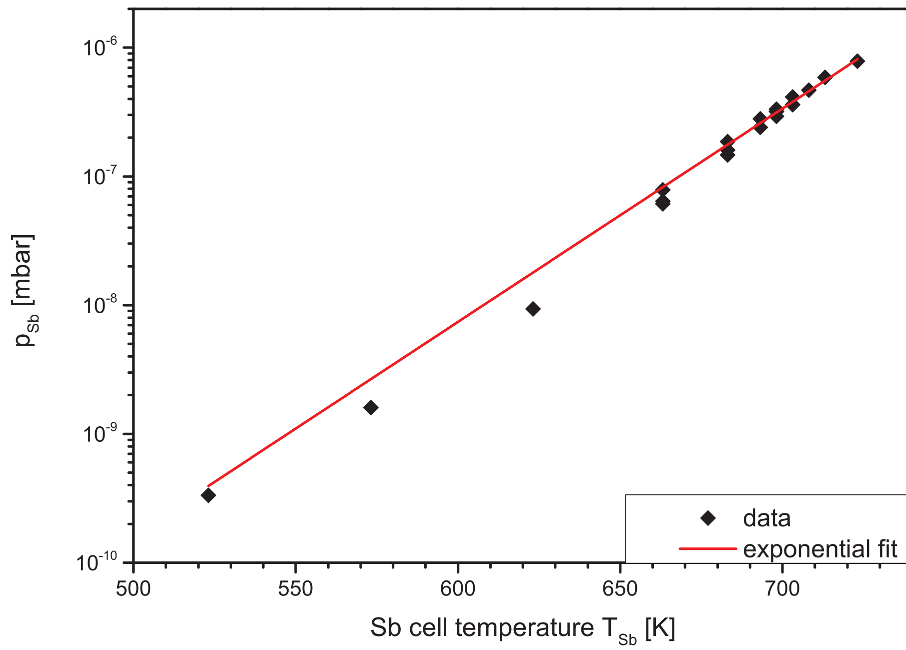

Fig. 5.7: Measured Sb pressure values p_{Sb} at various cell temperatures T_{Sb} fitted exponentially (red).

with $x = 1.4$ shows spots and streaks with an inclination to the surface normal. These features indicate the presence of tilted grains and an increased roughness of the surface compared to layers with lower Sb contend. The RHEED image of the layer with $x = 2$ shows a complex pattern including spots, and horizontal, vertical, and inclined streaks indicating a rough surface with steps and facets.

The layers alloyed with Sb were analyzed by EDX to determine their composition. Here, hydrogen passivated Si(111) wafers were used as substrates to exclude the overlap of the In L- and Sb L-lines in the EDX spectrum for growth on InP(111), as shown in figure 3.5 (b). The measured compositions of the layers result in a group-V to -VI ratio of $\frac{2}{3}$ as expected for a V_2VI_3 layer, revealing a preferential incorporation of Sb on group-V sites. Figure 5.8 shows the relation between the ratio of Sb flux F_{Sb} to the total group-V flux $F_{Sb} + F_{Bi}$ and the Sb content x of the layers measured with EDX at constant Bi- and Se- fluxes. These measurements allow a calibration of the Sb content x in dependence of the applied fluxes of group-V elements with a flux rate equation: $x = 2 \cdot \frac{k_{Sb}/k_{Bi} F_{Sb}}{k_{Sb}/k_{Bi} F_{Sb} + F_{Bi}}$, where k is the sticking coefficient and F represents the flux of the indexed elements, as discussed in chapter 3.1. The stick-

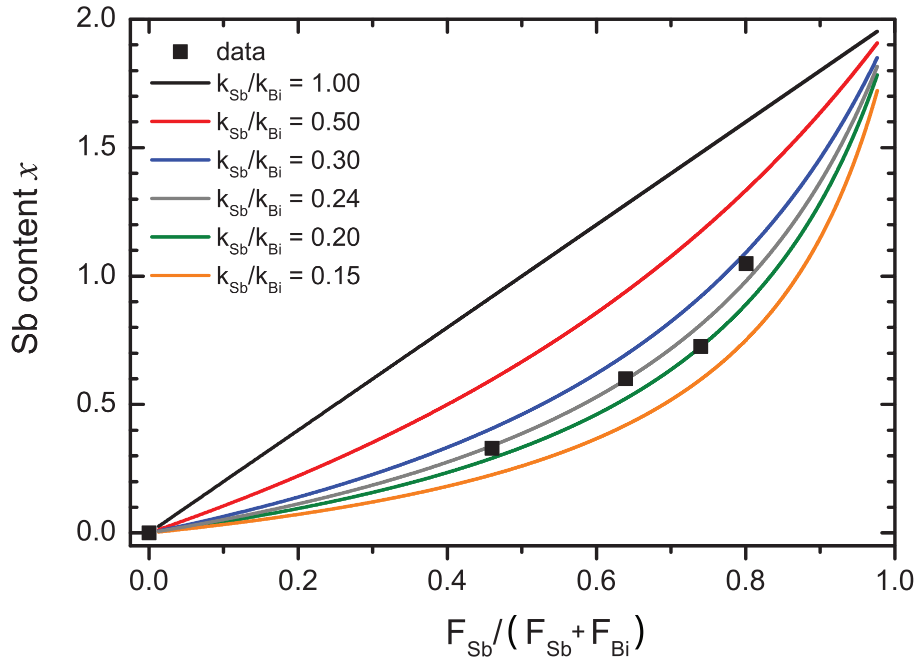

Fig. 5.8: Sb content x versus the ratio of the Sb flux F_{Sb} to the total group-V flux $F_{Sb}+F_{Bi}$. The colored curves represent the flux rate equation calculated for various sticking coefficients ratios $\frac{k_{Sb}}{k_{Bi}}$ at constant F_{Bi}.

ing coefficient describes the relation between the impinging and the incorporated atoms into the crystal. Figure 5.8 shows calculated curves for the flux rate equation with various values for the ratio $\frac{k_{Sb}}{k_{Bi}}$ at $F_{Bi} = constant$. The data is in between the curves $k_{Sb}/k_{Bi} = 0.3$ and 0.2 fitting to the sticking coefficient ratio $\frac{k_{Sb}}{k_{Bi}} = 0.24$.

The growth of bismuth selenide with additional applied Sb flux combined with the Se rich growth conditions results in an increase of the growth rate and consequently an increased layer-thickness (figure 5.9), as determined by analysis of XRD fringes next to the layer peaks. The observed increase of layer-thickness implies an incorporation of the Sb during the growth, whereas for layers with higher Sb content $x > 0.6$ the layer roughness is to high to observe XRD thickness fringes. The extrapolation of the layer thickness at $x = 1.0$ results in 162 nm instead of the expected value of about 200 nm. Possible reasons for this deviation of the expected and measured layer thicknesses are the underestimating of layer thickness due to the extrapolation of layers with increasing roughness for increasing the Sb content, over estimating the Sb content measured in EDX, or an increased Bi desorption at

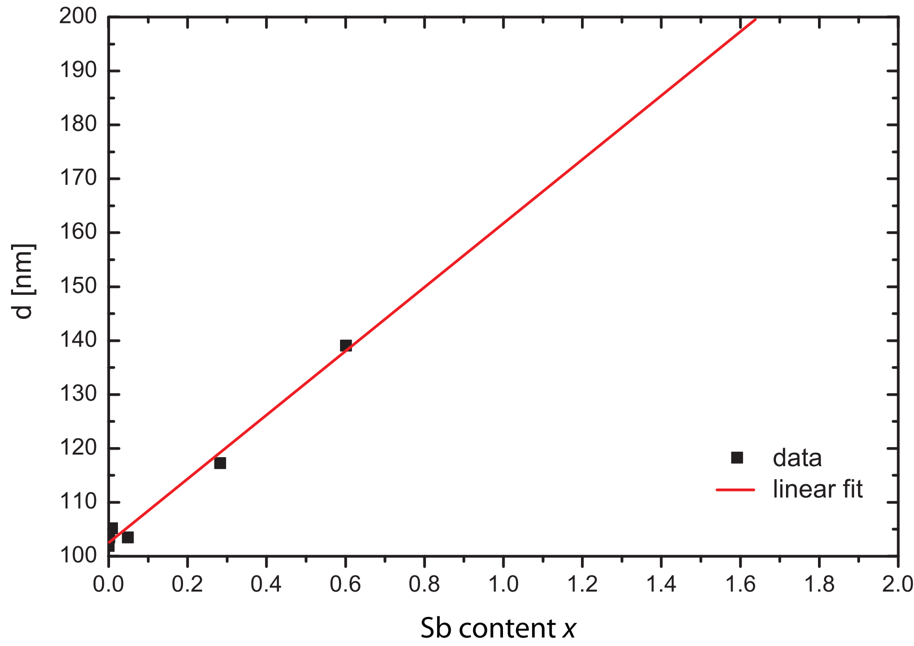

Fig. 5.9: Layer thickness determined by XRD thickness fringes of the Bragg reflections versus the Sb content x fitted linearly (red) and extrapolated.

the surface with increasing the Sb flux. The commonly used technique to precisely determine the layer composition is XRD, whereas for $Bi_{2-x}Sb_xSe_3$ Vegard's law is not applicable due to the crystallization of Sb_2Se_3 Pnma symmetry. Further measurements, such as secondary ion mass spectroscopy would be desirable to clarify the Sb content x in these layers. In the following the x contents determined by EDX measurements of reference samples with known Sb/Bi flux ratio are used to describe the samples, which seems to be the most reliable measurement of Sb content in this layers.

The layers were measured by XRD to determine the structural changes for alloying Bi_2Se_3 with Sb. Figure 5.10 shows wide range θ-2θ diffractograms for different compositions x. The layers with x up to 1.2 show the reflections of the 0 0 l family of the R$\bar{3}$m crystal symmetry beside the InP 111 substrate peak. At a higher Sb concentration, i.e. $x = 1.4$, additional peaks are measured. The origin of these peaks is assigned to the Pnma crystal symmetry of the Sb_2Se_3 structure [ZQT+09]. The intensity of the Pnma (201) and (402) peaks is even higher than these of the R$\bar{3}$m symmetry, suggesting that for $x = 1.4$ a considerable volume of the layer crystallizes in the Pnma symmetry. The Sb_2Se_3 layer ($x = 2$) displays peaks of

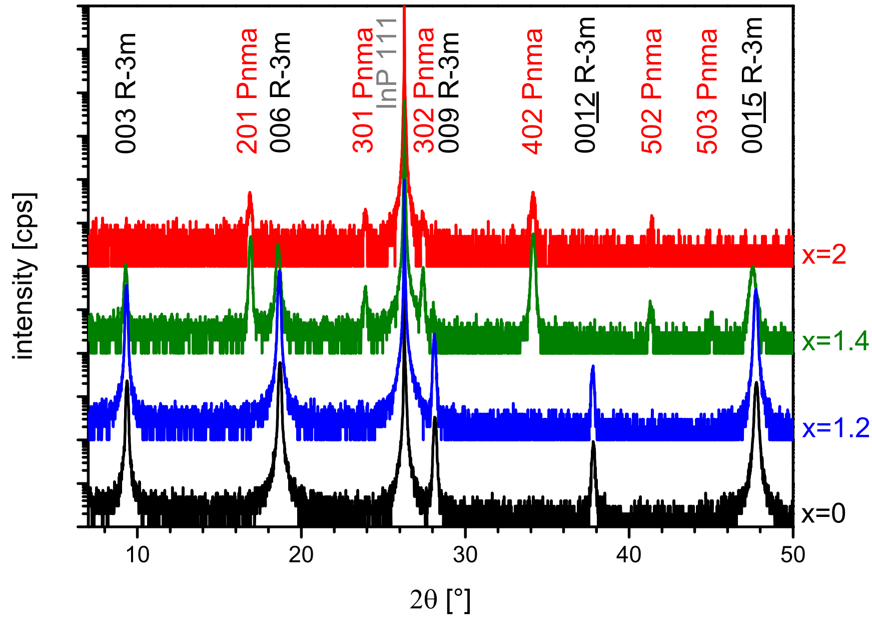

Fig. 5.10: Wide range XRD diffractograms for layers with different Sb contents $x = 0$ (black), $x = 1.2$ (blue), and $x = 1.4$ (green) and $x = 2.0$ (red). The peaks are labeled as InP substrate (grey) or with hkl indices of the layer reflections and the corresponding crystal symmetry R$\overline{3}$m (black) or Pnma (red).

the Pnma crystal symmetry, whereas peaks of the R$\overline{3}$m symmetry are absent in the diffractogram. The presence of the reflections of the (301),(302),(502), (503), (201) and (402) planes indicate a nonuniform out-of-plane crystal orientation within the Sb rich layers (x $\geq$ 1.4). This agrees well with the observed tilted streaks by RHEED at the compositions $x = 1.4$ and $x = 2$. These diffractograms reveal a change in crystal symmetry from the R$\overline{3}$m of Bi_2Se_3 to the Pnma of Sb_2Se_3. The transition of the crystal symmetries is located between the compositions $x = 1.2$ and $x = 1.4$ as determined by XRD.

The effect of twin suppression on the $Bi_{2-x}Sb_xSe_3$ layers is analyzed by XRD. Figure 5.11 illustrates the pole scans of the asymmetric reflections of the {015} planes of layers with Sb content $x = 0.6$ grown on rough InP(111)B:Fe and Si(111) substrates. The layer grown on Si(111) reveals six-fold symmetry of the reflections of the {015} planes and peaks with a FWHM of 3°, indicating twinning and a high mosaicity-twist. In contrast the layer grown on rough InP(111)B:Fe shows three-fold symmetry of the reflections of the {015} planes with a FWHM of 0.4°, as also observed for other Sb contents $x \leq 1.2$, which is a proof of suppressed twin domains.

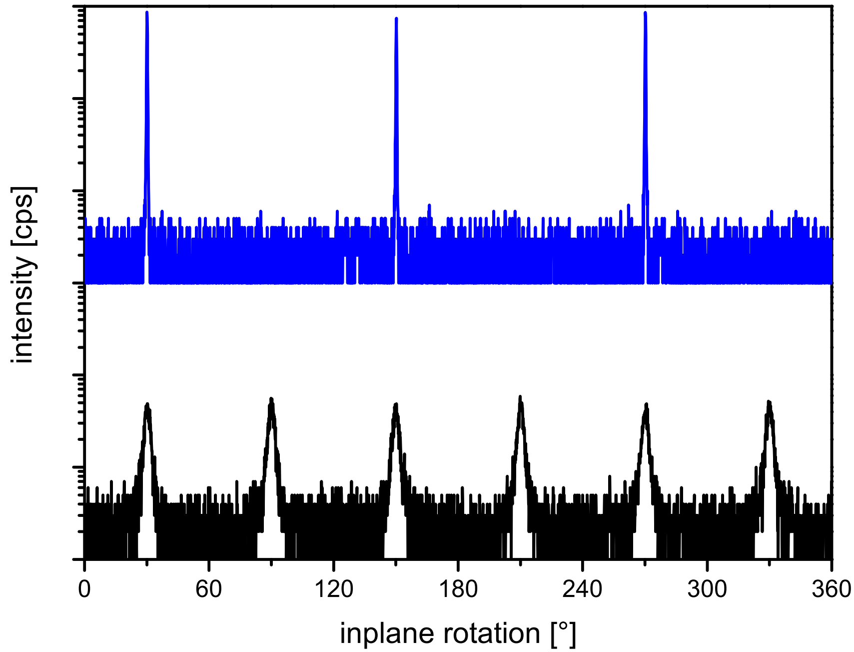

Fig. 5.11: XRD pole scan of the asymmetric reflections of the {015} planes of $Bi_{2-x}Sb_xSe_3$ for layers with the same Sb content $x = 0.6$ grown on different substrates, i.e. on Si(111) (black) and on rough InP(111)B:Fe (blue).

This confirms that the mechanism of twin suppression, as described in section 4.3, is also effective for the $Bi_{2-x}Sb_xSe_3$ layers with the R$\bar{3}$m crystal symmetry, although these layers are not lattice matched to the lateral InP(111) lattice constant. A layer with Sb content of about $x = 0.9$ exhibits a lateral lattice constant a of 4.12 Å, as determined by XRD, resulting in a 0.7% smaller in-plane lattice constant than a_{hex} of InP(111), which is significantly larger than the 0.2% mismatch of Bi_2Se_3 to the substrate. The mosaicity-twist of the $Bi_{2-x}Sb_xSe_3$ alloy grown on rough InP(111)B:Fe with $x = 0.9$ is by an factor of 2 larger than the binary layer of this growth series, indicating an increase of mosaicity-twist with increasing lattice mismatch.

The surface morphology of the $Bi_{2-x}Sb_xSe_3$ layers with R$\bar{3}$m symmetry is analyzed by AFM. The layers with a Sb content $x = 0$ to $x = 1.2$ show a 2D surface with atomically flat terraces. The terraces exhibit steps ranging from one to several QLs of height to the next level. While the Bi_2Se_3 forms triangular shaped terraces on the surface, the Sb alloyed layers show terraces with rounded shape, as observed

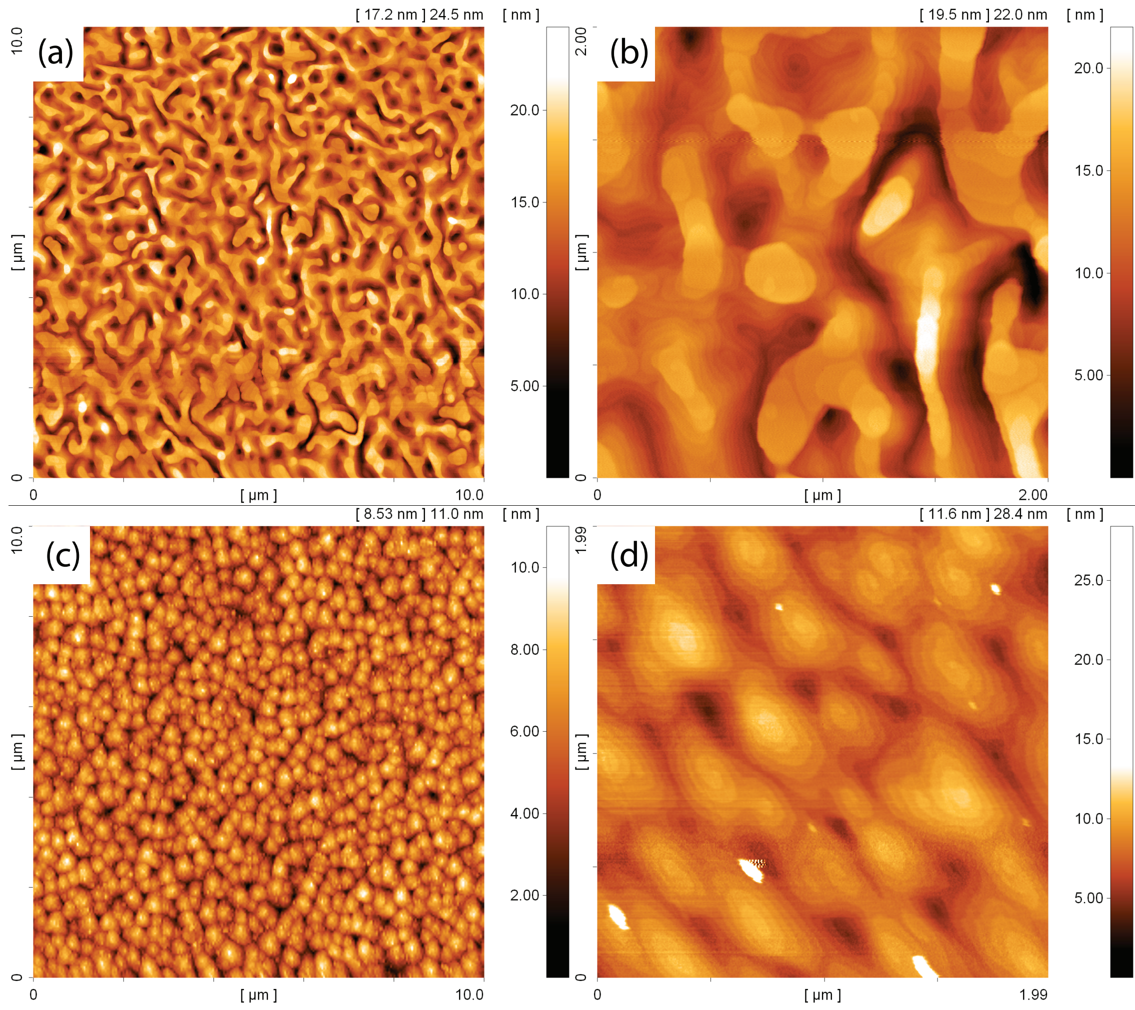

Fig. 5.12: 10×10μm and 2×2μm AFM images of the surface of $Bi_1Sb_1Se_3$ grown at (a), (b) T_{sub} =300°C and (c), (d) T_{sub} =270°C

for $x \geq 0.28$ (figure 5.12).

The morphology of the layers also depends on the growth temperature. At substrate temperatures of T_{sub} = 270°C (BiSe447) circle like growth-spirals are formed (figure 5.12 (c)(d)), in contrast to higher growth temperatures such as T_{sub} = 300°C for which the growth-spirals are connected to each other by ridges (figure 5.12 (a)(b)).

It is worth to mention, that Bi_2Se_3 grown on $Bi_1Sb_1Se_3$ forms triangular shaped terraces and does not adopt the round shape of the layer below (not shown), indicating that the surface morphology of $Bi_{2-x}Sb_xSe_3$ layers is an intrinsic property of this material system.

The $Bi_{2-x}Sb_xSe_3$ layers grown on InP(111) are analyzed by magneto-transport

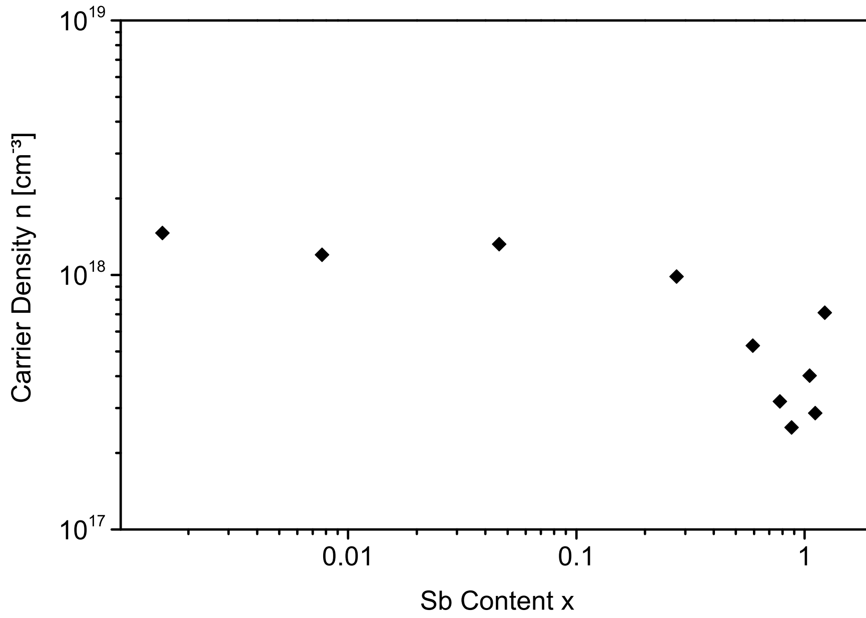

Fig. 5.13: Carrier density (n-type) versus Sb content x of $Bi_{2-x}Sb_xSe_3$ layers grown on rough InP(111)B:Fe

measurements at 4.2 K to determine the electrical properties. As shown in figure 5.13, the layers grown on InP(111) with Sb content $x \leq 0.3$ exhibit a n-type carrier concentration of about 10^{18} cm^{-3}. The carrier concentration decreases significantly for increasing the Sb content to $x > 0.3$ and shows a minimum of $n = 2.5 \times 10^{17}$ cm^{-3} at $x \approx 1$. Further increase of the Sb content x results in higher carrier concentrations, up to 7×10^{17} cm^{-3} at $x = 1.2$ (figure 5.13). Alloying with the Sb contents $x \geq 1.4$ results in layers with high ohmic resistance, indicating a transition to an insulating phase.

The electron mobility of the $Bi_{2-x}Sb_xSe_3$ layers is plotted in Figure 5.14 and displays relatively high values between 900 and 2400 $\frac{cm^2}{Vs}$, compared to other ternary Bi-based TIs reported in chapter 5.4, without a clear trend for increasing the Sb content x.

The comparison of the electrical properties of a twinned layer on Si(111) with a twin-free layer on rough InP(111)B:Fe under the same growth conditions reveals a seven times higher carrier density and a three times lower electron mobility for growth on Si(111). This confirms the influence of the structural layer quality on the transport properties, i.e. the reduction of carrier density, of the TI films by twin

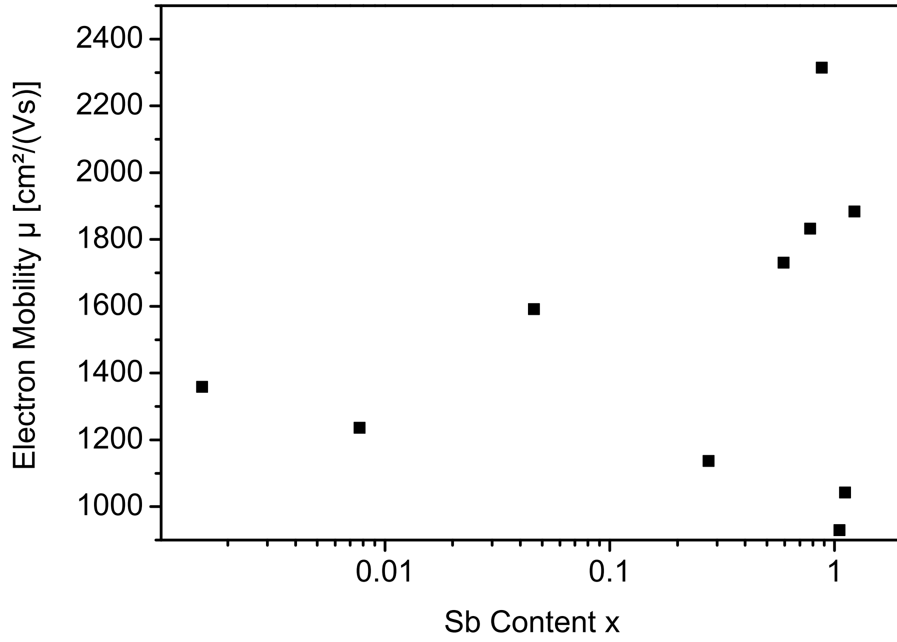

Fig. 5.14: Electron mobility versus Sb content of $Bi_{2-x}Sb_xSe_3$ layers grown on rough InP(111)B:Fe

suppression, as described in section 4.3.
It is worth to mention, that in addition to the magnetotransport for standard characterization with a one carrier model, also a gated Hall bar structure was examined for the layer with the lowest carrier density. The gate voltage shifts the Fermi level of the TIs. By applying a two carrier model, a transition of one carrier from n- to p-type was observed by varying the gate voltage, while the density of the second carrier remained nearly unchanged [Gra16]. Further studies are demanded to clarify the origin of the two carriers in this model or if even further carriers have to be considered.

The electronic band structure of a $Bi_{2-x}Sb_xSe_3$ films is measured with ARPES to analyze the existence of surface states. An amorphous Se cap was grown on top of the films to protect it from ambient conditions during transport to the UHV analysis chamber where the Se cap is thermally removed to obtain a clean surface. Figure 5.15 shows the ARPES spectra of two layers on InP(111) with $x = 0$ and $x = 0.9$. Both layers show the bulk conduction and valance bands. Also the surface states are clearly present within the bulk band gap for the intrinsic layer and the

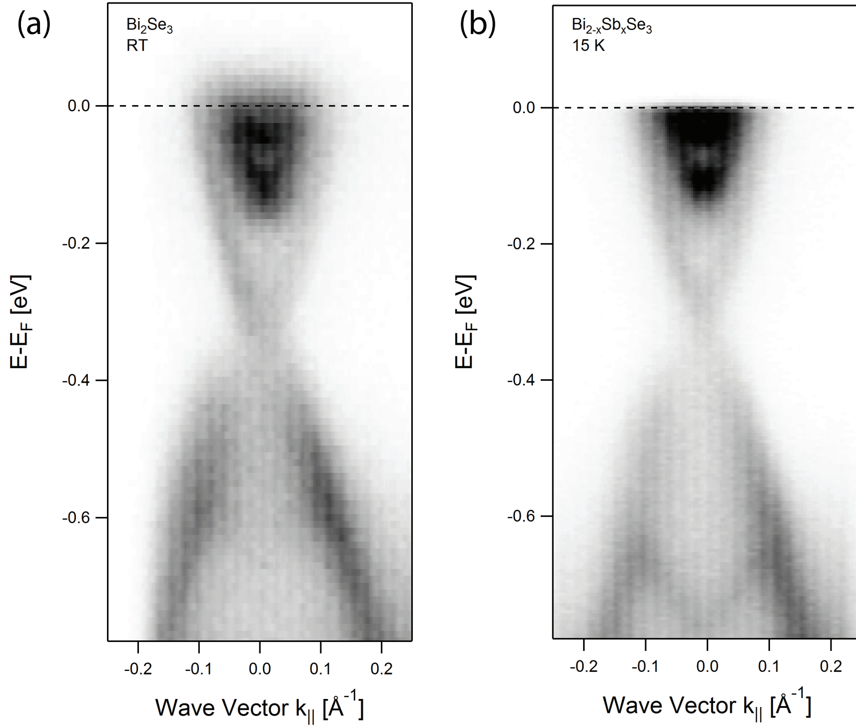

Fig. 5.15: ARPES spectra of $Bi_{2-x}Sb_xSe_3$ with (a) $x = 0$ and (b) $x = 0.9$ grown on InP(111). The spectra were taken by Henriette Maaß (University of Würzburg, Phys. Inst., EP7).

Sb-alloyed layer, confirming the presence of surface states in the alloyed layers with $x = 0.9$, which exhibit the lowest carrier densities. Note that the position of the Fermi level cutting through the conduction band is not necessarily caused by high carrier densities within the bulk of the layer. This material system is known to exhibit for the surface sensitive ARPES measurements a time dependent shift of Fermi level due to adsorbates on the surface [MSS$^+$14].

In summary, the alloying of Bi_2Se_3 with Sb results in V_2VI_3 TI layers, where the group-V site is occupied by both Bi and Sb. The carrier density of these layers decrease with increasing Sb content from $x = 0$ to $x = 0.9$. For higher Sb content a second phase is formed, which crystallizes in the same symmetry as Sb_2Se_3 (Pnma). This change in crystal symmetry is observed at $x = 1.4$ by XRD. The transition to trivial insulating behavior calculated for Sb_2Se_3 by Zhang et al. is observed for layers with $x \geq 1.4$, which goes along with the change of crystal symmetry from $R\bar{3}m$

to Pnma [ZQT+09]. Accordingly, Sb alloying allows to reduce the carrier density to 2.5×10^{17} cm^{-3} without declining the carrier mobility significantly. However, the transition from n- to pure p-type conduction is not observed in the $Bi_{2-x}Sb_xSe_3$ material system.

5.4 $Bi_{2-x}Sb_xTe_{3-y}Se_y$

On the search for insulating Bi-based topological insulators several approaches were made to realize TI devices. Besides the ternary alloys, reports on ARPES and transport measurements of quaternary $Bi_{2-x}Sb_xTe_{3-y}Se_y$ (BSTS) alloys grown from melt show that the Fermi level, as well as the position of the Dirac point is changed by varying the composition of the four elements [RTS+11, ASS+12]. This enables to tune the topological surface states within the band gap and to control the electrical contribution of the bulk in magneto transport measurements.

In this study the progress of MBE of binary and ternary alloys $Bi_{2-x}Sb_xTe_{3-y}Se_y$, as described in the former chapters, is used to find stable growth conditions for quaternary alloys. The quaternary alloys in the whole ranges of x and y are studied in respect to their structural crystalline quality and electrical properties to obtain an almost complete overview of MBE grown Bi-based topological insulators. This allows to identify compositions with low carrier densities and the transition of n-type conduction measured for Bi_2Se_3 and Bi_2Te_3 (see chapters 4.1 and 5.1) to the p-type conduction reported for Sb_2Te_3 grown by codeposition [ZRM01].
The growth conditions of the quaternary layers are adopted from the two studies of $Bi_{2-x}Te_{3-y}Se_y$ and $Bi_{2-x}Sb_xSe_3$ described in sections 5.2 and 5.3 i.e. a growth temperature of T_{sub}=300°C, growth velocity of about 1 nm per minute on undoped hydrogen passivated Si(111) substrates, and the BEP ratios Bi/Sb and Te/Se that are applied to obtain the desired compositions x and y.
During the whole growth of the quaternary alloys a streaky RHEED pattern is observed comparable to these of binary and ternary alloys grown on hydrogen passivated Si(111).

The XRD θ-2θ diffractograms of the $Bi_{2-x}Sb_xTe_{3-y}Se_y$ layers, as shown in figure 5.16, display the reflections of the 0 0 l planes beside the Si(111) planes. The investigated quaternary compositions do not show any other phases than the V_2VI_3, nor any signatures of the Pnma crystal structure of Sb_2Se_3 (see section 5.3). This restricts crystallization in Pnma structure of MBE grown films to Sb and Se rich

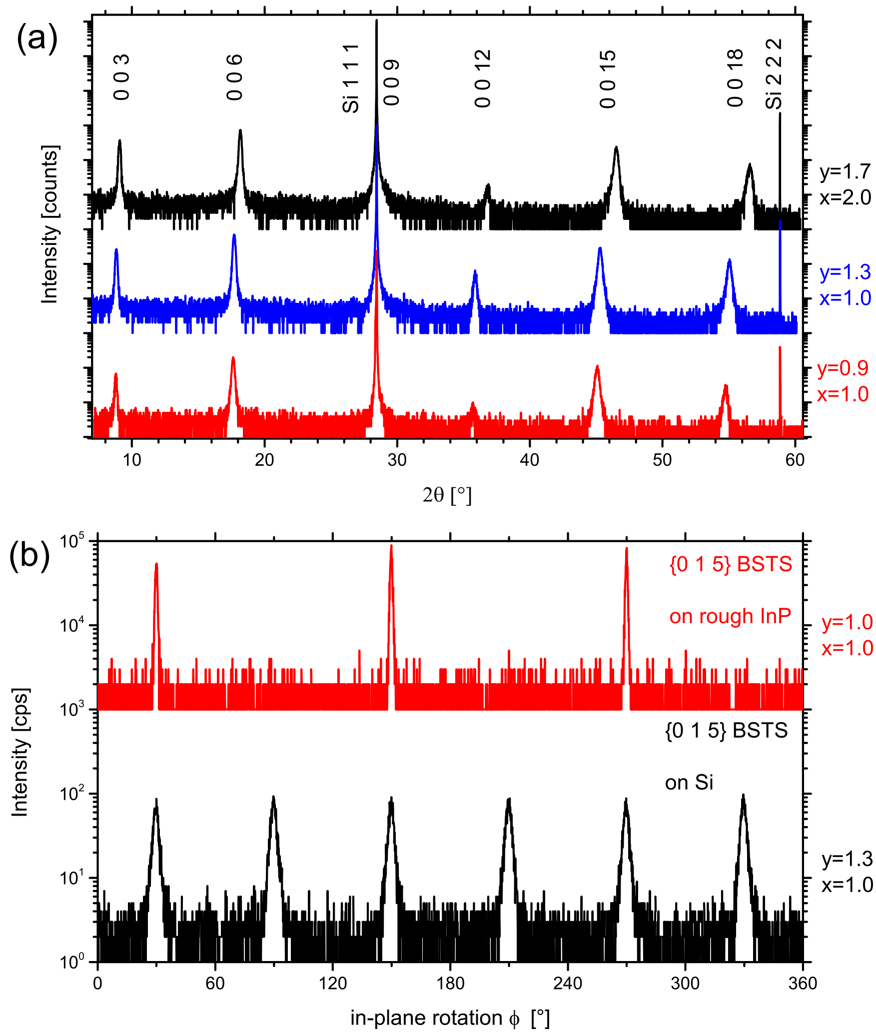

Fig. 5.16: XRD measurements of different compositions (indicated) of BSTS. (a) $\theta - 2\theta$ diffractograms of layers grown on Si(111) displaying 0 0 l reflections. (b) Pole-scans of the asymmetric reflections of the {0 1 5} planes showing three-fold symmetry for growth on rough InP(111)B:Fe (red) and six-fold symmetry for growth on Si(111) (black).

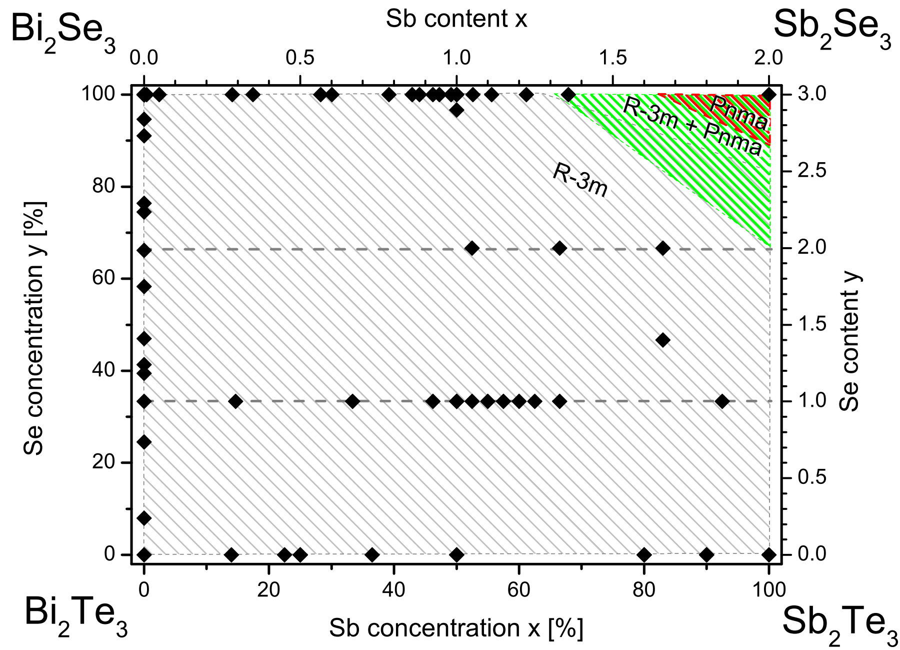

Fig. 5.17: Schematic diagram of the crystal structure (R$\overline{3}$m black, mixed R$\overline{3}$m + Pnma green, and Pnma red) of the layers, based on XRD measurements of the BSTS MBE grown films , in dependence of the x and y content of BSTS (black squares), after Teramoto et al. [TT61].

conditions, as schematically displayed in figure 5.17.

In addition to the growth on Si(111) substrates, a quaternary alloy ($x = 1$, $y = 1$) is also grown on rough InP(111)B:Fe substrate to study the influence of the substrate on these layers. Figure 5.16 (b) shows the pole scans of the asymmetric reflections of the {0 1 5} planes of layers grown on Si(111) and rough InP(111)B:Fe. The layer grown on Si exhibits a six-fold symmetry implying that the layer consists of 60° rotated twin domains. This is in contrast to the layer grown on rough InP(111)B:Fe, which exhibits a three-fold symmetry, proving that the twin suppression, described in section 4.3, also works for non lattice matched Bi-based quaternary alloys. The FWHM of the reflections of the layer grown on InP and Si are 1.2° and 2.7°, respectively, attesting a better in-plane orientation of the layer grown on InP. Nevertheless the FWHM is larger than these observed for Bi_2Se_3 on InP in section 4.3. This suggests, that the increased lattice mismatch to the substrate of the quaternary compound in respect to Bi_2Se_3, results in a increase of the mosaicity-twist for layers grown on InP substrates. It is worth to mention that the mosaicity-twist

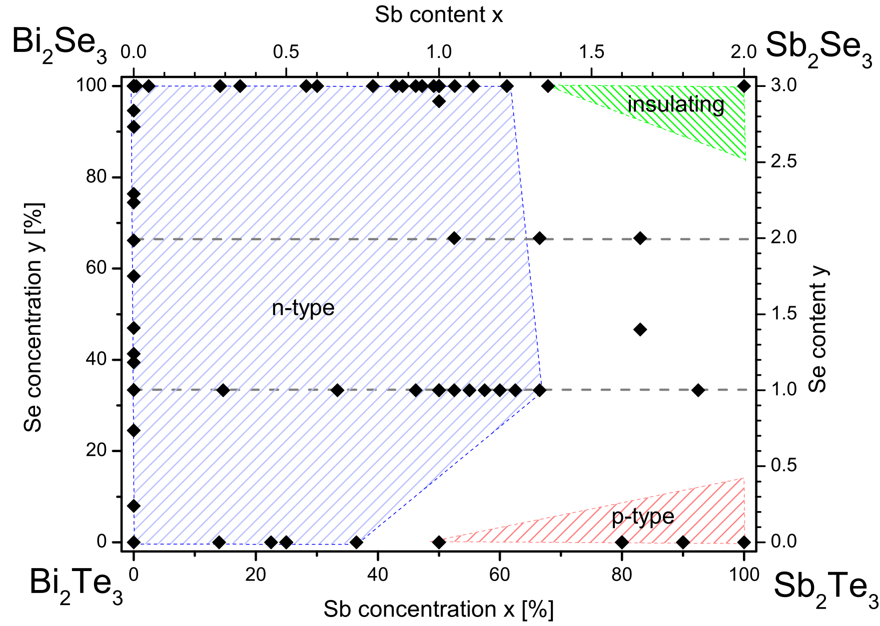

Fig. 5.18: Schematic of the whole $Bi_{2-x}Sb_xSe_3$ composition range x and y, with n-type (blue), p-type (red) conduction, as well as insulating (green) areas indicated. The uncolored area has to be studied in magneto transport to clarify the carrier type in these alloys.

of the quaternary layer grown on rough InP(111)B:Fe substrate is still smaller than that measured for Bi_2Se_3 on Si(111).

Magneto transport measurements of layers grown on Si(111) with fixed Se content $y = 2$ and various Sb content from $x = 0$ to 1.3 show n-type conduction. The lowest carrier concentration is observed for x=1 with $n = 3{\times}10^{18}\text{cm}^{-3}$ and a mobility $\mu = 126\text{cm/Vs}^2$. Whereas the layers with higher and lower Sb content ($x = 0$ and $x = 1.1$) show a higher n-type carrier concentration of $n > 10^{19}\text{cm}^{-3}$. This suggests that a minimum of n-type carriers is located close to $x = 1.0$.

To observe the transition from n-type to p-type conduction the Se content is reduced to $y = 0$ resulting in a p-type carrier concentration of $n = 7.6{\times}10^{19}\text{cm}^{-3}$. The pn-transition for the ternary alloys with $y = 0$ is determined to lie between the Sb content $x = 0.7$ and 1.0. Figure 5.18 shows a schematic overview of the observed carrier types for the Bi-based TIs. The measured areas are colored blue for n-type and red for p-type conduction. Since the focus of the following studies, described in

section 6, is on the pn-transition of the ternary alloy $Bi_{2-x}Sb_xTe_3$ the pn-transition at higher Sb contents (white area) is subject to ongoing research.

In summary, the quaternary BSTS alloys are realized by MBE growth in a comparable quality as the binary and ternary alloys grown on Si(111). The carrier density is tuned by varying the Sb and Se content to a value as low as $n = 3\times10^{18}\text{cm}^{-3}$ at $x = 1$ and $y = 2$. In addition, pn-transitions are observed between the quaternary alloy ($x = 1.0$, $y = 2.0$) and the ternary alloy (x=1.0, $y = 0$), as well as at the $Bi_{2-x}Sb_xTe_3$ branch between the Sb content $x = 0.7$ and $x = 1.0$. This paves the way for bulk insulating magnetically doped Bi-based TIs, as studied in chapter 6.

6 Magnetic doping of topological insulators

Magnetic Bi-based TIs have been predicted to exhibit exotic physical phenomena, such as the quantized anomalous Hall effect (QAHE) in 2010 [YZZ+10]. Subsequently the QAHE was experimentally observed in thin Cr- and V-doped $Bi_{2-x}Sb_xTe_3$ layers, in 2013 and 2015, respectively [CZF+13, CZK+15]. The growth of the magnetically doped ternary TIs exhibiting the QAHE is challenging, since the influences of substrate choice, layer quality, protecting cap-layer and lithography processing, as well as the mechanism of the incorporation of magnetic dopants remain unclear. A comparison of Cr- and V-doped Sb_2Te_3 shows that the Curie temperature of V-doped layers is by a factor of two and the coercive field by an order of magnitude higher than for the Cr-doped layers, attesting the V-doped layers to be more advantageous for a robust ferromagnetic topological insulator system, whereas the valance states of the magnetic dopants in these TIs are not exactly determined, suggesting the valance state of Vanadium in V-doped Sb_2Te_3 to be a mixture of 3+ and 4+ (or/and 5+) for replacing the Sb with valance state 3+ [CZK+15].
In this study, the influence of magnetic doping on the structural quality on Bi-based TIs is investigated by incorporation of Cr atoms in $Bi_{2-x}Sb_xTe_3$ layers. Therefore, Cr-doped bulk layers with varying Cr concentrations were grown on hydrogen passivated Si(111) substrates. The substrate temperature, as well as Bi-, Te-, and Sb-fluxes were kept constant to obtain a Sb content of nominally $x = 1.6$, while the Cr cell temperature was varied in the range of T_{Cr}=1150°C to 1300°C (BEP measurements are hindered by the high Cr cell temperature causing background pressures of $p_{BGR} > 10^{-8}$ mbar and the getter effect of chromium) [SMS82]. The

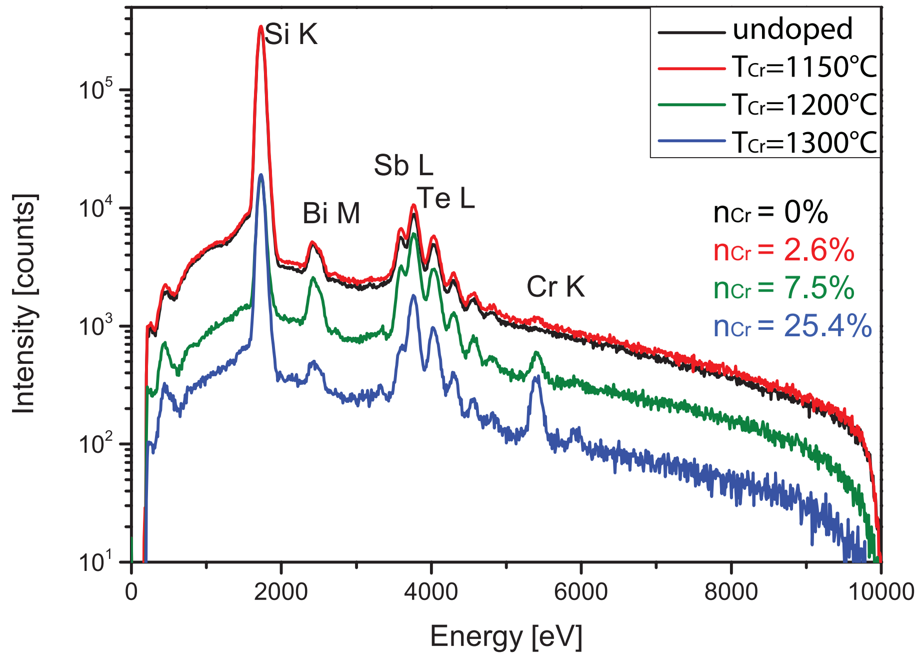

Fig. 6.1: EDX spectra of $Bi_{2-x}Sb_xTe_3$ layers with different Cr concentrations n_{Cr}. The measurement time of layers with Cr concentration below 3% is increased to obtain a better signal to noise ratio.

growth time of the samples is 60 min resulting in a layer thickness of about 40 nm for undoped layers, except for the layer grown at T_{Cr}=1200°C, here the growth time is increased by an factor of 4 to obtain a larger layer volume for a more precise EDX measurement.

EDX spectra shown in Figure 6.1 are measured to determine the Cr concentration of these layers. The EDX spectra confirms an increase of the atomic Cr concentration n_{Cr} with increasing the Cr cell temperature of 2.6% ($z = 0.13$), 7.9% ($z = 0.4$), and 25.4% ($z = 1.27$), for Cr cell temperatures of 1150°C, 1200°C, and 1300°C, respectively. The quantitative analysis of the EDX reveals an almost constant relation of the $(n_{Bi}+n_{Sb}+n_{Cr}):n_{Te}$ ratio of 2:3 for all layers, suggesting an incorporation of Cr on the group-V crystal sites. This implies, that the use of the chemical formula $Cr_z(Bi_{(2-x)/2}Sb_x/2)_{2-z}Te_3$, with $z = \frac{n_{Cr}}{100\%} \cdot 5$, is reasonable to describe the magnetically doped alloy. The effect of the magnetic doping on the carrier density was not studied in detail, whereas a Cr-doped $(Bi_1Sb_1)Se_3$ exhibits p-type conduction in contrast to the undoped samples described in chapter 5.3, implying that Cr acts

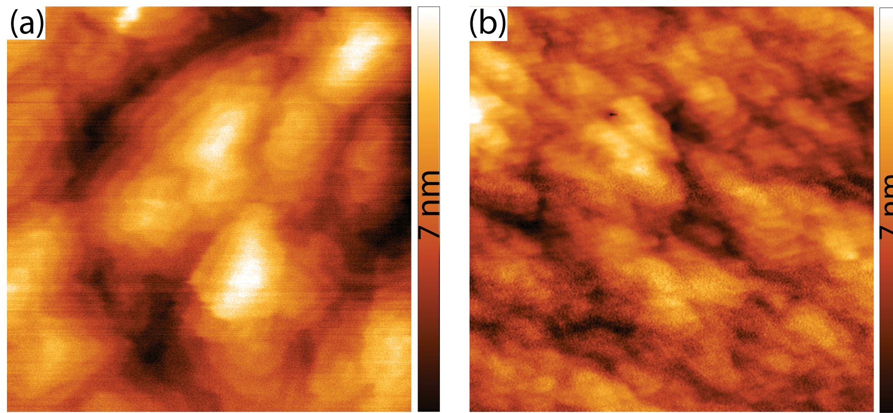

Fig. 6.2: 2×2 μm AFM images of the surface of undoped (a), and 2.6 % Cr-doped $(BiSb)_2Te_3$ layers of about 40 nm thickness. The z-scale is labeled with the height distribution.

as an electron acceptor in Bi-based TIs.

The layers are analyzed by AFM to examine the influence of Cr doping on the structural quality. Figure 6.2 displays the surfaces of $Cr_z(Bi_{0.2}Sb_{0.8})_{2-z}Te_3$ layers with a Cr content of $z = 0.0$ and $z = 0.13$. The surface of the undoped layer reveals irregular formed island structures and terraces with steps of about one QL height with a width of up to 90 nm. The Cr-doped layer has smaller domains compared to the undoped layer and terraces separated by QL steps are visible only in few areas of the surface. Both surfaces exhibit merged structures and several nanometer deep trenches between islands, which is a signature of twinning in these layers.

The influence of Cr on the crystal structure of $Bi_{2-x}Sb_xTe_3$ is analyzed by XRD. The wide range θ-2θ diffractograms, displayed in figure 6.3, show peaks of the $(BiSb)_2Te_3$ 0 0 $3n$ family and the Si substrate for the undoped, and Cr-doped layers up to n_{Cr} =8%. The 25.4% Cr-doped sample shows two additional peaks, as marked by blue arrows in figure 6.3, addressed to the crystal structure of Cr_2Te_3 ($P\overline{3}1c$) indicating a structural change for higher Cr concentration [And70]. The peak positions of the 0 0 $3n$ reflections are shifted to higher angles for increasing the Cr concentration, which is clearly visible for the region of 0 0 6 reflections enlarged in the inset of figure 6.3. This reveals a decrease of the lattice constant c

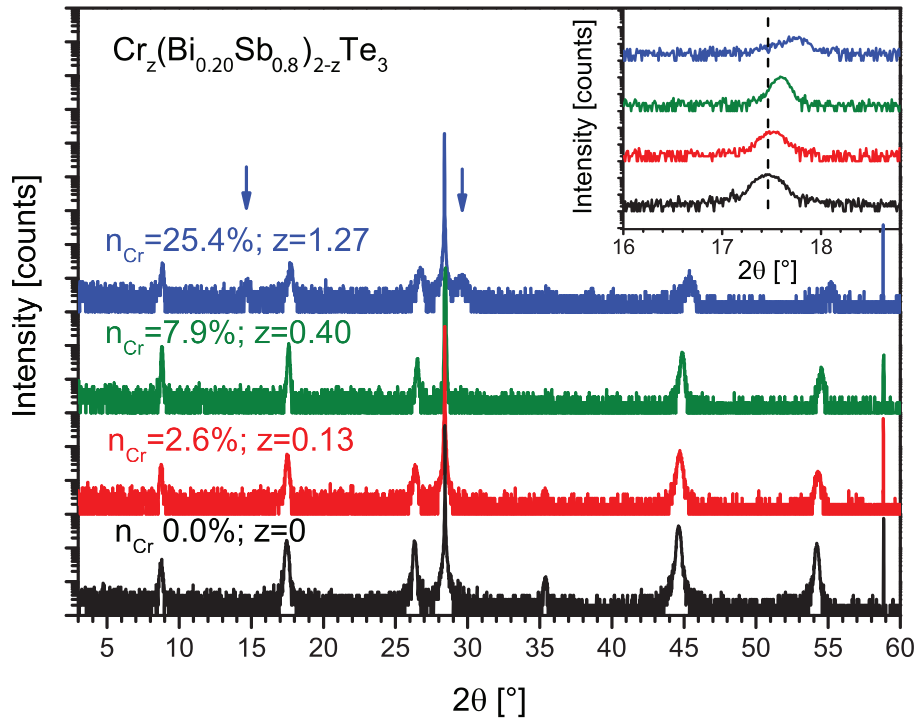

Fig. 6.3: XRD diffractograms of the Cr-doped $(BiSb)_2Te_3$ layers. The additional peaks corresponding to the $P\overline{3}1c$ symmetry of Cr_2Te_3 at z=1.27 are marked by blue arrows. The inset shows a zoom to the 0 0 6 reflections of the layers, with the dashed line marking the peak position of the undoped layer. Curves shifted for clarity.

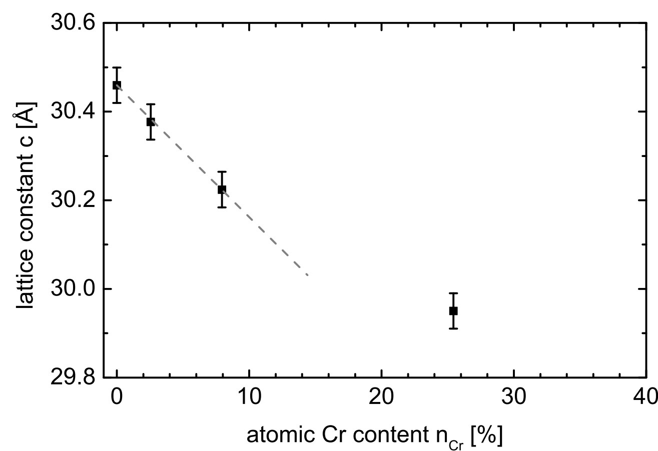

Fig. 6.4: Lattice constant c plotted as a function of the atomic Cr concentration n_{Cr} measured by XRD. The dashed line is a guide for the eye.

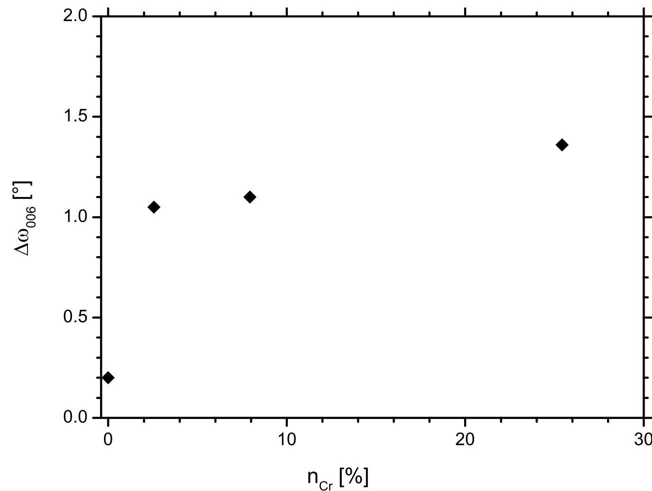

Fig. 6.5: Rocking curve FWHMs of the 0 0 6 reflection plotted as a function of the atomic Cr concentration n_{Cr} measured by XRD.

with increasing Cr concentration, which is linear for doping contents up to $z = 0.4$, as shown in figure 6.4. This can be explained by the substitution of the Bi and Sb atoms by Cr with a smaller ionic radius confirming the incorporation on group-V lattice sites.

The out of plane tilt of the layers is measured by rocking curves of the 0 0 6 reflection, displayed in figure 6.5, as a measure of the structural layer quality. The Cr-doped layer with $z = 0.13$ exhibits a by a factor of five larger rocking curve FWHM of 1.0° compared to the undoped layer. The FWHM further increases with increasing the Cr concentration. This reveals a decrease of crystalline quality with increasing Cr-doping level.

In addition to the characterization of structural quality of the layers, also magnetic and electrical measurements were performed, such as magneto-transport and SQUID (superconducting quantum interference device). These measurements confirm that the Cr-doping results in magnetic TI layers with an out-of-plane magnetization. The anomalous Hall resistivity determined for a 6 nm $Cr_{0.13}Bi_{0.37}Sb_{1.50}Te_3$ film, as shown in figure 6.6 (a), is about 0.35 h/e^2 with a coercive field of about 80 mT. It is worth to mention, that by changing the magnetic dopant to Vanadium and fine tuning of the Sb content to achieve charge neutrality at low growth tem-

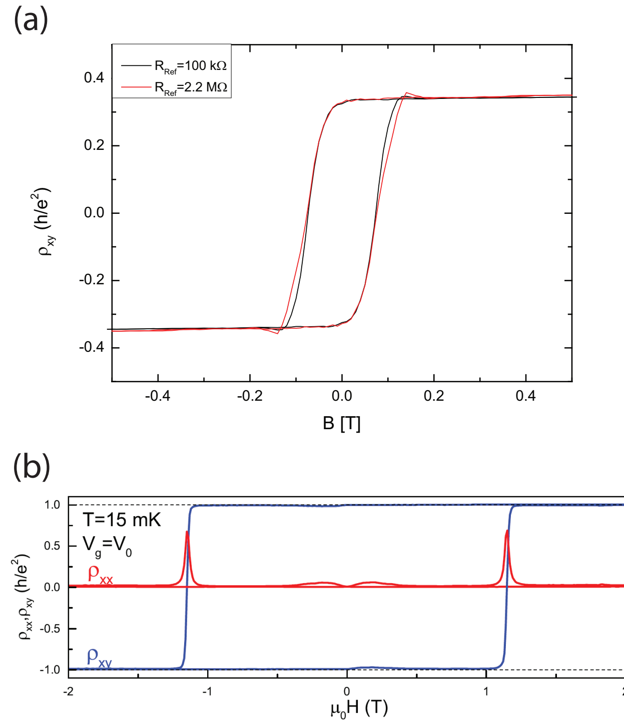

Fig. 6.6: Magneto transport at mK temperatures of magnetically doped TIs of (a) 6 nm $Cr_{0.13}Bi_{0.37}Sb_{1.50}Te_3$ on H passivated Si(111) displaying the anomalous Hall effect for two different reference resistance at 30mK (measured by Stefan Grauer, University of Würzburg, Phys. Inst., EP3) and (b) 10 nm $V_{0.11}Bi_{0.445}Sb_{1.4}Te_{3.045}$ on H-passivated Si(111) exhibiting the quantum anomalous Hall effect [GSW+15].

peratures (190°), the magnetotransport measurements result in the observation of the quantized anomalous Hall effect with a coercive field of about 1.2 T, as shown in figure 6.6 (b) [GSW+15].

In conclusion, the magnetic doping with Cr decreased the mosaicity-size and increases the out-of-plane mosaicity-tilt of the domains resulting in a lower structural crystalline quality of the $Bi_{2-x}Sb_xTe_3$ layers grown on hydrogen passivated Si(111). The EDX measurements result in a (Bi+Sb+Cr):Te ratio of 2:3 for all Cr-doped layers. This constant ratio, combined with the linear decrease of the c lattice parameter for Cr contents up to $z = 0.4$ as determined by XRD, indicate a preferential incorporation of Cr atoms at group-V sites. The smaller ionic radius of the Cr atom, compared to Sb and Bi, decreases the lattice constants. Nevertheless, the presence of defects, such as interstitials, antisites, Cr-decorated domain boundaries, Cr_2Te_3-,

and Cr-clusters, is possible in these layers, due to the limited sensitivity of XRD and EDX.

In magnetotransport measurements the Cr-doped $Bi_{2-x}Sb_xTe_3$ layers exhibit an out-of-plane magnetization and an anomalous Hall effect, whereas the Vanadium-doped $Bi_{2-x}Sb_xTe_3$ layers resulted in the observation of the QAHE.

Bibliography

[ACF+96] L. A. Almeida, Y. P. Chen, J. P. Faurie, S. Sivananthan, David J. Smith, and S. C. Y. Tsen. Growth of high quality CdTe on Si substrates by molecular beam epitaxy. *J. Electron. Mater.*, 25(8):1402–1405, 1996.

[And70] Arne F Andresen. Magnetic structure of Cr_2Te_3, Cr_3Te_4, and Cr_5Te_6. *Acta Chem. Scand.*, 24(10):3495–3509, 1970.

[ASS+12] T. Arakane, T. Sato, S. Souma, K. Kosaka, K. Nakayama, M. Komatsu, T. Takahashi, Zhi Ren, Kouji Segawa, and Yoichi Ando. Tunable Dirac cone in the topological insulator $Bi_{2-x}Sb_xTe_{3-y}Se_y$. *Nat. Commun.*, 3:636–, 2012.

[Bea67] J. A. Bearden. X-ray wavelengths. *Rev. Mod. Phys.*, 39:78–124, 1967.

[BHZ06] B. Andrei Bernevig, Taylor L. Hughes, and Shou-Cheng Zhang. Quantum spin Hall effect and topological phase transition in HgTe quantum wells. *Science*, 314(5806):1757–1761, 2006.

[Bir06] Mario Birkholz. *Thin film analysis by X-ray scattering*. John Wiley & Sons, 2006.

[BKE+11] Namrata Bansal, Yong Seung Kim, Eliav Edrey, Matthew Brahlek, Yoichi Horibe, Keiko Iida, Makoto Tanimura, Guo-Hong Li, Tian Feng, Hang-Dong Lee, Torgny Gustafsson, Eva Andrei, and Seongshik Oh. Epitaxial growth of topological insulator Bi_2Se_3 film on Si(111) with atomically sharp interface. *Thin Solid Films*, 520(1):224–229, 2011.

[Bra99] Wolfgang Braun. *Applied RHEED: Reflection high-energy electron diffraction during crystal growth*, volume 154 of *Springer tracts in modern physics*. Springer, Berlin, 1999.

[Che09] Y. L. Chen. Experimental realization of a three-dimensional topological insulator, Bi_2Te_3. *Science*, pages 2009; VOL 325; ISSU 5937, 178–180, 2009.

[CZF+13] Cui-Zu Chang, Jinsong Zhang, Xiao Feng, Jie Shen, Zuocheng Zhang, Minghua Guo, Kang Li, Yunbo Ou, Pang Wei, Li-Li Wang, et al. Experimental observation of the quantum anomalous Hall effect in a magnetic topological insulator. *Science*, 340(6129):167–170, 2013.

[CZK+15] Cui-Zu Chang, Weiwei Zhao, Duk Y Kim, Haijun Zhang, Badih A Assaf, Don Heiman, Shou-Cheng Zhang, Chaoxing Liu, Moses HW Chan,

and Jagadeesh S Moodera. High-precision realization of robust quantum anomalous Hall state in a hard ferromagnetic topological insulator. *Nat. Mater.*, 14(5):473–477, 2015.

[EZK+13] Ilias Efthimiopoulos, Jiaming Zhang, Melvin Kucway, Changyong Park, Rodney C. Ewing, and Yuejian Wang. Sb_2Se_3 under pressure. *Sci. Rep.*, 3:2665, 2013.

[FBB89] D. B. Fenner, D. K. Biegelsen, and R. D. Bringans. Silicon surface passivation by hydrogen termination: A comparative study of preparation methods. *J. Appl. Phys.*, 66(1):419–424, 1989.

[FGT+88] J.P. Fleurial, L. Gailliard, R. Triboulet, H. Scherrer, and S. Scherrer. Thermal properties of high quality single crystals of bismuth telluride part I: Experimental characterization. *J. Phys. Chem. Solids*, 49(10):1237 – 1247, 1988.

[FK08] Liang Fu and C. L. Kane. Superconducting proximity effect and majorana fermions at the surface of a topological insulator. *Phys. Rev. Lett.*, 100:096407, 2008.

[FKM07] L. Fu, C. L. Kane, and E. J. Mele. Topological insulators in three dimensions. *Phys. Rev. Lett.*, 98:106803–, 2007.

[FNS79] S Fung, R J Nicholas, and R A Stradling. A study of the deep acceptor levels of iron in InP. *J. Phys. Chem. Solids. C. Solid Sate*, 12(23):5145, 1979.

[FO71] T. A. Flaim and P. D. Ownby. Observations on Bayard-Alpert ion gauge sensitivities to various gases. *J. Vac. Sci. Technol.*, 8(5):661–662, 1971.

[GM03] Iosif Galanakis and Phivos Mavropoulos. Zinc-blende compounds of transition elements with N, P, As, Sb, S, Se, and Te as half-metallic systems. *Phys. Rev. B*, 67(10):104417, 2003.

[GNE+12] Joseph Goldstein, Dale E Newbury, Patrick Echlin, David C Joy, Alton D Romig Jr, Charles E Lyman, Charles Fiori, and Eric Lifshin. *Scanning electron microscopy and X-ray microanalysis: A text for biologists, materials scientists, and geologists.* Springer Science & Business Media, 2012.

[Gra10] S. Grauer. *Transportmessungen an Bi_2Se_3*. Diplomarbeit, Universität Würzburg, Phys. Inst., EP3, 2010.

[Gra16] Stefan Grauer. *Transport Phenomena in Bi_2Se_3 and related compounds.* PhD thesis, Universität Würzburg, Phys. Inst., EP3 (submitted), 2016.

[GSW+15] S. Grauer, S. Schreyeck, M. Winnerlein, K. Brunner, C. Gould, and L. W. Molenkamp. Coincidence of superparamagnetism and perfect quantization in the quantum anomalous Hall state. *Phys. Rev. B*, 92:201304, 2015.

[HCK86] J. Horak, K. Cermak, and L. Koudelka. Energy formation of antisite defects in doped Sb_2Te_3 and Bi_2Te_3 crystals. *J. Phys. Chem. Solids*, 47(8):805 – 809, 1986.

[HK69] R E Honig and D A Kramer. Vapor pressure data for the solid and liquid elements. *RCA Rev.*, 30:285–305, 1969.

[HQW+08] D. Hsieh, D. Qian, L. Wray, Y. Xia, Y. S. Hor, R. J. Cava, and M. Z. Hasan. A topological Dirac insulator in a quantum spin Hall phase. *Nature*, 452(7190):970–974, 2008.

[HRR+09] YS Hor, A Richardella, P Roushan, Y Xia, JG Checkelsky, A Yazdani, MZ Hasan, NP Ong, and RJ Cava. p-type for topological insulator and low-temperature thermoelectric applications. *Phys. Rev. B*, 79(19):195208, 2009.

[HS96] Marian A. Herman and H. Sitter. *Molecular Beam Epitaxy: Fundamentals and Current Status*. Springer series in materials science. Springer, 1996.

[Hun09] Siegfried Hunklinger. *Festkörperphysik*. Oldenbourg Verlag, 2009.

[HXQ+09] D. Hsieh, Y. Xia, D. Qian, L. Wray, J. H. Dil, F. Meier, J. Osterwalder, L. Patthey, J. G. Checkelsky, N. P. Ong, A. V. Fedorov, H. Lin, A. Bansil, D. Grauer, Y. S. Hor, R. J. Cava, and M. Z. Hasan. A tunable topological insulator in the spin helical Dirac transport regime. *Nature*, 460(7259):1101–1105, 2009.

[HXW+11] Liang He, Faxian Xiu, Yong Wang, Alexei V. Fedorov, Guan Huang, Xufeng Kou, Murong Lang, Ward P. Beyermann, Jin Zou, and Kang L. Wang. Epitaxial growth of Bi_2Se_3 topological insulator thin films on Si (111). *J. Appl. Phys.*, 109(10):103702, 2011.

[IC04] Ayahiko Ichimiya and Philip I. Cohen. *Reflection high-energy electron diffraction*. Cambridge Univ. Press, Cambridge, 2004.

[IL09] Harald Ibach and Hans Lüth. *Festkörperphysik: Einführung in die Grundlagen*. Springer-Verlag, 2009.

[Kai55] Y. Kainuma. The Theory of Kikuchi patterns. *Acta Cryst.*, 8(5):247–257, 1955.

[KFA95] P Kidd, P F Fewster, and N L Andrew. Interpretation of the diffraction profile resulting from strain relaxation in epilayers. *J. Phys. D: Appl. Phys.*, 28(4A):A133, 1995.

[Kit13] Charles Kittel. *Einführung in die Festkörperphysik*. Oldenbourg Verlag, 2013.

[KM05] Charles L Kane and Eugene J Mele. Z 2 topological order and the quantum spin hall effect. *Phys. Rev. Lett.*, 95(14):146802, 2005.

[Kom92] Atsushi Koma. Van der waals epitaxy - a new epitaxial growth method for a highly lattice-mismatched system. *Thin Solid Films*, 216(1):72 – 76, 1992. Papers presented at the International Workshop on Science and Technology of Thin Films for the 21st Century, Evanston,IL, USA, July 28-August 2, 1991.

[KWB+07] Markus König, Steffen Wiedmann, Christoph Brüne, Andreas Roth, Hartmut Buhmann, Laurens W. Molenkamp, Xiao-Liang Qi, and Shou-Cheng Zhang. Quantum spin Hall insulator state in HgTe quantum wells. *Science*, 318(5851):766–770, 2007.

[KY86] Atsushi Koma and Kazuki Yoshimura. Ultrasharp interfaces grown with van der waals epitaxy. *Surf. Sci.*, 174(1-3):556–560, 1986.

[LGL+13] Handong Li, Lei Gao, Hui Li, Gaoyun Wang, Jiang Wu, Zhihua Zhou, and Zhiming Wang. Growth and band alignment of Bi_2Se_3 topological insulator on H-terminated Si(111) van der Waals surface. *Appl. Phys. Lett.*, 102(7), 2013.

[LLG+13] Y. Liu, Y. Y. Li, D. Gilks, V. K. Lazarov, M. Weinert, and L. Li. Charging Dirac states at antiphase domain boundaries in the three-dimensional topological insulator Bi_2Se_3. *Phys. Rev. Lett.*, 110:186804, 2013.

[LLH05] Hanna Lind, Sven Lidin, and Ulrich Häussermann. Structure and bonding properties of $(Bi_2Se_3)_m(Bi_2)_n$ stacks by first-principles density functional theory. *Phys. Rev. B*, 72:184101, 2005.

[LSE+14] Gabriel Landolt, Steffen Schreyeck, Sergey V. Eremeev, Bartosz Slomski, Stefan Muff, Jürg Osterwalder, Evgueni V. Chulkov, Charles Gould, Grzegorz Karczewski, Karl Brunner, Hartmut Buhmann, Laurens W. Molenkamp, and J. Hugo Dil. Spin texture of Bi_2Se_3 thin films in the quantum tunneling limit. *Phys. Rev. Lett.*, 112:057601, Feb 2014.

[LWK+10] H D Li, Z Y Wang, X Kan, X Guo, H T He, Z Wang, J N Wang, T L Wong, N Wang, and M H Xie. The van der Waals epitaxy of Bi_2Se_3 on the vicinal Si(111) surface: An approach for preparing high-quality thin films of a topological insulator. *New J. Phys.*, 12(10):103038–, 2010.

[LWQZ10] Rundong Li, Jing Wang, Xiao-Liang Qi, and Shou-Cheng Zhang. Dynamical axion field in topological magnetic insulators. *Nat. Phys.*, 6(4):284–288, 2010.

[ML33] WJ Müller and G Löffler. Zur Kenntnis der Färbung von gefälltem Cadmiumsulfid. *Angewandte Chemie*, 46(33):538–539, 1933.

[MLS63] G. R. Miller, Che-Yu Li, and C. W. Spencer. Properties of Bi_2Te_3-Bi_2Se_3 alloys. *J. Appl. Phys.*, 34(5):1398–1400, 1963.

[MSS+14] H. Maaß, S. Schreyeck, S. Schatz, S. Fiedler, C. Seibel, P. Lutz, G. Karczewski, H. Bentmann, C. Gould, K. Brunner, L. W. Molenkamp, and F. Reinert. Electronic structure and morphology of epitaxial $Bi_2Te_2Se_1$ topological insulator films. *J. Appl. Phys.*, 116(19), 2014.

[Nak63] Seizo Nakajima. The crystal structure of $Bi_2Te_{3-x}Se_x$. *J. Phys. Chem. Solids*, 24(3):479–485, 1963.

[OPM+15] M. Orlita, B. A. Piot, G. Martinez, N. K. Sampath Kumar, C. Faugeras, M. Potemski, C. Michel, E. M. Hankiewicz, T. Brauner, Č. Drašar, S. Schreyeck, S. Grauer, K. Brunner, C. Gould, C. Brüne, and L. W. Molenkamp. Magneto-optics of massive Dirac fermions in bulk Bi_2Se_3. *Phys. Rev. Lett.*, 114:186401, 2015.

[Pal98] Edward D Palik. *Handbook of optical constants of solids*, volume 3. Academic press, 1998.

[Par85] E.H.C. Parker. *The Technology and Physics of Molecular Beam Epitaxy.* Plenum Press, 1985.

[PWHS99] Edward Prince, Arthur James Cochran Wilson, Theo Hahn, and U Shmueli. *International tables for crystallography.* International Union of Crystallography, 1999.

[Reu10] M. Reuss. *Transporteigenschaften dreidimensionaler topologischer Isolatoren.* Masterarbeit, Universität Würzburg, Phys. Inst., EP3, 2010.

[RTS+10] Zhi Ren, A. A. Taskin, Satoshi Sasaki, Kouji Segawa, and Yoichi Ando. Large bulk resistivity and surface quantum oscillations in the topological insulator $Bi_2Te_{3-x}Se_x$. *Phys. Rev. B*, 82:241306, 2010.

[RTS+11] Zhi Ren, A. A. Taskin, Satoshi Sasaki, Kouji Segawa, and Yoichi Ando. Optimizing $Bi_{2/x}Sb_xTe_{3/z}Se_y$ solid solutions to approach the intrinsic topological insulator regime. *Phys. Rev. B*, 84:165311, 2011.

[SBK+16] S Schreyeck, K Brunner, A Kirchner, U Bass, S Grauer, C Schumacher, C Gould, G Karczewski, J Geurts, and L W Molenkamp. Kinetic limitation of chemical ordering in $Bi_2Te_{3-x}Se_x$ layers grown by molecular beam epitaxy. *J. Phys.: Condens. Matter*, 28(14):145002, 2016.

[Sch11] Steffen Schreyeck. *Herstellung und Charakterisierung von topologischen Isolatoren auf Basis von Bi_2Se_3-Schichtsystemen.* Diplomarbeit, Universität Würzburg, Phys. Inst., EP3, 2011.

[SMS82] J.E. Simpkins, P. Mioduszewski, and L.W. Stratton. Studies of chromium gettering. *J. Nucl. Mater.*, 111:827 – 830, 1982.

[SN06] Simon M Sze and Kwok K Ng. *Physics of semiconductor devices*. John Wiley & Sons, 2006.

[STK+13] S. Schreyeck, N. V. Tarakina, G. Karczewski, C. Schumacher, T. Borzenko, C. Brune, H. Buhmann, C. Gould, K. Brunner, and L. W. Molenkamp. Molecular beam epitaxy of high structural quality Bi_2Se_3 on lattice matched InP(111) substrates. *Appl. Phys. Lett.*, 102(4):041914, 2013.

[STS+09] Lothar Spieß, Gerd Teichert, Robert Schwarzer, Herfried Behnken, and Christoph Genzel. *Moderne Röntgenbeugung: Röntgendiffraktometrie für Materialwissenschaftler, Physiker und Chemiker*. Springer-Verlag, 2009.

[TSB+12] N. V. Tarakina, S. Schreyeck, T. Borzenko, C. Schumacher, G. Karczewski, K. Brunner, C. Gould, H. Buhmann, and L. W. Molenkamp. Comparative study of the microstructure of crystal Bi_2Se_3 thin films grown on Si(111) and InP(111) substrates. *Cryst. Growth Des.*, 12(4):19131918, 2012.

[TSB+13] N V Tarakina, S Schreyeck, T Borzenko, S Grauer, C Schumacher, G Karczewski, C Gould, K Brunner, H Buhmann, and L W Molenkamp. Microstructural characterisation of Bi_2Se_3 thin films. *J. Phys. Conf. Ser.*, 471(1):012043, 2013.

[TSL+14] N. V. Tarakina, S. Schreyeck, M. Luysberg, S. Grauer, C. Schumacher, G. Karczewski, K. Brunner, C. Gould, H. Buhmann, R. E. Dunin-Borkowski, and L. W. Molenkamp. Suppressing twin formation in Bi_2Se_3 thin films. *Adv. Mat. Int.*, 1(5), 2014.

[TT61] Iwao Teramoto and Shigetoshi Takayanagi. Relations between the electronic properties and the chemical bonding of $Sb_xBi_{2-x}Te_{3-y}Se_y$ system. *J. Phys. Chem. Solids*, 19(1-2):124 – 129, 1961.

[War69] Bertram Eugene Warren. *X-ray Diffraction*. Courier Corporation, 1969.

[WDSW82] CEC Wood, D Desimone, K Singer, and GW Wicks. Magnesium-and calcium-doping behavior in molecular-beam epitaxial III-V compounds. *J. Appl. Phys.*, 53(6):4230–4235, 1982.

[WJF+16] S. Wiedmann, A. Jost, B. Fauqué, J. van Dijk, M. J. Meijer, T. Khouri, S. Pezzini, S. Grauer, S. Schreyeck, C. Brüne, H. Buhmann, L. W. Molenkamp, and N. E. Hussey. Anisotropic and strong negative magnetoresistance in the three-dimensional topological insulator Bi_2Se_3. *Phys. Rev. B*, 94:081302, Aug 2016.

[WM60] J.R. Wiese and L. Muldawer. Lattice constants of Bi_2Te_3-Bi_2Se_3 solid solution alloys. *J. Phys. Chem. Solids*, 15(1-2):13–16, 1960.

[Wyc63] Ralph W G Wyckoff. *Crystal structures*, volume 1. Interscience Publ., New York, 2 edition, 1963.

[Wyc64] R.W.G. Wyckoff. *Crystal Structures: Inorganic compounds RXn, RnMX2, RnMX3*. Interscience Publ., New York, 2 edition, 1964.

[XQH+09] Y. Xia, D. Qian, D. Hsieh, L. Wray, A. Pal, H. Lin, A. Bansil, D. Grauer, Y. S. Hor, R. J. Cava, and M. Z.X Hasan. Observation of a large-gap topological-insulator class with a single Dirac cone on the surface. *Nat. Phys.*, 5(6):398–402, 2009.

[YZZ+10] Rui Yu, Wei Zhang, Hai-Jun Zhang, Shou-Cheng Zhang, Xi Dai, and Zhong Fang. Quantized anomalous Hall effect in magnetic topological insulators. *Science*, 329(5987):61–64, 2010.

[ZHC+10] Yi Zhang, Ke He, Cui-Zu Chang, Can-Li Song, Li-Li Wang, Xi Chen, Jin-Feng Jia, Zhong Fang, Xi Dai, Wen-Yu Shan, Shun-Qing Shen, Qian Niu, Xiao-Liang Qi, Shou-Cheng Zhang, Xu-Cun Ma, and Qi-Kun Xue. Crossover of the three-dimensional topological insulator Bi_2Se_3 to the two-dimensional limit. *Nat. Phys.*, 6(8):584–588, 2010.

[ZLQ+09] Haijun Zhang, Chao-Xing Liu, Xiao-Liang Qi, Xi Dai, Zhong Fang, and Shou-Cheng Zhang. Topological insulators in Bi_2Se_3, Bi_2Te_3 and Sb_2Te_3 with a single Dirac cone on the surface. *Nat. Phys.*, 5(6):438–442, 2009.

[ZQT+09] Guanhua Zhang, Huajun Qin, Jing Teng, Jiandong Guo, Qinlin Guo, Xi Dai, Zhong Fang, and Kehui Wu. Quintuple-layer epitaxy of thin films of topological insulator Bi_2Se_3. *Appl. Phys. Lett.*, 95(5):053114, 2009.

[ZRM01] Helin Zou, D. M. Rowe, and Gao Min. Preparation and characterization of p-type Sb_2Te_3 and n-type Bi_2Te_3 thin films grown by coevaporation. *J. Vac. Sci. Technol. A*, 19(3):899–903, 2001.

[ZYZ+10] Wei Zhang, Rui Yu, Hai-Jun Zhang, Xi Dai, and Zhong Fang. First-principles studies of the three-dimensional strong topological insulators Bi_2Te_3, Bi_2Se_3 and Sb_2Te_3. *New J. Phys.*, 12(6):065013, 2010.

Publications

1. N. V. Tarakina, S. Schreyeck, T. Borzenko, C. Schumacher, G. Karczewski, K. Brunner, C. Gould, H. Buhmann, and L. W. Molenkamp. Comparative Study of the Microstructure of Bi_2Se_3 Thin Films grown on Si(111) and InP(111) Substrates. *Crystal Growth & Design*, 12(4):1913-1918, 2012.

2. S. Schreyeck, N. V. Tarakina, G. Karczewski, C. Schumacher, T. Borzenko, C. Brüne, H. Buhmann, C. Gould, K. Brunner, and L. W. Molenkamp. Molecular beam epitaxy of high structural quality Bi_2Se_3 on lattice matched InP(111) substrates. *Applied Physics Letters*, 102(4):041914, 2013.

3. N. V. Tarakina, S. Schreyeck, T. Borzenko, S. Grauer, C. Schumacher, G. Karczewski, C. Gould, K. Brunner, H. Buhmann, and L. W. Molenkamp. Microstructural characterisation of Bi_2Se_3 thin films. *Journal of Physics: Conference Series*, 471(1):012043, 2013.

4. G. Landolt, S. Schreyeck, S. V. Eremeev, B. Slomski, S. Muff, J. Osterwalder, E. V. Chulkov, C. Gould, G. Karczewski, K. Brunner, H. Buhmann, L. W. Molenkamp, and J. H. Dil. Spin Texture of Bi_2Se_3 Thin Films in the Quantum Tunneling Limit. *Physical Review Letters*, 112:057601, 2014.

5. N. V. Tarakina*, S. Schreyeck*, M. Luysberg, S. Grauer, C. Schumacher, G. Karczewski, K. Brunner, C. Gould, H. Buhmann, R. E. Dunin-Borkowski, and L. W. Molenkamp. Suppressing Twin Formation in Bi_2Se_3 Thin Films. *Advanced Materials Interfaces*, 1(5):1400134, 2014. * contributed equally to this work

6. H. Maaß, S. Schreyeck, S. Schatz, S. Fiedler, C. Seibel, P. Lutz, G. Karczewski, H. Bentmann, C. Gould, K. Brunner, L. W. Molenkamp, and F. Reinert. Electronic structure and morphology of epitaxial $Bi_2Te_{3-x}Se_x$ topological insulator films. *Journal of Applied Physics*, 116(19), 2014.

7. M. Orlita, B. A. Piot, G. Martinez, N. K. S. Kumar, C. Faugeras, M. Potemski, C. Michel, E. M. Hankiewicz, T. Brauner, Č Drašar, S. Schreyeck, S. Grauer, K. Brunner, C. Gould, C. Brüne, and L. W. Molenkamp. Magneto-Optics of Massive Dirac Fermions in Bulk Bi_2Se_3. *Physical Review Letters*, 114:186401, 2015.

8. G. Karczewski, M. Szot, S. Kret, L. Kowalczyk, S. Chusnutdinow, T. Wojtowicz, S. Schreyeck, K. Brunner, C. Schumacher, and L. W. Molenkamp. Nanoscale morphology of multilayer PbTe/CdTe heterostructures and its effect on photo-luminescence properties. *Nanotechnology*, 26(13):135601, 2015.

9. S. Grauer, S. Schreyeck, M. Winnerlein, K. Brunner, C. Gould, and L. W. Molenkamp. Coincidence of superparamagnetism and perfect quantization in the quantum anomalous hall state. *Physical Review B*, 92:201304, 2015.

10. S. Schreyeck, K. Brunner, A. Kirchner, U. Bass, S. Grauer, C. Schumacher, C. Gould, G. Karczewski, J. Geurts, and L. W. Molenkamp. Kinetic limitation of chemical ordering in $Bi_2Te_{3-x}Se_x$ layers grown by molecular beam epitaxy. *Journal of Physics: Condensed Matter*, 28(14):145002, 2016.

11. S. Wiedmann, A. Jost, B. Fauqué, J. van Dijk, M. J. Meijer, T. Khouri, S. Pezzini, S. Grauer, S. Schreyeck, C. Brüne, H. Buhmann, L. W. Molenkamp, and N. E. Hussey. Anisotropic and strong negative magnetoresistance in the three-dimensional topological insulator Bi_2Se_3. *Physical Review B*, 94:081302, 2016.

12. T. R. F. Peixoto, H. Bentmann, S. Schreyeck, M. Winnerlein, C. Seibel, H. Maaß, M. Al-Baidhani, K. Treiber, S. Schatz, S. Grauer, C. Gould, K. Brunner, A. Ernst, L. W. Molenkamp, and F. Reinert. Impurity states in the magnetic topological insulator $V:(Bi,Sb)_2Te_3$. *Physical Review B*, 94:195140, 2016.

Danksagung

An dieser Stelle möchte ich mich bei allen bedanken, die mich während meiner Promotion unterstützt und maßgeblich zum Erfolg dieser Arbeit beigetragen haben.

Allen voran danke ich Prof. Laurens W. Molenkamp für die Möglichkeit diese Dissertation am Lehrstuhl Experimentelle Physik III durchzuführen, sowie für die vielen Diskussionen und die Unterstützung während meiner Promotion.

Ich danke auch ganz besonders Prof. Karl Brunner für die ausgezeichnete Betreuung und sein unermüdliches Interesse an meiner Arbeit.

Genauso möchte ich Prof. Grzegorz Karczewski meinen Dank ausdrücken, da er mir während seiner Forschungsaufenthalte in Würzburg stets mit Rat und Tat zur Seite stand.

Zudem möchte ich mich bei Dr. Nadezda V. Tarakina für den Einblick in die mikrostrukturellen Details und die tolle Zusammenarbeit bedanken.

Besonders möchte ich mich bei allen weiteren Beteiligten im Rahmen des 3-TOP Projekts bedanken, Prof. Charles Gould, Prof. Hartmut Buhmann, Dr. Claus Schumacher, Dr. Christoph Brüne, Dr. Tanja Borzenko, Stefan Grauer, Hanno Flentje, Martin Reuß, Jörn Wilhelm, Martin Winnerlein und Sabine Rosenberger.

Auch allen Kollaborationspartnern möchte ich an dieser Stelle meinen Dank ausdrücken.

Weiterer Dank gilt den technischen Angestellten, Martin Zipf, Petra-Wolf Müller, Volkmar Hock, Jana Hinterberger und Carmen Bundschuh, die den reibungsfreien Ablauf dieser Arbeit ermöglicht haben. Zudem danke ich meinen langjährigen Bürokollegen Christoph Pohl, Christopher Ames und Mirko Trabel für die großartige Atmosphäre und die zahlreichen wissenschaftlichen Diskussionen. Für die gute Zusammenarbeit und die tolle Atmosphäre am Lehrstuhl EP3 möchte ich allen Freunden und Kollegen danken.

Ich möchte auch Katja und meiner Familie für die Unterstützung während meiner Promotion ganz herzlich danken.